The Pennsylvania State University

The Graduate School

Department of Engineering Science and Mechanics

THE ELECTRICAL PROPERTIES OF GOLD NANOWIRES AND THEIR APPLICATIONS IN CHEMICAL SENSING

A Dissertation in

Engineering Science and Mechanics

by

Shawn Keebaugh

© 2009 Shawn Keebaugh

Submitted in Partial Fulfillment
of the Requirements
for the Degree of

Doctor of Philosophy

August 2009

The dissertation of Shawn Keebaugh was reviewed and approved* by the following:

Stephen Fonash
Bayard D. Kunkle Professor of Engineering Science and Mechanics
Dissertation Advisor
Chair of Committee

Tony Huang
Assistant Professor of Engineering Science and Mechanics

Jerzy Ruzyllo
Professor of Electrical Engineering and Materials Science and Engineering

Jian Xu
Assistant Professor of Engineering Science and Mechanics

Judith Todd
P.B. Breneman Department Head of Engineering Science and Mechanics

*Signatures are on file in the Graduate School

ABSTRACT

In this study, we explore the morphology dependent electrical behavior of gold nanowires and exploit these phenomena to develop robust, highly responsive gold nanowire sensors capable of detecting low concentrations of elemental and ionic mercury. The sensor design is straightforward; it consists of a single gold nanowire isolated between electrical contact pads. Accordingly, it is highly manufacturable, low power, and suitable for integration into sensor arrays. The nanosensor is based on electrical resistivity changes that arise upon adsorption of mercury onto gold surfaces. We demonstrate the advantages of the nanoscale design for this application and substantiate its use for other chemical detection applications. Though the gold-mercury system is reported here, the effects observed are universal and can be utilized in other metal-analyte combinations as well.

TABLE OF CONTENTS

LIST OF FIGURES vii

ACKNOWLEDGEMENTS xi

Chapter 1 Introduction 1

1.1 Overview of Metallic Nanowires 1
1.1.1 Electronic Applications of Metallic Nanowires 2
1.1.2 Chemical Sensing Applications of Metallic Nanowires 4
1.2 Research Objectives 8
1.3 Thesis Organization 8
1.4 References 10

Chapter 2 Nanowire Device Fabrication and Characterization 12

2.1 Nanowire and Thin Film Device Fabrication 12
2.1.1 Overview of Device Fabrication 12
2.1.2 Electron Beam Lithography 16
2.1.2.1 Direct-Write Mask Design 17
2.1.2.2 Direct-Write Data File Fracturing 18
2.1.2.3 Beam Energy, Current, Dose, and Spot-Size Selection 18
2.1.2.4 Direct Write 20
2.1.3 Gold Deposition 20
2.1.3.1 Gold Film Formation 20
2.1.3.2 Gold Evaporation Procedure 22
2.2 Nanowire Device Characterization 24
2.2.1 Field Emission Scanning Electron Microscopy Analysis 24
2.2.2 Atomic Force Microscopy Analysis 26
2.2.2.1 Smooth Continuous Nanowires 29
2.2.2.2 Rough Discontinuous Nanowires 31
2.3 Summary 32
2.4 References 33

Chapter 3 Electrical Characterization of Gold Nanowires 34

3.1 Background on the Electronic Properties of Metals 34
3.2 Electron Scattering in Metals 37
3.2.1 Phonon Scattering 39
3.2.2 Impurity and Defect Scattering 39
3.2.3 Surface Scattering 40
3.2.4 Grain Boundary Scattering 42
3.3 Electrical Conduction in Metallic Nanowires 43
3.3.1 Effects of Size on Electrical Resistivity 45

3.4 Dependence of Electrical Resistance on Nanowire Morphology 49
3.5 Temperature Dependence of Resistivity 53
3.5.1 Experimental Setup and Procedure 54
3.5.2 Results and Discussion 55
3.6 Summary 59
3.7 References 61

Chapter 4 Gold Nanowire Mercury Sensors 63

4.1 Introduction 63
4.1.1 Motivation for Mercury Sensing with Gold Nanowires 64
4.1.2 Adsorption of Mercury on Gold 66
4.1.3 Electrical Effects of Mercury Adsorption on the Gold Nanowires 67
4.2 Sensor Response to Hg Vapor – WKU Experiments 69
4.2.1 Experimental Setup and Procedure 69
4.2.2 Results and Discussion 70
4.3 Sensor Response to Hg^{2+} 72
4.3.1 Experimental Setup and Procedure 72
4.3.2 Results and Discussion 73
4.3.3 Kinetics Modeling 74
4.3.4 Surface to Volume Ratio 76
4.3.5 Selectivity of the Sensor 78
4.4 Hg Sensor Response – JPL Experiments 79
4.4.6 Experimental Setup 79
4.4.7 Sensor Response to Hg 80
4.4.8 Multiple Exposures and Sensor Regeneration 82
4.4.9 Size Effects 83
4.4.10 Sensor Selectivity 87
4.5 Applications and Advantages of the Nanowire Hg Sensor 90
4.6 Summary 91
4.7 References 92

Chapter 5 Electrical Stressing Gold Nanowires 94

5.1 Introduction 94
5.2 Electrical Stress Technique 96
5.3 Electrical Stress Induced Conductance and Morphology Changes 97
5.3.1 Failure Analysis of Electrically Stressed Nanowires 101
5.4 Thermal Induced Conductance and Morphology Changes 104
5.5 Response to Hg Vapor 107
5.6 Summary 108
5.7 References 110

Chapter 6 Summary and Future Work 111

6.1 Summary 111

6.2 Future Work 113

Appendix Nanowire and Thin Film Device Processing Details 115

F.1 Silicon Dioxide Growth / Silicon Nitride Deposition 115
F.2 E-beam Lithography Processing 115
F.2.5 Developing the Resist 117
F.3 Ti/Au Evaporation 117
F.3.1 Metal Lift-off 118
F.4 Photolithography 118
F.4.1 Resist Coating 118
F.4.2 Alignment, Exposure, Developing the Resist 119
F.4.3 Resist Descum 119
F.5 Ti/Pt Evaporation 119
F.5.1 Metal Lift-off 120

LIST OF FIGURES

Figure **1-1**: Scanning electron microscope (SEM) images and illustrations of the metallic interconnects used in modern semiconductor device technology [**10**]. .. 3

Figure **1-2**: Atomic force microscope images of a Pd mesowire on a graphite surface and their electrical response upon cycled hydrogen exposures. Images (A) and (C) were acquired in air; images (B) and (D) were acquired in a stream of hydrogen gas. A hydrogen-actuated break junction is highlighted. (E) Plot of the mesowire topography along its axis showing the direction of grain sliding (red arrows) associated with opening and closing of the break junction [**2**]. 6

Figure **1-3**: FESEM image of the electrochemically grown silver nanowires and their depleted inter-particle boundaries formed by wet chemical etching. (b) Illustration comparing the percolation path of a conduction electron in a thin film and nanowire structure [**3**]. 7

Figure **2-1**: Illustration of Au nanowire fabrication steps: (a) silicon wafer with thermal oxide or LPCVD nitride, (b) e-beam resist coat and exposure, (c) e-beam resist developing (d) deposition of Au, (e) lift-off of e-beam resist, (f) coat, exposure, and developing of photoresist, (g) deposition of Pt contact layer, and (h) final device (cross section shown at a contact) 14

Figure **2-2**: Picture showing the fabricated nanowire sensors on a 3 inch wafer, an optical microscope image of the platinum contacts, and a drawing of idealized Au nanowires between the Pt contacts. 15

Figure **2-3**: Illustration of two-point (Left) and four point (Right) electrical contact pad configurations. 16

Figure **2-4**: EBPG-5HR e-beam lithography tool at the PSU Nanofab. 17

Figure **2-5**: Cross-section of ideal PMMA resist exposure, showing the resultant development and metallization. The larger exposure near the substrate is due to the secondary electrons produced at the substrate [**1**]. 19

Figure **2-6**: Geometry of condensate nucleus formation on a substrate [**3**]. 21

Figure **2-7**: Kurt Lesker (Left) and Semicore (Right) Evaporators at the PSU Nanofab. 23

Figure **2-8**: (Top) FESEM image of a single gold nanowire approximately 40nm wide. (Bottom) Nanowires in parallel with a pitch of 700nm. The edges of the lithographically defined nanowire are rough. 26

Figure **2-9**: AFM images of a 1μm Au thin film and the Pt electrical contact pad. (a) 2-D image, (b) 3-D image, and (c) cross-sectional profile showing the step between the substrate and electrical pad (70nm thickness); this cut was taken from image (a). 28

Figure **2-10**: Three-dimensional AFM images of Au nanowires with the DI rinse step omitted. The morphology is very rough and irreproducible. 28

Figure **2-11**: AFM image highlighting the grain-boundaries in the gold nanowire (Left). 3-D image of the nanowire (Right). 30

Figure **2-12**: Cross-sectional cut of nanowire and a plot of the average nanowire thickness. 30

Figure **2-13**: AFM image of rough, discontinuous wire and a profile showing the particles are much thicker in regions than what was recorded on the QCM. 31

Figure **3-1**: Metal modeled as a lattice of positive ion cores surrounded by a sea of free valence electrons [**1**]. 35

Figure **3-2**: Energy band formation of a metal [**1**]. 37

Figure **3-3**: Three dimensional illustration of an ideal film or nanowire. 41

Figure **3-4**: Experimental data of the resistivity dependence upon Cu line-width and thickness. Equation 3.9 was fit to the curves to determine the *p* and *R* values for the different nanowire thicknesses. 45

Figure **3-5**: Plot of the electrical resistivity vs. line-width for gold nanowires and thin-films with constant 20nm thickness. 48

Figure **3-6**: I-V curves of 40nm wide Au nanowires that received the DI rinse (top). Bar chart highlighting the variability in resistance between nanowires (bottom). 51

Figure **3-7**: I-V curves of 40nm wide Au nanowires that received the IPA rinse only (top). Bar chart highlighting the variability in resistance between nanowires (bottom). **Note: Plot is logarithmic on the y-axis.** 52

Figure **3-8:** Nanowire resistivity plotted against temperature. 57

Figure **4-1**: Illustration of the mercury cycle [**11**]. 65

Figure **4-2**: Illustration of difference between specular and diffuse scattering. An incoming electron (e^-) strikes the metal surface and for specular reflection, the component of momentum along the applied filed (indicated by *E* and the arrow) is conserved, whereas for diffuse reflection, it is not and the reflected

electron has a random direction of momentum, thus reducing the net current flow [9]. 68

Figure **4-3**: Mercury vapor generator set-up used for the initial experiments on the gold nanowire array sensor. 69

Figure **4-4**: Response of a nanowire sensor (rough morphology) to elemental Hg. ... 71

Figure **4-5**: Response of Au nanowire array (50 wires) to 18ppb Hg vapor. 71

Figure **4-6**: Setup for ionic mercury detection experiments. 72

Figure **4-7**: Ionic current of 1μM $HgCl_2$ between two Pt electrical contact pads. 73

Figure **4-8**: Nanowire sensors' response to varying $HgCl_2$ concentrations. Solid and dashed lines represent the experiment and modeling, respectively. 74

Figure **4-9**: Responses of sensors with varying dimensions to 1μM Hg^{2+}. (a) Comparison of nanowires 30nm thick (blue) and 20nm thick (green). (b) Comparison of thin films 30nm thick (blue) and 20nm thick (green). (c) Comparison of nanowires 30nm thick (green) to a thin film 30nm thick (blue). (d) Comparison of nanowires 20nm thick (green) to thin film 20nm thick (blue). 77

Figure **4-10**: Selectivity of Au nanowire sensor to Cu^{2+} and Mg^{2+}. Concentrations used here were 1mM $CuCl_2$ (red), 1mM Mg_2 (green), and 1μM $HgCl_2$ (blue). ... 78

Figure **4-11**: Au nanowire response vs. time to varying Hg vapor concentrations...... 80

Figure **4-12**: Plot of the nanowire sensor response to varying Hg concentrations. 81

Figure **4-13**: Response of nanowire sensor to multiple exposures and multiple concentrations (5ppb, 5ppb, 20ppb, and 50ppb; left to right). Sensor regenerated to base-line value after each exposure. 82

Figure **4-14**: Plot of the Au wire resistivity vs. line-width before and after 1ks 50ppb Hg exposure. 84

Figure **4-15**: Plot of the change in Au nanowire resistivity vs. line-width after 50ppb Hg exposure. 85

Figure **4-16**: Plot of sensitivity vs. Au line-width. 85

Figure **4-17**: Sensitivity vs. surface to volume ratio for the Au nanowires. 87

Figure **4-18**: Nanowire sensor response to 100ppm NH_3. Gas was introduced at 300s. 88

Figure **4-19**: Nanowire sensor response to 100ppm CO. Gas was introduced at 300s. 89

Figure **4-20**: Nanowire sensor response to 4% H_2. Gas was introduced at 250s. 89

Figure **5-1**: Electrical stress technique employed on a multiple nanowire device (a) linear scale, (b) log-scale. 98

Figure **5-2**: AFM images of gold nanowires. The nanowires on the left are of the as-fabricated, rough type. The nanowires on the right have been electrically stressed to alter their morphology using our post-deposition approach to morphology control. 99

Figure **5-3**: I-V curves of a single 40nm wide Au nanowire before and after the electrical stressing. The curve remains linear, but has an increased slope. 99

Figure **5-4**: Electrical stressing a single 40nm wide Au wire. The achievable changes in conductance depend on initial conductivity and morphology. 100

Figure **5-5**: Plot of a stress-to-failure test on a multiple nanowire device. The optimum region to discontinue the electrical stressing is highlighted in red. 102

Figure **5-6**: Plot of stress-to-failure test on a 40nm wide single nanowire device. 102

Figure **5-7**: SEM image of a nanowire device that failed during electrical stressing. The electrons were flowing in the bottom to top direction during the electrical stress procedure. 103

Figure **5-8**: Plot of conductance change vs. annealing temperature for multiple nanowire devices (40nm wire width). 104

Figure **5-9**: 3D AFM images of 40nm Au nanowires (a) Nanowire is as-fabricated, (b) nanowire is annealed, and (c) nanowire is electrically stressed. 105

Figure **5-10**: FESEM image of nanowires that failed during the annealing process. Temperature of the hotplate was 250C. 106

Figure **5-11**: Response of a smooth continuous nanowire to 1μM $HgCl_2$. 107

Figure **5-12**: Resistance response of rough, discontinuous nanowire to 35ppb Hg exposure (top) and 1μM $HgCl_2$ (bottom). 108

ACKNOWLEDGEMENTS

First and foremost, I would like to thank my research advisor Dr. Stephen Fonash for his guidance and support throughout the years. I could not have asked for a better advisor. His innovative thinking inspired me to think outside the box and his ideas contributed greatly to this research and dissertation. Additionally, I am very appreciative to my committee members; their suggestions, contributions and advice significantly improved this dissertation.

I am very grateful to the staff at CNEU for helping me with just about everything and to the graduate students in my group for the great discussions and advice. Additionally I would like to thank the Penn State Nanofabrication Facility staff and the NASA JPL E-Nose group for their support in using their facilities for my research.

Finally, I would like to thank my family, friends, and especially my wife, Elisha, for supporting me throughout this long journey. You are truly what kept me going and you were always there when I needed you. For this, I am eternally grateful.

Chapter 1

Introduction

1.1 Overview of Metallic Nanowires

Metallic nanowires are one-dimensional metal structures which have lengths ranging from nanometers to millimeters, and diameters not exceeding a few hundred nanometers. Recently, they have attracted a great deal of attention due to the innate phenomena associated with their nano-scale dimensions. These phenomena enable for very high density integration with semiconductor electronics [1] (e.g. interconnects and junctions) and makes them ideal candidates for chemical and biological sensing applications [2][3][4].

Researchers have developed a variety of techniques to fabricate metallic nanowires; these methods can be classified into two main categories: Top-down and bottom-up fabrication approaches. Top-down methods use standard lithography techniques, like direct-write e-beam lithography, to pattern and deposit, or pattern and etch materials. Bottom-up approaches are more versatile and can be used to build metal nanowires through mechanisms such as self-assembly and template-based synthesis [5][6]. These fabrication techniques can be used to manufacture a wide-variety of metallic nanowire structures for electronic and sensor applications.

1.1.1 Electronic Applications of Metallic Nanowires

As the semiconductor industry decreases device dimensions and increases device density [1], it becomes necessary to scale-down the dimensions of the metal interconnects and contacts. Decreasing the cross-sectional area of the nanowires results in substantial increases in the current density and increases the likelihood for device failure due to joule heating and electromigration [7]. Furthermore, as the dimensions of the wire approach the mean free path of the conduction electrons, the electrical resistance no longer scales linearly with the cross-sectional area. In order to optimize the nanostructures' performance and reliability, it is necessary to examine their size dependent electrical behavior and failure mechanisms.

Although metal nanowires have attracted most of their attention for applications in interconnect technologies, they can also be used to form junctions with other materials to make devices such as thermocouples and diodes. Recent fabrication techniques [8][9] have enabled the ability to precisely and controllably position nanowires to form junctions with other nanowires. These advances will eventually enable the development novel devices which contain metal nanowires as an integral part of the active device. The current drive, however, is to study their properties because of their ubiquitous role in semiconductor technology.

The figure of merit commonly used to evaluate the performance of an electrical interconnect (Figure **1-1)** is the time constant $\tau = RC$, where R is the resistance and C is the capacitance [1][10]. To improve the speed between devices, it is necessary to reduce the delay, τ, by reducing the resistance or capacitance. The capacitance is a function of

the wire dimensions, spacing, and permittivity of the low-k dielectric used between the metal lines. The resistance, *R*, of the metal lines is a function of the wire material, geometry, dimensions, and morphology. The scattering mechanisms responsible for increases in the electrical resistivity (e.g. surface and grain-boundary scattering) are generally exacerbated at the nanoscale [1][11][12][13][14][15]. These phenomena are a direct result of the metal nanowires having dimensions that are on the same order of magnitude as the mean-free-path, λ, of the conduction electrons in the metal [16][17][18]. In this size range, the resistance no longer scales linearly with the cross-sectional area and the interaction of conduction electrons with the surface of the nanowire becomes increasingly important. The various scattering mechanisms responsible for the size-related electrical resistance increase are covered in Chapter 3.

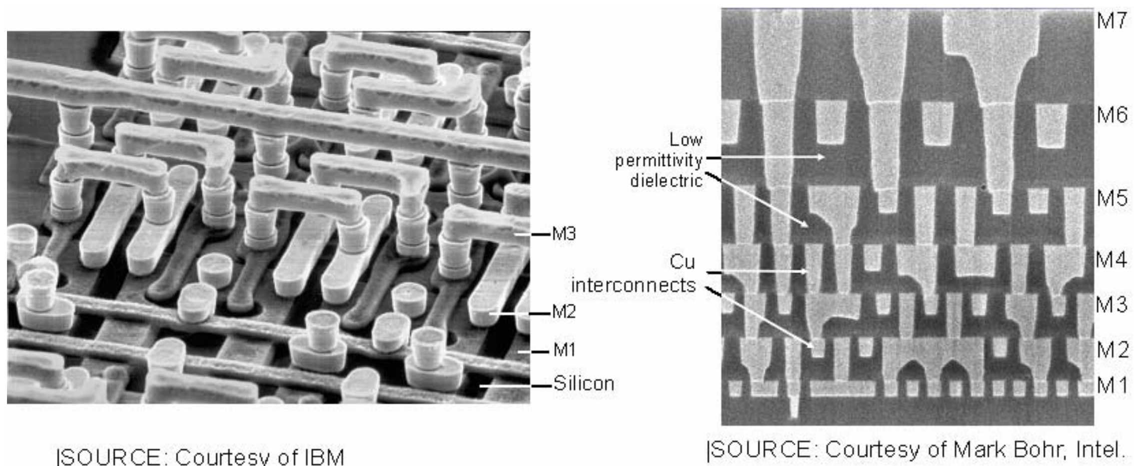

Figure **1-1**: Scanning electron microscope (SEM) images and illustrations of the metallic interconnects used in modern semiconductor device technology [10].

1.1.2 Chemical Sensing Applications of Metallic Nanowires

The high surface-to-volume ratio and selectivity to surface chemical reactions makes metallic nanowires ideal candidates for chemical sensing applications. Thin metal films, which exhibit similar properties to nanowires, have frequently been used as active elements in gas sensing applications. Generally, these sensors operate by monitoring electrical resistivity changes which arise from the chemical absorption or adsorption on the film surface [19][20]. These surface interactions are usually highly selective and the mechanism responsible for the resistance change varies between metal-analyte combinations.

Metallic nanowires have several advantages over their thin-film sensor counterpart: First, they are smaller, consume less power, and are more apt to be integrated into sensor arrays. The device density can be made higher and they can be fabricated onto smaller chips. Additionally, the lower power of the devices makes them particularly appealing for small, portable sensor configurations. Second, they have higher surface-to-volume ratios. This allows for a rapid uptake of gas upon absorption, and rapid release upon desorption. The total amount of vapor released during regeneration is less than a thin film which makes them safer and more environmentally friendly for hazardous gas sensing applications. Third, the high surface to volume ratio increases the proportion of conduction electrons interacting with the surface. In adsorption processes, the sensor response generally depends on a change in the electrical resistivity of a thin modified layer formed at the surface, or on the scattering events which occur between the conduction electrons and the affected surface. Since the higher

surface-to-volume increases the proportion of electrons interacting with the affected regions, it results in an improved sensor response and sensitivity. Finally, the nanowires are one-dimensional and consequently reduce the number of percolation paths. Therefore, the electrons are forced to cross each of the affected grain-boundaries. This is in contrast to a thin film where the electrons may percolate around the affected grain-boundaries and reduce sensitivity.

Though there are many advantages of metal nanowires, the majority of nanowire sensor work has been focused on semiconductor materials [21][22][23][24]. This is due to the wide range applications that can be tailored through doping and functionalizing the materials. The adsorption or binding of materials to the semiconductor surface can result in accumulation or depletion regions which alter the nanowire's electrical conductivity. Semiconductor nanowires have been used in a plethora of sensor applications to demonstrate the many advantages of the nanoscale for electrical sensing purposes. Little research, however, has been done to investigate the use of metallic nanowires for sensing applications.

Penner *et al.* first demonstrated the use of Pd nanowires for H_2 sensing [2]. The Pd nanowires were electrochemically grown and transferred onto a glass slide where silver paint was used to contact the wires. The transfer process caused the nanowires to form nm-size breaks. Consequently, the measured resistance was much larger than anticipated. Once exposed to H_2, the nanowires formed a hydride which caused an increase in the nanowires' volume. The volumetric change was large enough to bridge the breaks which were formed in the transfer process; therefore, an increase in conductance was measured upon H_2 exposure (Figure **1-2**). Such a response was not

expected since most thin film sensors experience an increase in resistance upon H_2 inclusion [25]. This is an example of a novel detection mechanism at the nano-scale, but is unique to the Pd-H_2 system. Since then, other Pd nanowire H_2 sensors have been developed; some operating upon the break-junction mechanism [26] and others based on increases in bulk resistivity [27] upon absorption.

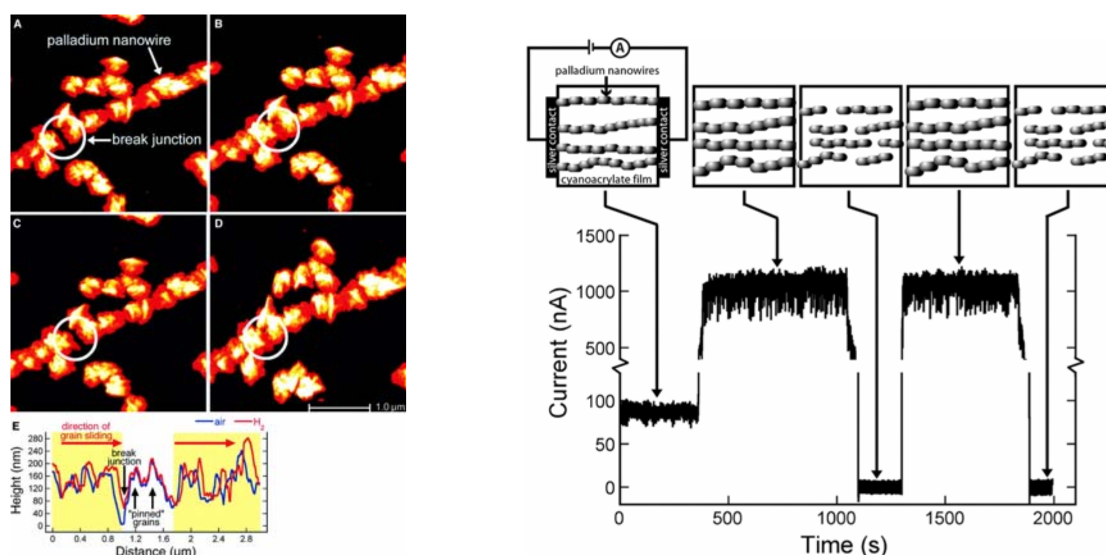

Figure **1-2**: Atomic force microscope images of a Pd mesowire on a graphite surface and their electrical response upon cycled hydrogen exposures. Images (A) and (C) were acquired in air; images (B) and (D) were acquired in a stream of hydrogen gas. A hydrogen-actuated break junction is highlighted. (E) Plot of the mesowire topography along its axis showing the direction of grain sliding (red arrows) associated with opening and closing of the break junction [2].

Penner's group also demonstrated the use of silver nanowires for detection of amines [3]. A similar electrochemical fabrication technique was used to grow these nanowires. The as-fabricated morphology was rough, and was further roughened by wet chemical etching. The resulting nanowires exhibited depleted inter-particle regions that dominated the conduction of the wires. Adsorption of amines into these regions resulted in resistance increases more than one-thousand times larger than its silver thin-film

counterpart. The reason for this large change remains unclear, but the authors attribute it in part to the one-dimensional geometry of the nanowire; i.e., the electrons are forced to cross every inter-particle boundary in the nanowire where the amine is absorbed, but have a chance to percolate along a less resistive conduction path in a thin film Figure **1-3**. The results from this research illustrate the importance of one-dimensionality and morphology on nanowire sensor's response.

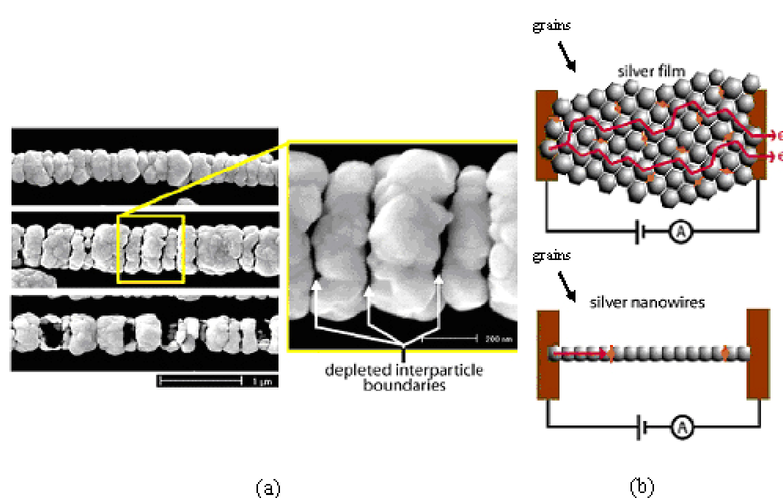

Figure **1-3**: FESEM image of the electrochemically grown silver nanowires and their depleted inter-particle boundaries formed by wet chemical etching. (b) Illustration comparing the percolation path of a conduction electron in a thin film and nanowire structure [3].

The novel detection mechanisms and improved performance of these sensors indicates the need for further investigation and exploration into the use of metallic nanowires for sensing applications. The most simplistic and efficient approach is to scale down a thin film chemical sensors to nanowire geometries. This is the approach used here for developing the Au nanowire Hg sensor.

1.2 Research Objectives

The aim of this thesis is to study the electrical properties of gold nanowires and to exploit their properties for sensor applications. To do this, the dependence of the electrical resistivity on size, morphology, and temperature is reported on. In addition, the development of a gold nanowire sensor capable of ppb detection of mercury vapor will be presented. To meet these goals, several research objectives were proposed and completed. The objectives include: nanowire fabrication, physical characterization, material modification (electrical-stressing), electrical characterization, and implementation of the nanowires into a finalized sensor test structure.

1.3 Thesis Organization

In Chapter 2, the fabrication of the metallic nanowires is described and the nanowire size, shape, and morphology are characterized. The dependence of nanowire morphology on substrate surface condition will be reported on. The fabrication techniques enable the production of single and multiple nanowire devices with controllable dimensions and very high surface to volume ratios.

In Chapter 3, the electrical properties of the fabricated nanowires are investigated. An overview of the electrical conduction mechanisms and the effects of the nanoscale size are covered. The electrical characterization of the nanowire devices will be discussed and reported on. The characterization includes: two point resistance, four-point resistivity, and low-temperature resistivity measurements. The size effects and nano-scale phenomena associated with small dimensions will be discussed.

In Chapter 4, a fast, highly sensitive and selective elemental and ionic mercury sensor is demonstrated. Details regarding the sensor performance covered. Electrical characterization of the nanowires and the size effects are demonstrated and an explanation for the improved sensor response is given.

In Chapter 5, an electrical stressing technique is used to selectively alter the morphology of the nanowires. The electrical resistivity, morphology, and response of the nanowires to mercury vapor are evaluated before and after the electrical stressing technique.

In Chapter 6 the results obtained throughout the thesis are summarized and future work in this research area is proposed.

1.4 References

1. The International Roadmap for Semiconductors (ITRS), 2007 edition, http://www.itrs.net/Links/2007ITRS/Home2007.htm

2. F. Favier, E.C. Walter, M.P. Zach, T. Benter, and R.M. Penner, *Science*, 293, 5538 (2001).

3. B.J. Murray, E.C. Walter, and R.M. Penner, *Nano Letters*, 4, 665 (2004).

4. Y. Xia, P. Yang, Y. Sun, Y. Wu, B. Mayers, B. Gates, Y. Yin, F. Kim, and H. Yan, *Advanced Materials*, 15, 353 (2003).

5. G. Cao, *Nanostructures and Nanomaterials*, Imperial College Press: London (2004).

6. B. Bhushan, *Springer Handbook of Nanotechnology*, Springer Verlag: Berlin (2004).

7. C. Durkan, M.A. Schneider, M.E. Welland, *Journal of Applied Physics,* 86, 1280 (1999).

8. Y. Shan, A.K. Kalkan, C.Y. Peng, S.J. Fonash, *Nano Letters*, 4, 2085 (2004).

9. S. Evoy, N. DiLello, V. Deshpande, A. Narayanan, H. Liu, M. Riegelman, B.R. Martin, B. Hailer, J.C. Bradley, W. Weiss, T.S. Mayer, Y. Gogotsi, H.H. Bau, T.E. Mallouk, and S. Raman, *Microelectronic Engineering*, 75, 31 (2004).

10. S.O. Kasap, *Principles of Electronic Materials and Devices*, McGraw Hill: New York (2006).

11. C. Durkan and M.E. Welland, *Physical Review B*, 61, 14215 (2000).

12. H. Marom, J. Mullin, and M. Eizenberg, *Physical Review B*, 74, 045411 (2006).

13. W. Steinhogl, G. Schindler, G. Steinlesberger, M. Traving, and M. Engelhardt, *Journal of Applied Physics*, 97, 023706 (2005).

14. J. J. Plombon, E. Andideh, V.M. Dubin, and J. Maiz, *Applied Physics Letters*, 89, 1131124 (2006).

15. W. Steinhogl, G. Schindler, G. Steinlesberger, and M. Engelhardt, *Physical Review B*, 66, 075414 (2002).

16. K. Fuchs, *Proceedings of the Cambridge Philosophical Society*, 34, 100 (1938).

17. E. Sondheimer, *Advances in Physics*, 1, 1 (1952).

18. A.F. Mayadas, M. Shatzkes, *Physical Review B*, 1, 1382 (1970).

19. J.J. McNerney, P.R. Buseck, and R.C. Hanson, *Science*, 178, 611 (1972).

20. J. R. Anderson, *Chemisorption and Reactions on Metallic Films*, Academic Press: New York (1971).

21. Y. Cui, Z. Wei, H. Park, and C.M. Lieber, *Science*, **293**, 5533 (2001).

22. A. Kolmakov and M. Moskovits, *Annual Review of Materials Research*, 34, 151 (2004).

23. A. Kolmakov, D.O. Klenov, Y. Lilach, S. Stemmer, and M. Moskovits, *Nano Letters*, 5, 667 (2005).

24. A. K. Wanekaya, W. Chen, N.V. Myung, A. Mulchandani, *Electroanalysis*, 18, 533 (2006).

25. J. RaviPrakash, A.H. McDaniel, M. Horn, L. Pilione, P. Sunal, R. Messier, R.T. McGrath, and F.K. Schweighardt, *Sensors and Actuators B*, 120, 439 (2007).

26. M.Z. Atashbar, D. Banerji, S. Singamaneni, *IEEE Sensors Jornal*, 5, 792 (2005).

27. M.H. Yun, N.V, Myung, R.P. Vasquez, C.S. Lee, E. Menke, and R.M. Penner, *Nano Letters*, 4, 419 (2004).

Chapter 2

Nanowire Device Fabrication and Characterization

2.1 Nanowire and Thin Film Device Fabrication

The gold nanowire and thin film devices used in this work were fabricated using standard solid-state device processing techniques in a class 10 clean-room environment at the Penn State Nanofabrication Facility. An overview of the device fabrication is given below and is followed with a discussion of the critical steps (e-beam lithography and metal deposition) involved in the device processing. Details of all device processing steps can be found in Appendix 1.

2.1.1 Overview of Device Fabrication

The Au nanowire and thin film devices used in this work were fabricated using the following procedure (Figure **2-1**): First a 200nm thick thermal SiO_2 or LPCVD Si_3N_4 layer was grown / deposited on a bare 3-inch Si wafer to act as an electrically insulating floor for the nanowire device. Next an e-beam resist (3% polymethylmethacrilate (PMMA) 950k, dissolved in anisole) was spun onto the wafer at 4000rpm and soft-baked on a hot-plate at 180C for 3 minutes. This resulted in a 120nm thick PMMA layer as determined by profilometer measurements. After this, a 15nm thick Au layer was thermally evaporated onto the resist surface to help prevent charging on the oxide surface

in the subsequent e-beam lithography step. The resist was then exposed with an e-beam tool (EBPG-5HR) and the beam currents, spot sizes, and doses were determined from the results of a preceding dose array. Once exposed, the Au conducting layer was removed using a wet chemical etching procedure. The resist was then developed for 130 seconds in a 1:7 methyl-iso-butyl ketone: isopropanol solution kept at 20C in temperature controlled water bath. The wafer was immediately rinsed in isopropanol and then de-ionized (DI) water to remove any residual resist and/or contaminants that may have been left in the exposed regions. Next the wafer was loaded in an evaporator where a thin Ti adhesion layer followed by a Au layer was e-beam evaporated at a rate of 0.5A/s. A lift-off procedure in acetone was then used to reveal the Au nanowire features. Contacts to the nanowire were then patterned via photolithography. This process involved a dual-layer (LOR5A / SPR 3012) resist structure to help prevent fencing of the contact structure. The coated samples were then exposed in a MA-6 contact aligner containing the contact pattern photo-mask. Once exposed, the sample was baked at 100C in a post-exposure bake step and was subsequently developed in MF-CD-26 and rinsed in DI water. An oxygen plasma was then used to remove the resist scum in order to make a clean surface for contact between the Au nanowires and Pt electrical pads. The sample was then loaded in an evaporator and a Ti/Pt layer (3.5nm/70nm) was e-beam evaporated. Metal lift-off in Remover PG© solution at 70C was then employed to complete the device fabrication. Pictures of the resulting devices are shown in Figure **2-2**.

Gold Nanowire Device Fabrication

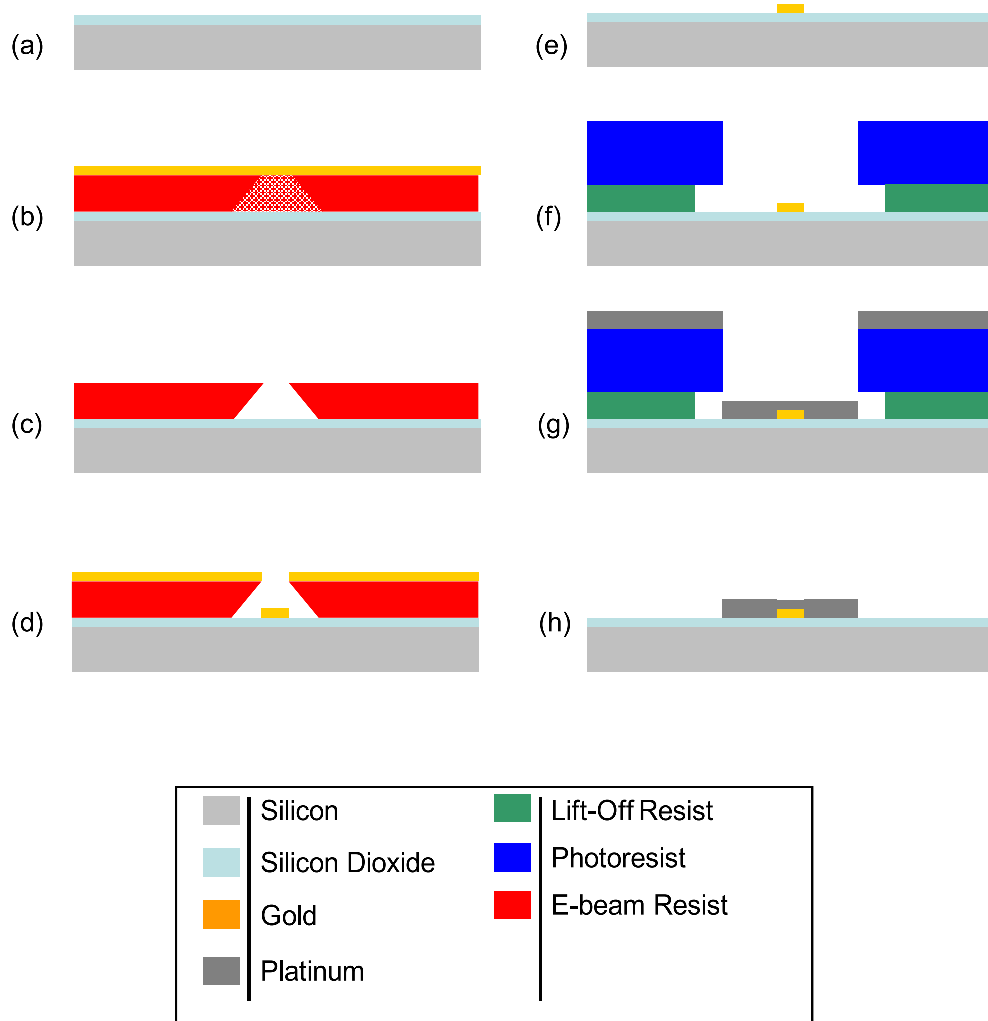

Figure **2-1**: Illustration of Au nanowire fabrication steps: (a) silicon wafer with thermal oxide or LPCVD nitride, (b) e-beam resist coat and exposure, (c) e-beam resist developing (d) deposition of Au, (e) lift-off of e-beam resist, (f) coat, exposure, and developing of photoresist, (g) deposition of Pt contact layer, and (h) final device (cross section shown at a contact)

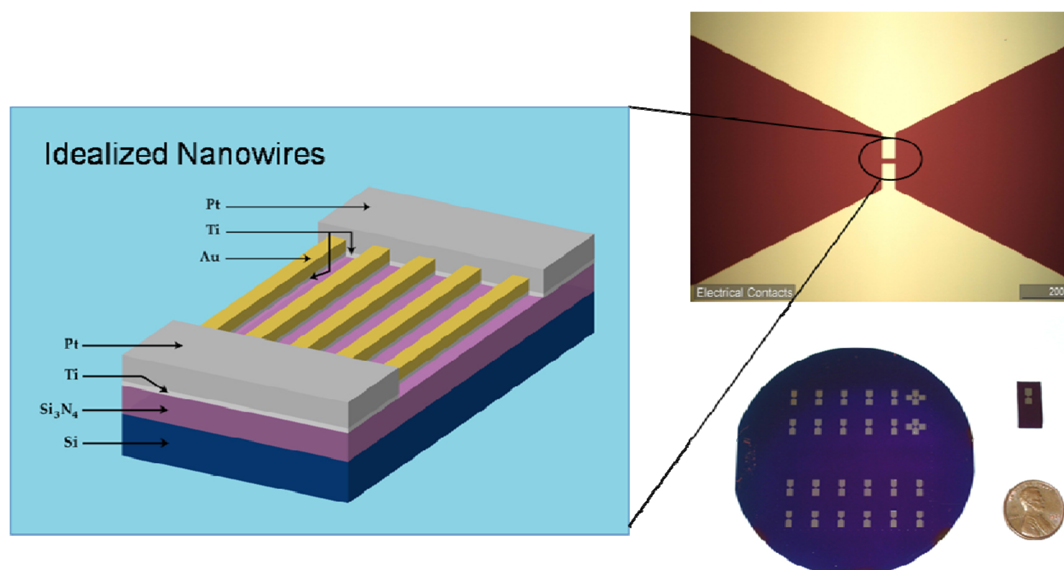

Figure **2-2**: Picture showing the fabricated nanowire sensors on a 3 inch wafer, an optical microscope image of the platinum contacts, and a drawing of idealized Au nanowires between the Pt contacts.

Single and multiple nanowire devices were fabricated using the aforementioned procedure. The single nanowire devices were connected to the electrical contact pads in two-point and four-point configurations (Figure 2-3). The multiple nanowire devices consisted of 50 parallel nanowires with a 700nm pitch and were connected to the contact pads in a two-point configuration. The electrical contact pads were approximately 2.5mm x 2.5mm and narrowed at the ends where they contacted the nanowires. The spacing between adjacent contact pads was 20µm in the two-point configuration and 10µm in the four-point configuration. The pads were designed so they were large enough for contacting the electrical clips used in the sensor experiments.

A total of 24 devices were fabricated per wafer. The individual devices were cleaved from the wafer and examined separately in the characterization and experimental procedures.

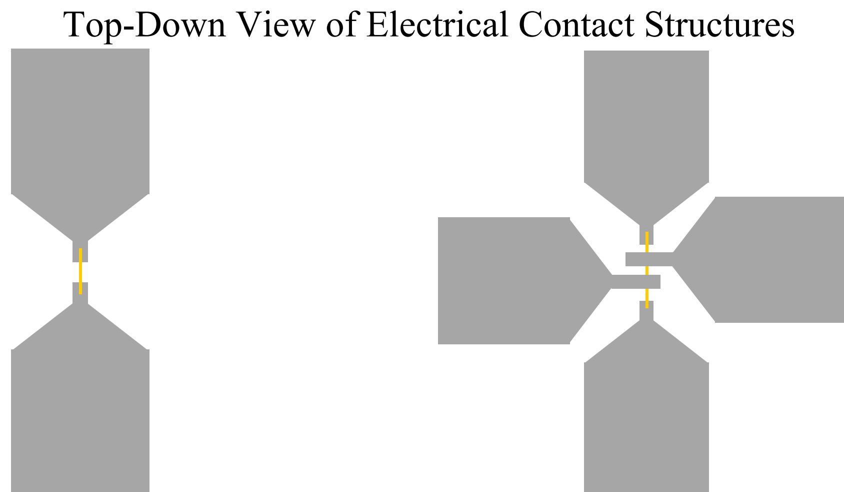

Figure **2-3**: Illustration of two-point (Left) and four point (Right) electrical contact pad configurations.

2.1.2 Electron Beam Lithography

The e-beam lithography direct write was perhaps the most involved and critical step in the fabrication of the gold nanowires. Much development work was required to optimize the process. The PSU Nanofab's e-beam lithography tool (Leica EBPG-5HR, Figure **2-4**) was used for our direct write lithography efforts. The tool is a vector scan writer and uses a thermal emitter which can accelerate electrons down the column with energies as high as 100keV. Electromagnetic coils and lenses in the column are used to shape the beam, vary the beam size, and move the beam. The tool is capable of

approximately 10nm diameter spot sizes and features smaller than 20nm. The direct write process used in this work involved four main procedures: designing a direct-write mask file, fracturing the mask file data, selecting the tool conditions (dose array), and writing the job.

Figure **2-4**: EBPG-5HR e-beam lithography tool at the PSU Nanofab.

2.1.2.1 Direct-Write Mask Design

The direct-write mask design was performed using L-Edit software. Three data layers were created: Layer 1 for the large features (>1um); Layer 2 for the medium sized features (200nm-1μm); and Layer 3 for the small features (<200nm). Multiple layers were used because of the different dosing conditions and/or fracture sizes used for the features. Since e-beam lithography is a serial process, the write times can be long, high cost, and low throughput. The goal in designing the mask was to minimize the write time, but still obtain the desired patterns in the resist.

2.1.2.2 Direct-Write Data File Fracturing

Once the L-Edit file was created it was converted to a GDSII file and transferred to CATS software. This software was used to fracture the GDSII file and converted it into the machine language (IWFL file). In doing this, the accelerating voltage and data fracture size were selected. The 100 keV accelerating voltage was used to improve the resolution and to reduce the proximity effects. The data fracture sizes varied: Layer 1 was fractured at 250nm, Layer 2 was fractured at 100nm, and Layer 3 was fractured at 10nm. These sizes were selected because of their availability on the tool and to help prevent any rounding errors in the data. In other words, the feature sizes were evenly divisible by fracture sizes.

2.1.2.3 Beam Energy, Current, Dose, and Spot-Size Selection

Prior to exposure, the tool was prompted to generate a spot table and list the available beam currents and corresponding spot sizes. The range of beam currents was typically on the order of 100pA-100nA and the spot sizes ranged from 10nm-300nm. The spot-size used in the direct write was always selected to be at least 10% greater than the fracture size of the data file in order to prevent under-exposure of the resist and problems with overlay.

As mentioned above, we performed the direct write with the maximum accelerating voltage (100kV) and aperture (400µm) available on the tool. When the electrons impact the resist /substrate stack at high energies they forward-scatter, back-scatter, and excite secondary electrons. The scattered electrons and secondary electrons

are responsible for exposing the resist; sometimes up to tens of microns from where they initially impact the substrate (proximity effects). The 100kV accelerating voltage helps minimize this effect by pushing the plume of scattered electrons deeper into the substrate. The collision-based exposure mechanisms in e-beam lithography results in the PMMA resists having re-entrant profiles (Figure **2-5**). This profile is highly desirable for lift-off processing and prevents the need for dual layer resist stacks.

The optimum dose was selected by performing a dose array on the PMMA coated substrates. The dose was varied across the substrate for the different layers and the substrate was processed through the first metal lift-off as explained in the previous section. The substrate was then inspected optically and in the SEM. We were searching for the dose that would give us a continuous metal line with the target line-width. For the large alignment marks, the selected dose was 1800μC/cm^2 and for the smaller features the dose was 4100μC/cm^2. Slight adjustments in the dose were necessary as the filament aged or when it was replaced.

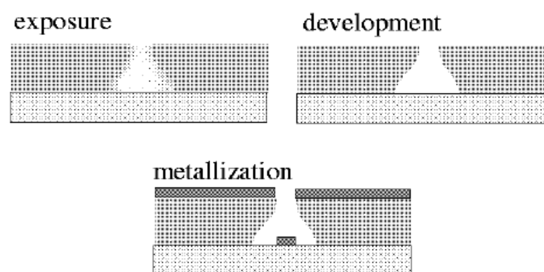

Figure **2-5**: Cross-section of ideal PMMA resist exposure, showing the resultant development and metallization. The larger exposure near the substrate is due to the secondary electrons produced at the substrate [1].

2.1.2.4 Direct Write

After determining the direct-write parameters, the wafer was loaded into the tool on a 3" holder and a job file was created. The first step in this was to generate a spot table. The table was compared to the previous table to ensure the beam was stable. Next, the beam currents were selected and measured by the Faraday cup on the holder. Several iterations were usually required to obtain the desired beam currents. Once acquired, the holder was loaded into the chamber and height measurements were made across the wafer. After this, the job-file containing all the layers and beam currents was loaded in the software and the direct write was started. The patterns used in this work took approximately 35 minutes to write. Once completed, the holder was unloaded from the tool and the wafer removed from the holder.

2.1.3 Gold Deposition

2.1.3.1 Gold Film Formation

The other critical step in the formation of the nanowires and thin films was the Au deposition procedure. The Au evaporation procedure plays an important role in determining the structure and morphology of the thin films and nanowires. Au has a face-centered cubic (FCC) atomic crystal structure and typically deposits so that the plane with the lowest surface energy, γ_f, {111} is exposed during deposition [3]. However, the interfacial energy, γ_i, and surface energy of the substrate, γ_s, also contribute to the Au film formation (Figure **2-6**). The shape of the Au nucleus will adjust during film growth

to minimize the total surface energy of the system [2] (Eq. **2.1**). In doing this, it is common for Au to have a polycrystalline structure with island-like film growth [3].

During the polycrystalline film growth process, the Au atoms nucleate to form crystallites or grains. These grains grow in size until they come in contact with one another. Once in contact, the surface atoms migrate across the boundaries of the grains and coalesce to form larger metal particles (i.e. grain boundary migration). The grains continue to grow until the deposition process is complete. The grain-size varies between tools and processing conditions, but it is common for the grain size of evaporated metal to be approximately equal to the film or nanowire thickness.

As previously mentioned, both silicon nitride and silicon dioxide were used as electrically insulating floors for the nanowire devices. Since Au is rather inert and does not adhere well to these substrates, a very thin (25 angstrom) Ti adhesion layer was first evaporated onto the patterned substrates. Subsequently, the Au was evaporated onto the substrate without breaking vacuum in the e-beam evaporator.

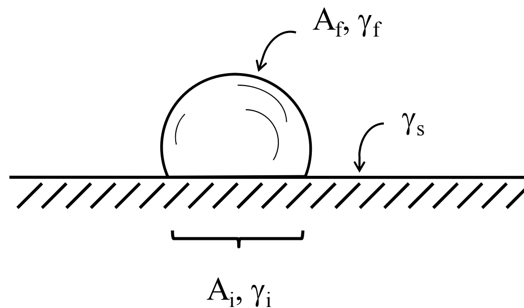

Figure **2-6**: Geometry of condensate nucleus formation on a substrate [3].

$$\sum_k \gamma_k A_k = Minimum \qquad \textbf{2.1}$$

2.1.3.2 Gold Evaporation Procedure

It is well-known that the morphologies of evaporated Au films and nanowires differ between tools and processing conditions [4]. In this research two e-beam evaporators (Kurt Lesker and Semicore, Figure **2-7**) were used and compared for depositing the Ti/Au films. A quartz crystal thickness monitor (QCM) was used for real-time monitoring of deposition rates and film thicknesses. In the Kurt Lesker tool, the base pressure was pumped to below 2.5 x 10^{-6} Torr with a cryo pump before initializing the Ti e-beam evaporation. To start the evaporation, the beam current was ramped through a soak procedure until the desired deposition rate of 0.5 A/s was achieved. A shutter near the substrate blocked the metal vapor during the beam current soak. During the soak, the Ti vapor gettered the chamber of oxygen and a drop in deposition pressure was observed. Once the chamber pressure stabilized, the shutter was opened and the Ti was deposited onto the substrate. The QCM was monitored during the deposition and once 2.5nm of Ti was evaporated, the shutter was closed. The beam current was then gradually reduced and finally turned off. The Au crucible was then selected on the tool. The Au used in the evaporation was 99.999% purity, purchase from Kurt Lesker. Similar to the Ti deposition, a soak procedure was used until the 0.5A/s deposition rate was achieved. The deposition was monitored with the QCM and aborted by closing the shutter once the desired film thickness was achieved. The film thicknesses varied between 20nm to 30nm, depending on which set of experiments the nanowires were used for.

Figure **2-7**: Kurt Lesker (Left) and Semicore (Right) Evaporators at the PSU Nanofab.

The Semicore evaporator produced a smoother and more continuous film than the Kurt Lesker. This was due to three main factors: lower achievable base pressures (< $1x10^{-6}$ Torr), lower deposition pressures, and better centering of the substrate over the evaporation source. Similar to the Kurt Lesker, the e-beam evaporations were done in a crucible with 99.999% purity Au. A QCM was used to determine the deposition rates and film thickness; however, the shutter was nearer to the evaporation source and prevented deposition rate monitoring until the shutter was opened. Once the soak cycle was complete and the shutter was opened, a feedback control loop automatically adjusted the power to maintain the desired deposition rates. Otherwise, the deposition procedures were very similar. Neither evaporator had the option for substrate heating / cooling; therefore, all of the depositions were performed with the substrate at the temperature inside the chamber.

The deposition rate used here, 0.5A/s, is relatively low for e-beam evaporation of Au; it was selected because slower deposition rates result in more ordered films [5]. The reason for this is described as follows: In the deposition process, the vapor first reaches the substrate where it is physisorbed. These atoms diffuse along the surface until they are captured by energetically favorable chemisorption sites. If, however, the next monolayer is deposited before the atoms are able to diffuse to these sites, then they are incorporated into the film. The activation energy required to diffuse in the surface is greater than on the surface; therefore, the higher evaporation rates gives less time for the atoms to redistribute on the surface and result in less ordered films.

2.2 Nanowire Device Characterization

The fabricated nanowire and thin film devices were characterized using optical microscopy, field-emission scanning electron microscopy (FESEM), and atomic force microscopy (AFM). These techniques enabled us to evaluate the line-width, side-wall roughness, thickness, morphology, and average grain-size of the nanowires.

2.2.1 Field Emission Scanning Electron Microscopy Analysis

The SEM analysis demonstrated our ability to design an extensive range of Au wires widths and also revealed the limitations of the e-beam lithography tool for forming these structures. Both multiple and single nanowire devices were fabricated and characterized for our sensor application (Figure **2-8**). The SEM analysis showed that the

minimum nanowire width obtained in our experiments was 30nm; however, most of the wires used in our sensors were 40nm due to low yield in the wires with smaller dimensions. The largest wire line-width was 1μm. We consider this to be a thin film, because above a 200nm line-width, the interactions of the electrons with the sidewalls of the wire are negligible to the overall electrical properties. The wire length spanned the distance (10-20μm) between adjacent electrical contact pads in all device configurations.

The SEM was used to verify the dimensions, geometry, and spacing of the nanowires and electrical contact pads after fabrication. Additionally, it was used to determine the roughness and continuity of the nanowires. The images revealed that the sidewalls of the nanowires were rough. This level of roughness is expected when fabricating sub-100nm line-width wires with e-beam lithography and lift-off processing [1]. The wires with line-widths greater than 100nm also exhibited some level of side-wall roughness; however it is less apparent in these wires since the undulations are much smaller than the line-width.

Although the SEM was useful for measuring dimensions, geometry, and sidewall roughness of the nanowires, it lacked the resolution and contrast required for determining the grain size. Therefore, a combination of AFM and SEM was used to approximate the grain sizes. This process is discussed in further detail in the subsequent section on AFM analysis.

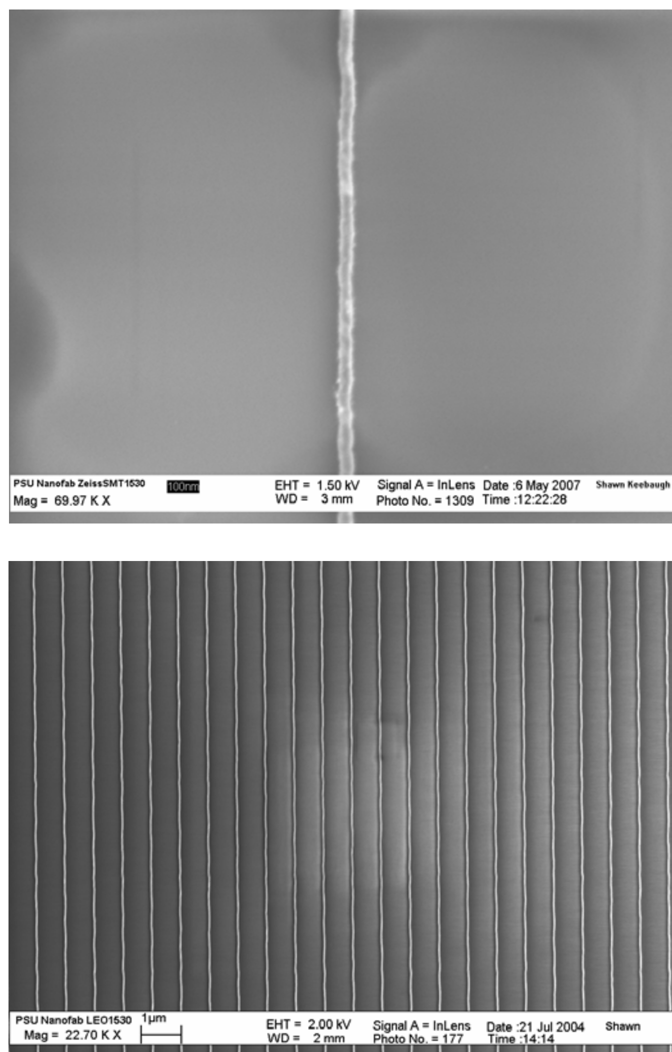

Figure **2-8**: (Top) FESEM image of a single gold nanowire approximately 40nm wide. (Bottom) Nanowires in parallel with a pitch of 700nm. The edges of the lithographically defined nanowire are rough.

2.2.2 Atomic Force Microscopy Analysis

AFM analysis was used to determine the thickness, morphology, and average grain size of the nanowires and films. The AFM used in this study (Veeco© Dimension 3100 AFM) is capable of giving angstrom vertical resolution, but is limited in lateral

resolution due to the distortions created by the tip diameter, slope, and edge instabilities. The AFM tool was operated in tapping mode to help mitigate the problems associated with edge instabilities [6]. Both Veeco and WsXM software [7] were used to analyze the data and produce the AFM images displayed here. For example, Figure **2-9** shows 2-D, 3-D, and cross-sectional AFM images of a 1μm Au film and the Pt electrical contact pad. The cross-sectional view was used to verify that the correct thickness of Pt was evaporated for the contact.

The surfaces of the nanowires were rough, having approximately 20% thickness variations along their length. This level of roughness was expected due to the island-like nucleation of gold on oxides and nitrides. However, depending on the fabrication procedure, the nanowires could have thickness variations approaching the thickness of the deposited film; i.e., they were discontinuous nanowires. If the DI water rinse step was omitted in the e-beam resist development procedure (i.e. only IPA was used), then the nanowires' were more likely to produce a rough and irreproducible morphology (Figure **2-10**). Alternatively, the addition of the DI water rinse step resulted in smooth, highly reproducible morphologies.

The DI water rinse step helped to remove residues on the substrate prior to the metal deposition. It is possible these residues would inhibit the adhesion of the evaporated metals to the substrate. As previously mentioned, the nanowire morphology depends strongly on the interfacial energy at the metal-substrate interface; these results underscore this point and also open up the possibility of tailoring the interfacial properties to produce nanowires with a desired roughness and morphology.

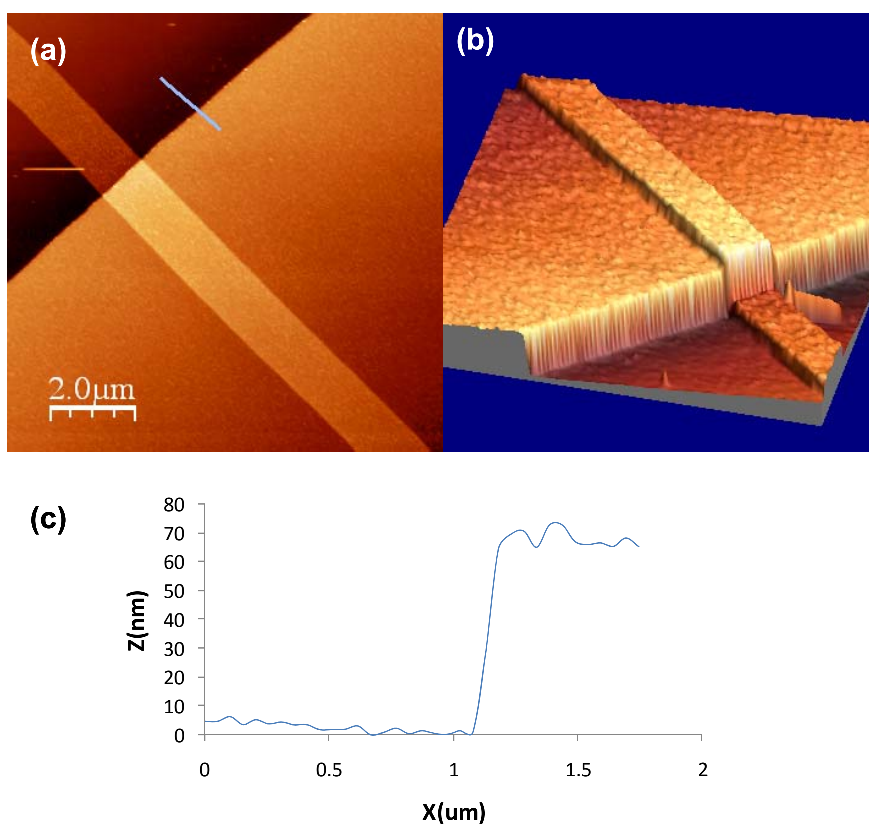

Figure **2-9**: AFM images of a 1μm Au thin film and the Pt electrical contact pad. (a) 2-D image, (b) 3-D image, and (c) cross-sectional profile showing the step between the substrate and electrical pad (70nm thickness); this cut was taken from image (a).

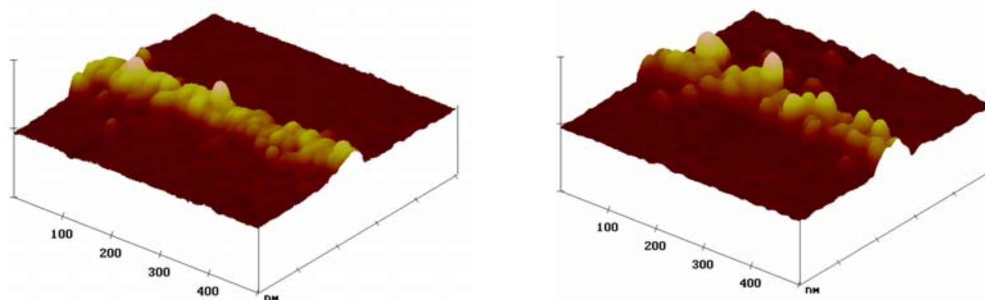

Figure **2-10**: Three-dimensional AFM images of Au nanowires with the DI rinse step omitted. The morphology is very rough and irreproducible.

The nanowires were separated into two categories depending on their level of surface roughness: smooth and continuous nanowires or rough and discontinuous nanowires. The smooth and continuous wires come from the batches which received the DI rinse step at the e-beam resist development procedure. The others come from the batches that did not. These categories are used only to describe the relative differences in roughness and continuity of the nanowires as determined from the AFM and electrical characterizations. They are not meant to be used as a criterion for categorizing nanowires fabricated outside of this work.

2.2.2.1 Smooth Continuous Nanowires

AFM analysis was performed on the smooth, continuous nanowires (Figure **2-11**). It may be seen in the image that the individual grains in the wire are resolved. On average, there are only two grains across the width of the wire. SEM analysis showed that the wire width was approximately 40nm. Therefore, we can take the average grain size to be approximately 20nm. This happens to be within 20% of the nanowire thickness. The average of the cross-sectional profile of a nanowire is given in Figure **2-12**. It may be seen in this image that there is a small positive offset from zero at the substrate and that the average nanowire thickness is 28nm. According to the QCM used in the Semicore e-beam evaporator, the Ti thickness was 2.5nm and the Au was 25nm. Therefore, we conclude that the Semicore QCM gives accurate thickness measurements of the films used in this work.

The roughness of the nanowires was determined by using the power spectrum function in the WsXM software. A profile cut was taken in the center-line, along the length of the nanowires. The average of the nanowires was 5nm and the roughness between 2 and 3nm.

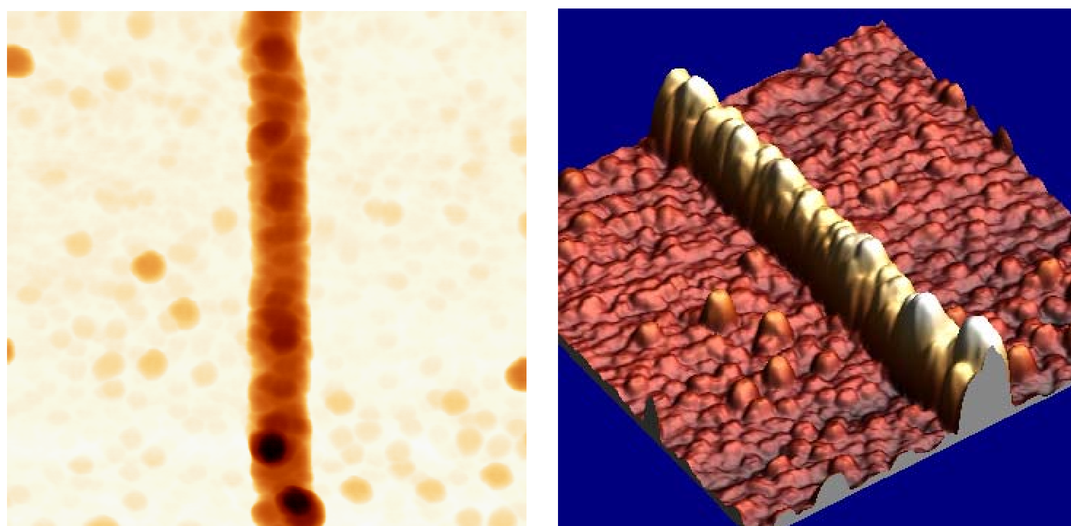

Figure **2-11**: AFM image highlighting the grain-boundaries in the gold nanowire (Left). 3-D image of the nanowire (Right).

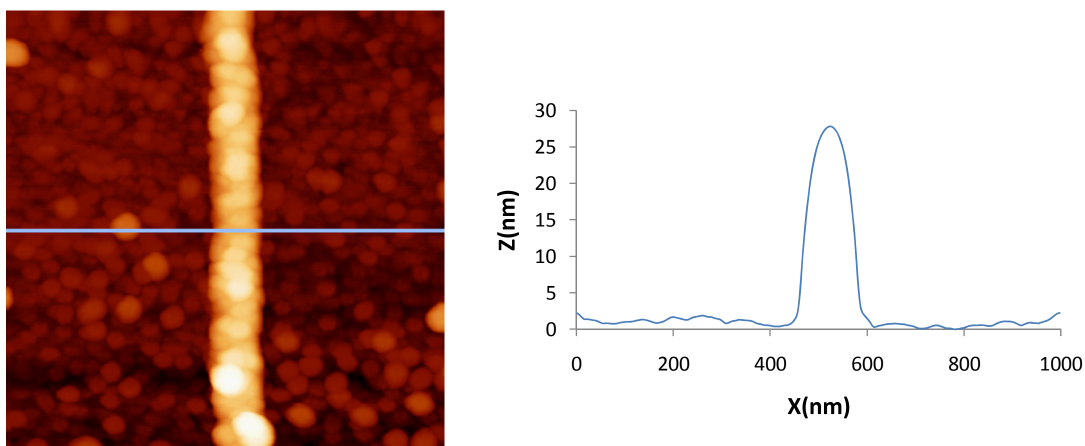

Figure **2-12**: Cross-sectional cut of nanowire and a plot of the average nanowire thickness.

2.2.2.2 Rough Discontinuous Nanowires

The AFM images (Figure **2-13**) of the rough, discontinuous nanowires illustrates the island-like or particle-like quality of the wire. Additionally, the cross-sectional profile shows a region of the wire that is much thicker than what was recorded on the QCM (25nm). The SEM analysis showed that the wire width varied more than the smooth wires. By comparing the images of the smooth nanowires and taking profile cuts in the AFM software, we can approximate some particles to be as large as 40nm. The roughness of the nanowires was determined by using the power spectrum function in the WsXM software. A profile was taken in the center-line, along the length of the wires. The average was 10nm and the roughness between 4 and 5nm.

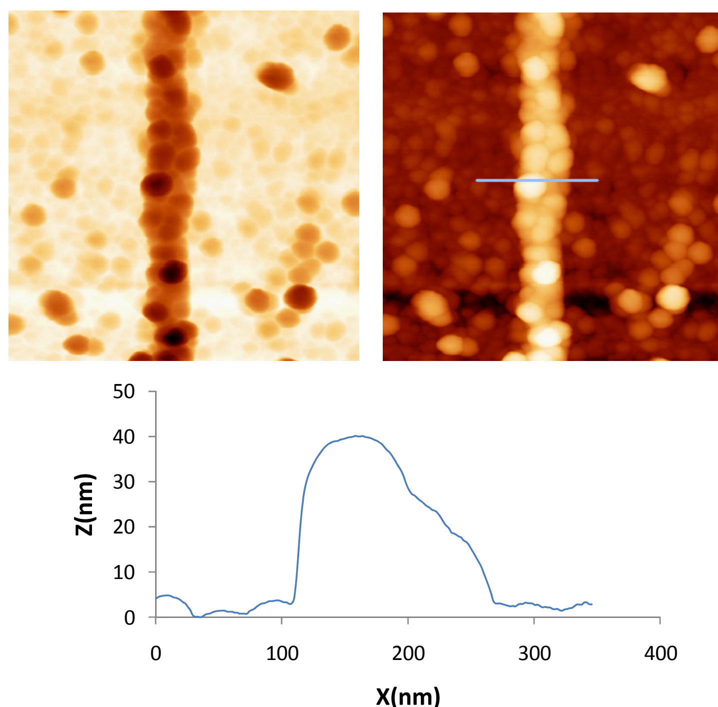

Figure **2-13**: AFM image of rough, discontinuous wire and a profile showing the particles are much thicker in regions than what was recorded on the QCM.

2.3 Summary

To summarize, we have fabricated Au nanowires and thin films using e-beam lithography, e-beam evaporation, and other standard processing techniques. The line-widths ranged from 30nm to 1μm and the thicknesses between 20 and 30nm. SEM analysis was used to verify the dimensions, geometry, and spacing of the nanowires and electrical contact pads after fabrication. AFM analysis was used to determine the thickness, morphology, and average grain size of the nanowires and films. The nanowire characterizations revealed that alterations in the fabrication procedure could produce nanowires with smooth and continuous, or rough and discontinuous morphologies. The cause of this was found to be the surface condition prior to metal evaporation.

2.4 References

1. D. Natelson, *Recent Developments in Vacuum Science and Technology*, 157 (2003).

2. D. Smith, *Thin-Film Deposition: Principles & Practice*, McGraw-Hill, Boston (1995).

3. J. Anderson, *Chemisorption and Reactions on Metallic Films*, Academic Press Inc., New York (1971).

4. G.P. Zhigal'skii and B.K. Jones, *The Physical Properties of Thin Metal Films*, Taylor and Francis, New York (2003).

5. M. Ohring, *The Materials Science of Thin Films*, Academic Press, London (2002).

6. D. Schroder, *Semiconductor Material and Device Characterization*, John Wiley and Sons, Hoboken, New Jersey (2006).

7. I. Horcas, R. Fernandez, J.M. Gomez-Rodriguez, and J. Colchero, *Review of Scientific Instruments*, 78, 013705 (2007).

Chapter 3

Electrical Characterization of Gold Nanowires

3.1 Background on the Electronic Properties of Metals

Soon after the discovery of the electron, Drude put forth a model for explaining the electrical conduction of metals [1]. At that time, a metal was thought to be comprised of atoms containing a heavy, positively charged nucleus, core electrons bound to the nucleus and valence electrons which were shared by all of the atoms and formed an electron gas. This electron gas supplied an attractive force which glued the positively charged ions together (Figure **3-1**). By assuming the electron gas picture, Drude applied the kinetic theory of gases to explain the motion of the conduction electrons. This model was experimentally confirmed for many metals, but some anomalies were later found. Although this model was not completely accurate, a few modifications can be applied to the model to give a very reasonable description of conduction in metals including metallic thin films and nanowires. For example, recently, researchers applied this model to explain the conductance change of gold thin films exposed to mercury vapor [2].

After the development of quantum theory, Sommerfeld built upon Drude's Theory by asserting that the electrons must be governed by Fermi-Dirac statistics. He applied these principles to explain the distribution of energy and velocity for the free electrons in the electron sea. For most metals, the electrons have a large velocity even as the temperature approaches *0K*.

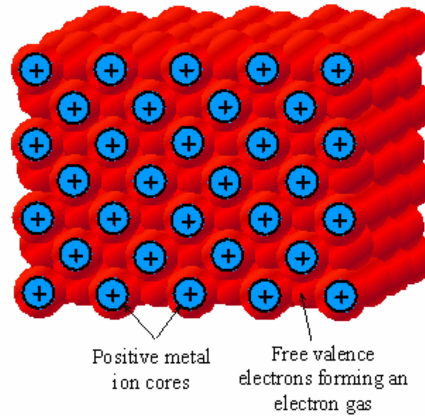

Figure **3-1**: Metal modeled as a lattice of positive ion cores surrounded by a sea of free valence electrons [1].

This contradicts the explanation given by the kinetic theory of gases, where the translational kinetic energy was equated to $E=3kT/2$. Here, the electron velocity can be derived by equating its kinetic energy to the Fermi energy. The Fermi energy is the energy at which, all states above this level are empty and all beneath this level are full at $T=0K$. The Fermi energy has a very small temperature dependence as can be seen in Eq. **3.1**.

$$E_F(T) = E_{F0}\left[1-\frac{\pi^2}{12}\left(\frac{kT}{E_{F0}}\right)^2\right] \quad \mathbf{3.1}$$

where E_F is the Fermi Energy, E_{F0}, is the Fermi Energy at 0K, k is the Boltzmann constant, and T is the temperature.

Eventually, a more accurate model for the description of electron conductions was given by the band theory of metals where a full quantum mechanical description is given to the electron in a periodic potential, $U(r)$ [1]. The Schrodinger equation of the crystal is

given by Eq. **3.2.** The electrons, named Bloch electrons, satisfy this equation and are described by a wave equation Eq. **3.3**.

$$\left[\frac{-\hbar^2}{2m_0}\nabla^2 + U(r)\right]\psi(r) = E\psi(r) \quad \textbf{3.2}$$

$$\psi_k(r) = e^{ik\bullet r}u_k(r) \quad \textbf{3.3}$$

For metals, we can simplify these expressions by assuming the background potential is screened and the E-k relationship becomes Eq. **3.4** [3].

$$E(k) = E_C + \frac{(\hbar k)^2}{2m_0} \quad \textbf{3.4}$$

A pictorial description of the band theory is shown in Figure **3-2** . As the inter-atomic spacing between the atoms decreases, the wavefunctions interfere with one another and the atoms' discrete energy levels split into bands of energy. The spacing between the energy levels within the band is small relative to *kT* and can therefore be thought of as a continuum of energy. The bands containing in the conduction electrons or holes are the called conduction band and valence band respectively. For metals, the spacing between the conduction band and valence band is negligibly small or overlaps.

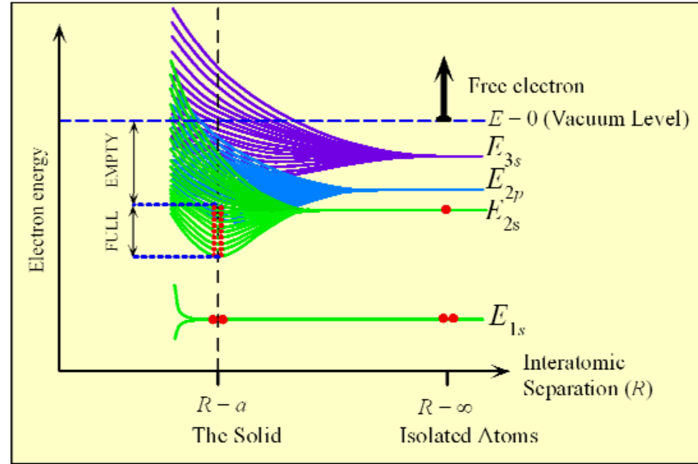

Figure **3-2**: Energy band formation of a metal [**1**].

3.2 Electron Scattering in Metals

The nanowires used in this research have lengths much greater than λ; therefore, they fall into the diffusive transport regime and the current-voltage characteristics are described by Ohm's law Eq. **3.5**.

$$J = \sigma E \qquad \textbf{3.5}$$

where E is the electric field, J is the current density, and σ is the conductivity. The conductivity, σ, is the proportionality constant between J and E and is given by Eq. **3.6**

$$\sigma = \frac{ne^2\tau}{m_e} = ne\mu \qquad \textbf{3.6}$$

where, n is the number of carriers/cm^3, e is the electronic charge, τ is the mean free time, m_e is the mass of the electron, and μ is the electron mobility. Additionally, the electron mobility is the proportionality constant between the drift velocity and applied electric

field; i.e., $v_d=\mu E$. If we assume that we are applying a voltage V, along the length of the nanowire with a current I, then $V=EL$ and $J=I/A$, and the electrical resistance, R, of the nanowire is given by Eq. **3.7**

$$R = \frac{\rho L}{A} \qquad \textbf{3.7}$$

where, L is the length of the wire, A is the cross-sectional area, and $\rho=1/\sigma$ is the electrical resistivity. Therefore, the electrical resistivity is inversely related to the average time, τ, between electron scattering events.

As mentioned above, we can make an approximation that the sea of electrons in a metal screens the underlying potential and the free electron energy is purely kinetic (KE). The average electron velocity can then be calculated by equating the KE to the Fermi Energy as in Eq. **3.8.**

$$KE = \frac{1}{2} m v_F^{\ 2} = E_F$$
$$v_F = \sqrt{\frac{2E_F}{m}} \qquad \textbf{3.8}$$

where v_F is the Fermi velocity. Most metals have v_F on the order of 10^8cm/s [**4**], so the electrons are randomly moving in the metal with a very high velocity and are scattering with phonons, electrons, impurities, defects, and the metal surface. The average distance the electron travels between collisions is termed the mean free path, λ, and is given by Eq. **3.9.** The electrical size effects appear when λ approaches the line-width, thickness, or average grain size of the nanowires. For bulk Au, $\lambda \approx 40$nm; therefore, the size effects become apparent in the devices that were discussed in Chapter 2. The mean-free-path

can be affected by several scattering mechanisms; the primary mechanisms include: phonon scattering, impurity and defect scattering, surface scattering, and grain-boundary scattering. Matheissen's Rule states that the scattering events are additive and independent.

$$\lambda = v_F \tau \quad \textbf{3.9}$$

3.2.1 Phonon Scattering

Phonons are quanta of lattice vibrations and are described by Bose-Einstein statistics. They are the dominant electron scattering mechanism in the nanowires in the 50-300K temperature range. For these temperatures, the Bose-Einstein model (Eq. **3.10**) suggests the number of phonons is proportional to the temperature; therefore, the number of phonon scattering events should also be linear with temperature. According to Matheissen's rule, the scattering mechanisms are additive and linear. Therefore, it is expected that the electrical resistivity is linear with temperature for continuous metallic thin films and nanowires in the 50-300K temperature range [1][3].

$$n_p \propto \frac{1}{\exp\left(\frac{\hbar\omega}{kT}\right) - 1} \propto \frac{kT}{\hbar\omega} \quad \text{for } T > 50K \quad \textbf{3.10}$$

3.2.2 Impurity and Defect Scattering

Fabricating a pure and defect free metal nanowire is impractical. The impurities and defects disrupt the lattice periodic potential and scatter the electrons. Impurity and

defect scattering, along with electron-electron scattering are the dominant scattering mechanisms responsible bulk metal resistivity below 50K. In this temperature range phonon scattering is negligible and the resistivity has a $\rho \alpha T^5$ dependence [1][3]. As the temperature approaches 0K, the resistivity is frequently called the residual resistivity of the metal. Other scattering mechanisms may also contribute to the residual resistivity if the dimensions and grain sizes approach the mean free path of the conduction electrons.

3.2.3 Surface Scattering

As the dimensions of a film or wire approach the mean free path of the conduction electrons, they will experience a larger fraction of scattering at the metal-vacuum interface. A physical model explaining the increase in resistivity due to surface scattering in thin films was first reported by Fuchs [5] and Sondheimer [6] and is commonly referred to as the *FS* theory for surface scattering. This model has been used to successfully explain the increase in resistivity measured in thin metal films [7][8][9].

In the FS model, an electron may have either a specular scattering event or a diffuse scattering event at the film surface. For specular scattering, the momentum is conserved in the direction of drift; i.e., the angle of incidence is equal to the angle of reflection. In diffuse scattering, however, the momentum is not conserved and the electron is randomly reflected at the film surface. Consequently, specular scattering events do little to affect the drift velocity and diffuse scattering events decrease it. In this model, the important parameters are the thickness of the film, the mean free path of electrons in the metal, and the proportion of electrons that are scattered diffusely at the

surface of the film. The parameter, *p*, is used to explain the proportion of electrons specularly scattered at the surface and may vary between 0 and 1 with 0 being perfectly diffuse scattering and 1 being perfectly specular scattering. As one might expect, the *p* value depends strongly on the surface roughness of the nanowires. For rough surfaces the scattering is more diffuse, and for smooth surfaces it is more specular. The *FS* model has described many times, the dependence of resistivity on film thickness. Currently, the model has been used to explain the resistivity increases in metallic nanowires due to surface scattering. The nanowires differ from the film because they have two dimensions confined (width and thickness) instead of one (thickness). The following example illustrates this point. Electrons in a pure, bulk metal move randomly at the Fermi velocity and have an equal likelihood of being scattered in all three dimensions (***x***,***y***,*z*) Figure **3-3** .

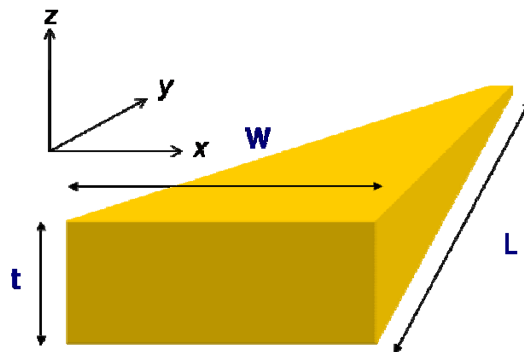

Figure **3-3**: Three dimensional illustration of an ideal film or nanowire.

On average, an electron will travel the mean-free-path (~40nm for Au) before scattering. However, in a thin-film with a thickness on the order of the *mfp*, the electrons are

confined in the z-direction and are forced to scatter at this surface more frequently than the x,y-directions. The p value determines whether the scattering event will affect the overall resistivity. Furthermore, nanowires confine the electrons in two-dimensions (x,z). Depending on the nanowire geometry and dimensions, the frequency of scattering events in the x-direction can be equal to or more than the z-direction. Therefore, scattering at the side-wall can be equally significant to affecting the overall resistivity of the metal as scattering at the top surface.

3.2.4 Grain Boundary Scattering

FS theory alone was unable to successfully describe the resistivity increases found in thin films with sub-100nm thicknesses. Mayades and Shatzkes found that the average grain diameter typically decreased with film thickness and attributed the higher resistivity to electron scattering at the grain-boundaries [**10**]. This model, known as the *MS* theory for grain-boundary scattering, is applicable for nanowires and films with grain diameters approaching λ. The most important parameter in the *MS* theory is the reflection coefficient at the grain boundaries. The reflection coefficient, R, is the average probability that an electron will be reflected at a grain-boundary. This value can range between 0 to 1, with 0 being no reflection at the grain-boundary and 1 being complete scattering at the grain boundary. Unless single crystalline, most metallic nanowires will have multiple grain-boundaries between electrical contacts; therefore, it should be emphasized that R is an average scattering probability for all the grain-boundaries between contacts and not a measure of an individual boundary. Current models rely on a

combination of *MS* and *FS* theories to explain the resistivity anomalies due to size effects [11][12][13][14][15]. The two scattering mechanisms are additive, and their relative contribution to resistivity change depends on the nanowire dimensions, morphology, and grain-diameters.

3.3 Electrical Conduction in Metallic Nanowires

It is well known that the resistivity of metallic thin films increase as the thickness approaches the dimensions of the mean-free-path (λ) of the conduction electrons. More recently it has been demonstrated that similar principles apply to metallic nanowires with lateral dimensions approaching λ. The increase in resistivity is due to the additional surface and grain-boundary scattering at this size scale. Matheissen's rule states that the scattering events are additive and independent of each other. Therefore, the total resistivity of a nanowire can be expressed as Eq. **3.11** below:

$$\rho_{Total} = \rho_0(T) + \rho_{ss} + \rho_{gb} \qquad \textbf{3.11}$$

where ρ_{Total} is the total resitivity, $\rho_0(T)$ is the phonon-scattering dominated, temperature dependant component of resistivity, ρ_{ss} is the component of resistivity due to surface scattering, and ρ_{gb} is the component of resistivity due to grain-boundary scattering. A more detailed expression for the nanowire resistivity, which combines the Fuchs-Sondheimer (*FS*) theory, for surface scattering and the Mayadas-Shatzkes (*MS*) theory for grain-boundary scattering, is given by Eq. **3.12** below [16]:

$$\rho = \rho_0 \left\{ \frac{\frac{1}{3}}{\left[\frac{1}{3} - \frac{\alpha}{2} + \alpha^2 - \alpha^3 \ln\left(1 + \frac{1}{\alpha}\right) \right]} + \frac{3}{8} C (1 - p) \frac{1 + AR}{AR} \frac{\lambda}{w} \right\} \quad \textbf{3.12}$$

with $$\alpha = \frac{\lambda}{d} \frac{R}{1 - R}$$

where w is the width, AR is the aspect ratio (thickness over width), ρ_0 is the resistivity of the bulk material, λ the *mfp*, d the average distance between grain-boundaries, p the specularity parameter, R the reflectivity coefficient at the grain-boundary, and C is a constant equal to 1.2 for rectangular cross-sections.

The important parameters in this equation are the p and R values. As explained earlier, the p value describes the proportion of electrons that scatter specularly at the nanowire surface. This value can vary between 0 and 1. A p value of 1 would indicate perfectly specular scattering and a p value of 0 would indicate completely diffuse scattering. A wide range of p values have been reported for polycrystalline Au wires. This is expected since the imperfections at the surface of the wire will depend on the method of fabrication. The R value is the probability that an electron will be reflected at a grain-boundary. This value can also vary between 0 and 1 and has been reported to be as high as 0.9 for polycrystalline Au wires [17]. The R value can be experimentally determined by measuring individual grain-boundaries; however, this measurement is by no means trivial. The p and R values for nanowires are generally determined by fitting Equation 3.9 to a plot of the resistivity vs. line-width (Figure **3-4**). The fit obtained is not

unique; therefore, a large amount of uncertainty in fitted parameters (*p* and *R*) is usually observed. In additional, the model assumes that *p* and *R* are independent of line-width. In many cases, this assumption is reasonable; however, one can expect the model to break down if the surface roughness or grain-boundary barrier height or width varies with line-width.

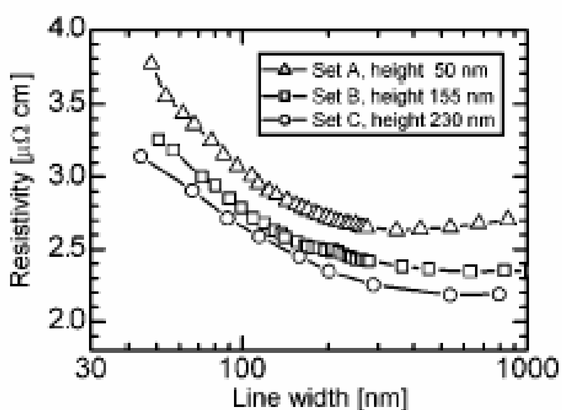

Figure **3-4**: Experimental data of the resistivity dependence upon Cu line-width and thickness. Equation 3.9 was fit to the curves to determine the *p* and *R* values for the different nanowire thicknesses [**16**].

3.3.1 Effects of Size on Electrical Resistivity

The effects of line-width on the electrical resistivity of gold nanowires were studied by fabricating four-point, single nanowire devices with thicknesses of 20nm and various line-widths: 30nm, 40nm, 50nm, 75nm, 100nm, 200nm, 500nm, and 1μm. The nanowire sizes and geometries were verified with SEM and AFM measurements and were subsequently characterized with an Agilent 4156C Semiconductor Parameter Analyzer. This tool consisted of four high-resolution, low-noise source monitor units

(SMUs) capable of independent current and voltage measurements. The devices were measured inside a shielded box by first placing them on a chuck and contacting them with a probe station which was connected to the four SMUs via tri-axial cables. The probes were contacted to the Pt contact pads and current was forced through the outer two electrodes and the voltage differential was measured across the inner two. The applied current was 10μA for all line-widths except for the 500nm and 1μm line-widths. 100μA was applied to these devices in order to keep the measured voltage differential in the mV range. The current at each probe was monitored ensuring there was no leakage between contacts. The four-point configuration eliminated the contact resistance from the measurements and allowed for accurate measurements of the wire resistance. Once the resistance data was collected, the wire dimensions were used to calculate the nanowire resistivity.

The smallest continuous nanowire line-width we fabricated with the e-beam lithography tool was 30nm. The largest width was 1μm, not because of fabrication limitations, but because for larger line-widths, the electrons are only confined in 1-D and surface scattering at the side-walls is negligible. SEM and AFM analysis were combined to approximate the grain diameter for all the wires and films to be 20nm.

A plot of the electrical resistivity vs. line-width for the gold nanowires and thin-films is shown Figure **3-5.** The curve is relatively flat for the wires with 100nm-1μm line-widths. However, below 100nm, the resistivity increases sharply; it goes from 6.6μΩ-cm at the 100nm line-width to 20.2μΩ-cm at the 30nm line-width. Our nanowires ranged from three to nine times greater than the bulk electrical resistivity, $\rho_{0,}$ for Au (2.2μΩ-cm). This suggests there was a substantial amount of surface and grain-boundary

scattering in the wires. These results are consistent with other reports in the literature where the size effects have been investigated [**18**][**19**]; however, our nanowires have a stronger dependence on line-width (sub-100nm) than most others.

We attempted to extract the surface scattering and grain-boundary scattering parameters *p* and *R* by using the *FS-MS* scattering model and fitting it to the experimental data. The curve fitting functions in Origin (Version 8) and Mathematica (Version 7) were utilized for these efforts. In the model, we used the bulk Au resistivity (2.2μΩ-cm) for ρ_0, the bulk *mfp* of Au (41.8nm) for λ, 20nm for the average grain-diameter, *d*, and 20nm for the wire thickness. The parameter constraints were set $0 \leq p \leq 1$ and $0 \leq R \leq 1$ and the simulation was run. The results indicated that the fit was very poor and the parameter uncertainty near the constraint limits. This was not surprising considering the level of uncertainty in *p* and *R* reported elsewhere (e.g. [**16**]).

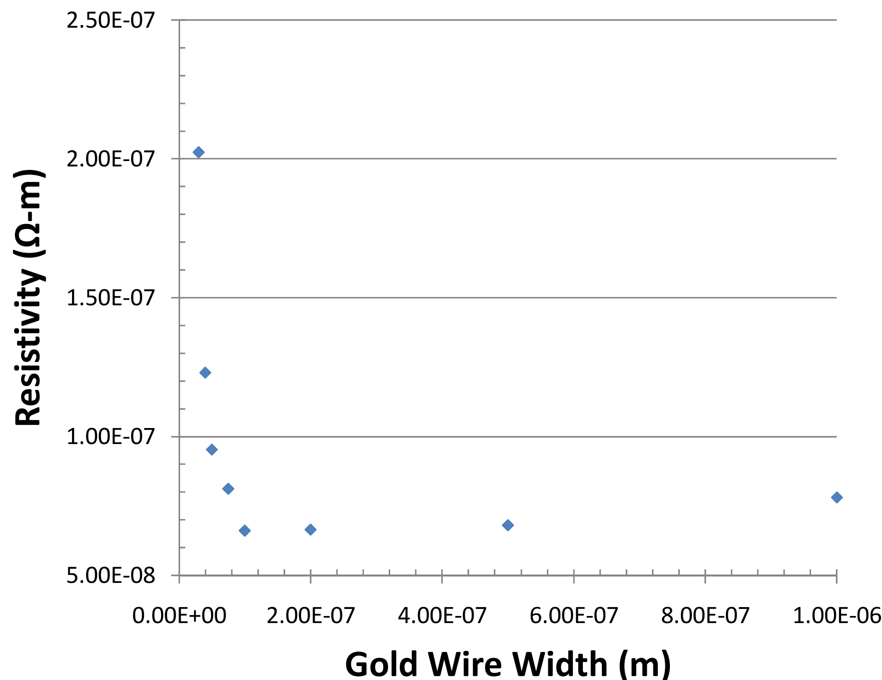

Figure **3-5**: Plot of the electrical resistivity vs. line-width for gold nanowires and thin-films with constant 20nm thickness.

The difficulty in using this model is accounting for the precipitous upturn of resistivity for line-widths below 100nm. The model assumes that *p* and *R* are independent of line-width. We know, however, that the roughness for the nanowires is greater than the thin-films. This suggests that unless the surface scattering is completely diffuse, the nanowires have a lower *p* value than the films. Additionally, we know from SEM and AFM characterization that the nanowires only have two to three grain-boundaries across their width. Because of this, the statistical fluctuations in the reflection coefficients at individual boundaries can have a drastic impact the electron transport. This notion is supported by a recent report where individual Au grain-boundary reflection coefficients were measured [**20**]. They showed that the *R* values at the individual boundaries varied

substantially along the wire length and suggested an improved model is required to account for electron percolation. For example, in a thin-film, the electrons have many possible conduction paths and can miss the high-*R* boundaries by percolating around them; where as in a nanowire, the electrons have few conduction paths and are more likely to cross the high-*R* regions. Although useful, we believe that the assumptions in the *FS-MS* model prevent us from accurately determining the average *p* and *R* parameters in our wires.

3.4 Dependence of Electrical Resistance on Nanowire Morphology

A nanowire's surface structure plays an important role in determining its electrical properties. A wide range of nanowire morphologies are possible; they can range from smooth and continuous, where scattering events dominate the electron transport, to rough and discontinuous, where tunneling and hopping dominate [**21**]. Since the nanowire electrical resistance depends strongly on the morphology, we used the resistance measurements to verify the fabrication step responsible for the nanowire roughness.

The devices used in this study were fabricated using the standard fabrication procedure (Chapter 2) up to the e-beam resist develop step. At this point, the wafer was cleaved in half; one half received the IPA rinse and the other half received IPA and DI water rinse. After this step, the pieces were processed together through completion, ensuring the rinse procedure was the only difference in processing. The completed two-point devices contained single nanowires, 40nm wide and 20nm thick. We measured the

I-V response of the finalized nanowire devices with the 4156C and extracted resistance values from the inverse slope of the curve. Figure **3-6** is the I-V plot of the Au nanowires that received the DI water rinse. The average resistance of these nanowires was 19.7kΩ and the standard deviation was 3.1kΩ. Figure **3-7** shows an I-V plot of the nanowires which received the IPA rinse only. The average nanowire resistance is approximately 1GΩ because four of the nanowires were electrically discontinuous. However, if only the electrically continuous nanowires are considered, they have an average resistance of 60.1kΩ with a 49.7kΩ standard deviation. The average resistance is nearly three times larger and the standard deviation more than an order of magnitude higher than the smooth wires.

The resistance and morphology data establish several points about our nanowires: First they indicate that the surface condition prior to the Au evaporation is indeed responsible for altering the nanowire morphology. Second, they demonstrate that the nanowires with smooth morphologies are less resistive and have less variability between devices than those with rough morphologies. Last, they show that the nanowire fabrication procedure with the DI rinse is more robust and reproducible than the alternative procedure.

The resistance values of the smooth nanowires fall into the expected range for continuous nanowires. The electron transport is most likely dominated by the various scattering mechanisms. On the other hand, several of the rough nanowires have resistance values which are orders of magnitude larger than the smooth nanowires. This is probably because the inter-grain barriers are wider and approach the attenuation length of the tunneling electrons. In such a case, there could be a transition from scattering-

dominated to tunneling and hopping-dominated conduction. Additionally, since the nanowires only have two to three grains across their width, the transition could be easily dominated by only a few grain-boundaries.

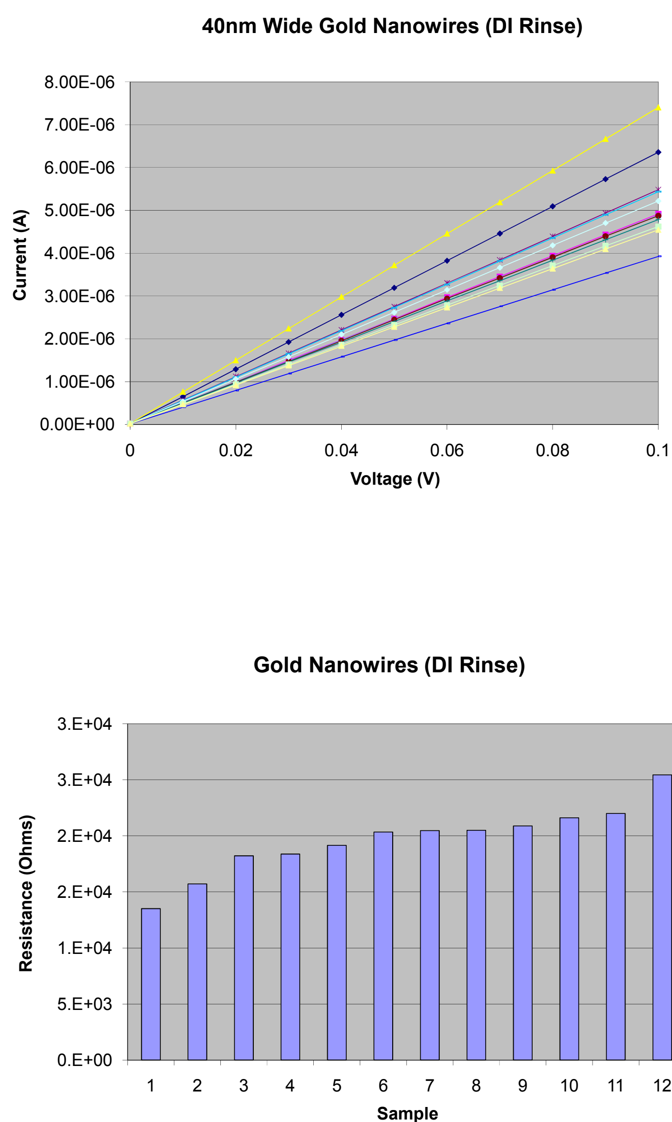

Figure **3-6**: I-V curves of 40nm wide Au nanowires that received the DI rinse (top). Bar chart highlighting the variability in resistance between nanowires (bottom).

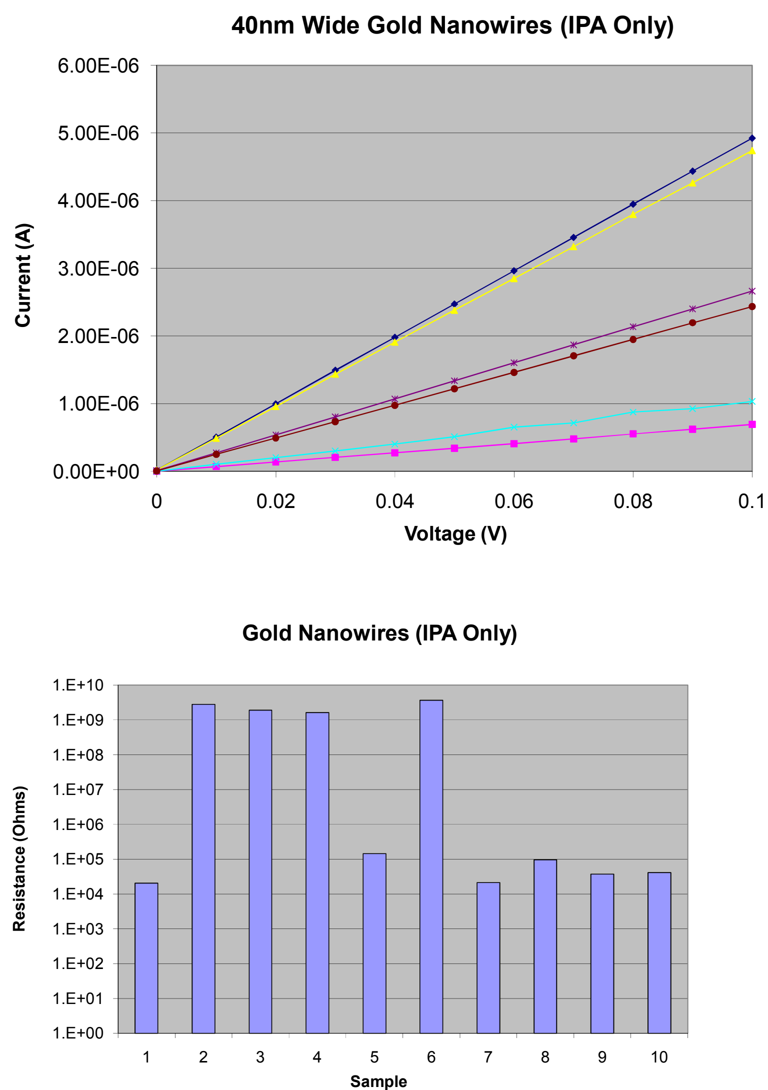

Figure **3-7**: I-V curves of 40nm wide Au nanowires that received the IPA rinse only (top). Bar chart highlighting the variability in resistance between nanowires (bottom). **Note: Plot is logarithmic on the y-axis.**

3.5 Temperature Dependence of Resistivity

Exploring the nanowire temperature dependence of resistivity is useful because it provides information regarding the nanowire electron transport mechanisms, the various electron scattering mechanisms, and the level of disorder in the nanostructures. For example, the temperature independent components of the resistivity (e.g. ρ_{SS}, ρ_{GB}) show up as the residual resistivity, ρ_0, for temperatures approaching 20K. For continuous nanowires, the resistivity is dominated by electron-phonon scattering and ρ α T for temperatures ≥ 100K. However, if the nanowires are disordered, instead of having a constant residual resistivity, they show an upturn at low temperatures. This type of behavior is attributed to the disorder-induced localization of the electrons [**22**].

If the nanowire transport is diffusive and dominated by electron scattering, it is expected that the temperature coefficient of resistance [**23**], α_R, given by Eq. **3.13**, will be linear at temperatures above 100K. This is due to the linear relationship between phonon scattering and the temperature dependent portion of the resistivity in Eq. 3.7.

$$\alpha_R = \frac{R}{R_0}\frac{1}{\Delta T} \qquad \textbf{3.13}$$

where R_0 and R are the initial and final resistances respectively and $\Delta T = T_1 - T_0$ is difference between the initial and final temperatures. The temperature dependence of resistivity was explored in our nanowires using the following experimental setup and procedure.

3.5.1 Experimental Setup and Procedure

Single nanowire devices with smooth morphologies were fabricated for the low temperature resistivity experiments. The nanowires were 21nm thick and had widths of 30nm, 75nm, 100nm, and 200nm. Four-point resistance measurements were performed on the nanowires with the 4156C by forcing a current through the outer two electrodes and measuring the voltage drop across the inner two electrodes. Current and voltage data were collected from each of source monitor unit probes ensuring no current leakage between the electrodes. The resistance was then calculated from Ohm's law: $R = V/I$. Preliminary two-point resistance measurements showed anomalous resistance values at temperatures below 50K. We were concerned that this was due to contact resistance changes at low temperatures; therefore, the four-point configuration was used in favor of the two. The nanowire resistivity was then calculated from the resistance measurements and the average cross-sectional area, $\rho = R \times A/L$. For these calculations the nanowires were assumed to have ideal, rectangular cross-sections.

The temperature of the nanowires was controlled inside a Biorad Digital DLTS System cryo-chamber which had an operating range of 25-300K. This system consisted of a temperature controlled vacuum chamber which was connected to a liquid helium cryogenic pump. A thermocouple inside the chamber measured the chuck temperature and displayed it real-time on a digital readout. Additionally, the chamber contained an electrical probe station which was connected to the 4156C through sealed coaxial feed-throughs. Once the chamber and 4156C were connected, a nanowire device was loaded into the chamber and pumped down to the base pressure (0.5mbarr). Next, the tool was

prompted to incrementally cool the chamber to the minimum stable chuck temperature (30K). The slow cooling process helped prevent any thermal shock of the devices. Once the temperature stabilized at 30K, the probes were contacted to the device and the resistance was measured. The probes were then removed from the device and the temperature was increased to the next data point. This was done to keep the probes from scratching the device as the temperature was ramped. Once the tool stabilized at this temperature, the probes were contacted to the device and a resistance measurement was again performed on the device. The temperature was incremented up to 300K and resistance measurements were made at each increment.

3.5.2 Results and Discussion

Figure **3-8** shows a plot of the resistivity vs. temperature for the nanowires in the 30-300K temperature range. It can be seen that the resistivity has a linear dependence on temperature above 50K. These results confirm the continuity of our nanowires and that their transport is dominated by phonon scattering at temperatures above 50K. It may also be seen in the plot that the smaller line-widths exhibit larger electrical resistivity for the entire temperature range. This is expected since the temperature change should have little effect on the resistivity increases from surface scattering, grain-boundary scattering, and impurity scattering. The slope of each curve, $\partial\rho/\partial T$, was determined by fitting a straight line to each data set in the 50-300K temperature range. These values, along with the corresponding α_R and line-widths are reported in Table **3-1.** The slope of the 30nm wide wire was approximately twice as large as the rest of the wires. This was unexpected

since the electron-phonon interaction size effects should not show up for nanowires with these dimensions [24].

Table **3-1**: $\partial\rho/\partial T$ and α_R vs. gold nanowire line-width.

Wire Width	$\partial\rho/\partial T$ (Ω-m/K x10^{-11})	Temperature Coefficient of Resistance, α_R
30 nm	17.01	4.20 x 10^{-3}/K
75 nm	8.87	3.96 x 10^{-3}/K
100 nm	7.18	3.99 x 10^{-3}/K
200 nm	7.55	3.82 x 10^{-3}/K
(Bulk Au)	4.0	3.82 x 10^{-3}/K

The nanowires have *TCR* values within 10% of bulk Au. There is a small increasing trend in the *TCR* with decreasing line-width. It is unclear if this trend has physical importance or if it is due to measurement error. Other researchers have observed the inverse of this trend in Cu nanowires; i.e., the *TCR* decreased with decreasing line-width. They attributed this to the increased surface scattering and the thermal coefficient of expansion mismatch between the metal and underlying substrate. We are not ruling out the possibility that a similar effect is occurring in our nanowires, but lack enough evidence to support it.

Below 50 K we observed an upturn in the nanowire resistivity for all nanowire line-widths. The temperature was cycled and the phenomenon was found to be reversible and independent of the sweep direction. According to the Bloch-Gruneisen [24] formula, the nanowires should exhibit $\rho \alpha T^5$ behavior below 50K and flatten out to the residual resistivity ρ_0 at even lower temperatures. Although the upturn in resistance was unexpected, similar results have been reported elsewhere in the literature. Three possible explanations exist for this behavior: (1) impurity scattering, (2) metal to insulator

transition due to disordered nanowire structure, or (3) a thermal mismatch between nanowire and underlying substrate.

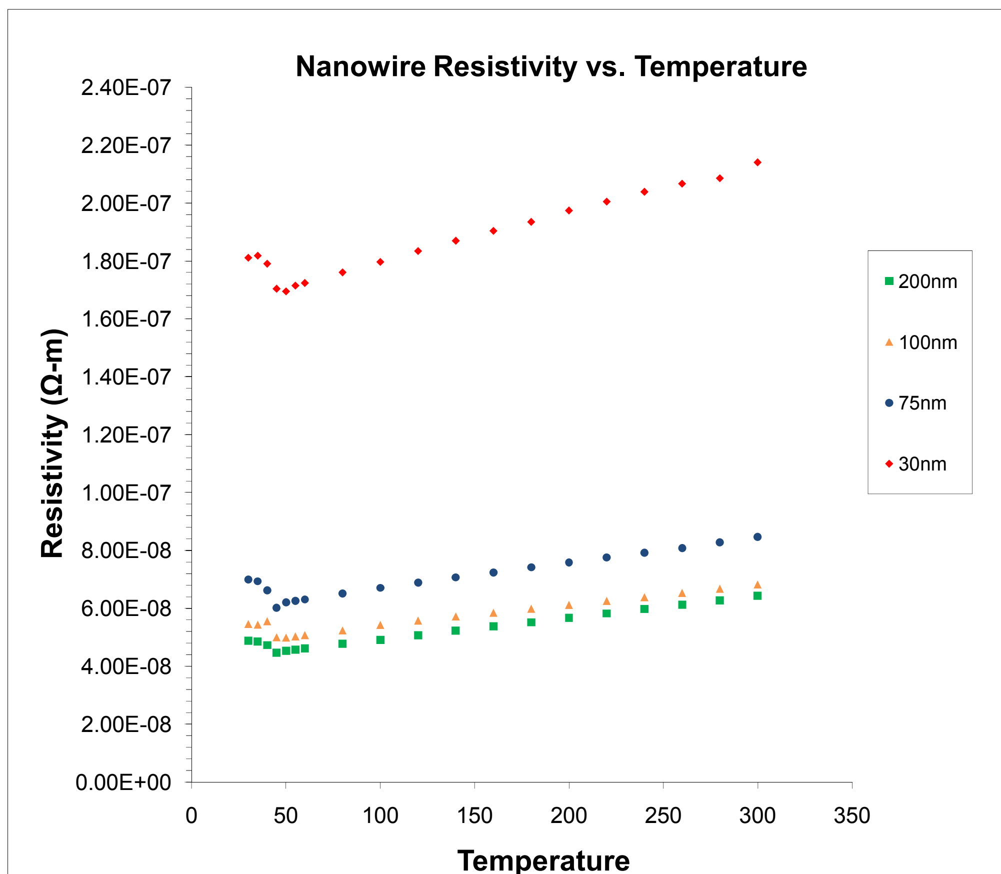

Figure 3-8: Nanowire resistivity plotted against temperature.

Impurities in the gold nanowire can alter its low temperature electrical resistance. As the temperature decreases, so does the carrier velocity; therefore, the impurity scattering increases. This behavior can result in an upturn in the resistance. The impurities in the nanowires could be a consequence of cross-contamination in the processing tools, because they are used by multiple users running various processes. Additionally, localized magnetic impurities can act as strong scattering centers for

carriers at low temperatures. This type of scattering is described by the Kondo effect [25]. The only condition for this to occur is that the temperature be cooled to below the Kondo Temperature of the metal. For most metals, this is usually on the order of 10K. The temperature where we observed the upturn in resistance is much higher than expected for the Kondo Temperature. Therefore, it is unlikely that the phenomenon can be described well by the Kondo Effect.

The second possible explanation for the upturn in resistance is due to the disorder in the nanowire structure [22]. The electron wave-functions in a random potential may be substantially altered if the level of disorder is strong enough. In such cases, instead of being an extended state, the electrons become localized and at low enough temperatures they have a metal-to-insulator transition; i.e., as $T \rightarrow 0$ the conductivity goes from being finite to zero. The polycrystalline nanowires obviously have some level of disorder; however, the effects do not typically show up until $T \leq 10K$. Therefore, the level of disorder is unlikely the source of the upturn in resistance we see at 50K.

The third possible explanation for the upturn in resistance is a mismatch in the thermal coefficient of expansion between the Au nanowire and thermal oxide [23]. The thermal coefficient of expansion for Au is 1.420×10^{-5} K^{-1} and for SiO_2 it is 5×10^{-7} K^{-1}. Therefore, as the material cools, the Au will shrink faster than the SiO_2 and will undergo significant tensile stress. It is plausible the strain in the nanowire could be large enough to cause a separation between grains and an increase the barrier width. In such cases, one would expect the electron tunneling probability to decrease and the electrical resistivity to increase. Furthermore, negative *TCRs* have been reported for discontinuous films.

Therefore, we conclude that either the mismatch in thermal coefficients of expansion or impurity scattering is causing the observed upturn in resistance below 50K.

3.6 Summary

To summarize, we have reported on the electrical characterization of our Au nanowires. The wires were characterized with four point electrical resistivity measurements for line-widths ranging from 30nm to 1μm. The resistivity was found to increase substantially for line-widths smaller than 100nm. A widely used model for surface and grain-boundary scattering was introduced to explain this phenomenon. The model inadequately described the phenomenon in our wires because of the assumption that the specularity parameter and reflection coefficient are independent of line-width. Two-point resistance measurements were performed on Au nanowires with varying morphology. It was found that the rough nanowires were more resistive and less reproducible than the smooth wires. Furthermore, we found that the surface condition prior to the Au evaporation was strongly related to the resulting nanowire morphology. Finally, the temperature dependence of resistivity was reported on. The nanowires exhibited a linear increase in resistivity with temperature for temperatures above 50K. These results underscore the continuity of the nanowires and indicate phonon-dominated scattering in this temperature range. The temperature coefficients of resistance were extracted from the data and found to be within 10% of the bulk Au value. In addition, an upturn in resistance was observed at temperatures below 50K. This behavior was

unexpected and attributed to either increased impurity scattering or the mismatch in thermal coefficients of expansion for the nanowires and substrate.

3.7 References

1. S.O. Kasap, *Principles of Electronic Materials and Devices*, McGraw Hill: New York (2006).

2. V. Raffa, B. Mazzolai, V. Mattoli, A. Mondini, and P. Dario, *Sensors and Actuators B*, 114, 513 (2006).

3. J. Singh, *Electronic and Optoelectronic Properties of Semiconductor Structures*, Cambridge University Press: New York (2003).

4. N.W. Ashcroft and N.D. Mermin, *Solid State Physics*, Brooks Cole, 1976.

5. K. Fuchs and H.H. Wills, *Proceedings of the Cambridge Philosophical Society*, 34, 100 (1938).

6. E.H. Sondheimer, *Advances in Physics*, 1, 1 (1952).

7. M.S.P. Lucas, *Journal of Applied Physics*, 36, 1632 (1965).

8. K.L. Chopra and M.R. Randlett, *Journal of Applied Physics*, 38, 3144 (1967).

9. D. Schumacher, *Thin Solid Films*, 152, 499 (1987).

10. A.F. Mayadas and M. Shatzkes, *Physical Review B*, 1, 1382 (1970).

11. C.Durkan and M.E. Welland, *Physical Review B*, 61, 14215 (2000).

12. W. Steinhogl, G. Schindler, G. Steinlesberger, and M. Engelhardt, *Physical Review B*, 66, 075414 (2002).

13. J.J. Plombon, E. Andideh, V.M. Dubin, and Jose Maiz, *Applied Physics Letters*, 89, 113124 (2006).

14. H. Marom, M. Ritterband, and M. Eizenberg, *Thin Solid Films*, 510, 62 (2006).

15. H. Marom, J. Mullin, and M. Eizenberg, *Physical Review B*, 74, 045411 (2006).

16. W. Steinhogl, G. Schindler, G. Steinlesberger, M. Traving, and M. Engelhardt, *Journal of Applied Physics*, 97, 023706 (2005).

17. M.A. Schneider, M. Wenderoth, A.J. Heinrich, M.A. Rosentretter, and R.G. Ulbrich, *Journal of Electronic Materials*, 26, 383 (1997).

18. D. Josell, C. Burkhard, Y. Li, Y.W. Cheng, R.R. Keller, C.A. Witt, D.R. Kelley, J.E. Bonevich, B.C. Baker, and T.P. Moffat, *Journal of Applied Physics*, 96, 759 (2004).

19. J. Camacho and A. Oliva, *Microelectronics Journal*, 36, 555 (2005).

20. A.Bietsch and B. Michel, *Applied Physics Letters*, 80, 3346 (2002).

21. C.A. Neugebauer and M.B. Webb, *Journal of Applied Physics*, 33, 74 (1962).

22. P. A. Lee and T.V. Ramakrishnan, *Reviews of Modern Physics*, 57, 287 (1985).

23. G.P. Zhigal'skii and B.K. Jones, *The Physical Properties of Thin Metal Films*, Taylor and Francis: New York (2003).

24. A. Bid, A. Bora, and A.K. Raychaudhuri, *Physical Review B*, 74, 035426 (2006).

Chapter 4

Gold Nanowire Mercury Sensors

4.1 Introduction

Nanosensors have generated much interest due to their exceptional performance (response, sensitivity, recovery time, etc.), ease of integration, and ability to exploit phenomena observed at the nanoscale. Many different types of nanostructures have been used for sensing and detection applications; examples found in literature include: nanocantilevers [1][2], nanowires [3][4][5], nanoparticles [6][7], and nano-structured materials [8]. Of these, metallic nanowires are excellent candidates because of their high surface to volume ratio, ease of integration into sensor arrays, and inherent selectivity to adsorbed species. In addition, the surface dependent electrical size effects become very important once the dimensions of the nanowire approach the mean-free-path (*mfp)* of the conduction electrons [9][10]. This phenomenon can be exploited and utilized to develop electrical nanowire sensors capable of high sensitivity to surface adsorption. Furthermore, one-dimensional nanowire geometry forces minimized electron-percolation paths which can be used to maximize a sensor's response to absorbed species [5].

With this in mind, a manufacturable and highly responsive Au nanowire sensor capable of detecting ppb concentrations of Hg in air and water was developed. The nanowire sensor exhibits a superior response compared to thin film sensors and it has been observed that this response is closely related to the morphology of the nanowire. By

carefully controlling the sensor fabrication steps, one can obtain reproducible smooth, continuous nanowire morphologies and consequently obtain highly responsive and reproducible sensors.

4.1.1 Motivation for Mercury Sensing with Gold Nanowires

Mercury is a severe neurotoxin whose presence in the environment has increased three-fold since the beginning of the industrial revolution. Coal-fired power plants are the major emitters of mercury which enters the food cycle via the air and water (Figure **4-1**). With the emergence of surging economies around the globe and the demands on oil and coal supplies, the potential for further mercury contamination is rapidly increasing. Environmental Protection Agency (EPA) data shows that approximately one in every six pregnant women has enough mercury in their body to inhibit the full development of a fetus. It also shows that one quarter of the mercury in the U.S. comes from domestic sources while the rest comes from other regions globally. The EPA has proposed mandates to drastically reduce the amount of mercury released into the environment. As part of their roadmap, they have listed a need for improved environmental sensing and detection techniques [**11**].

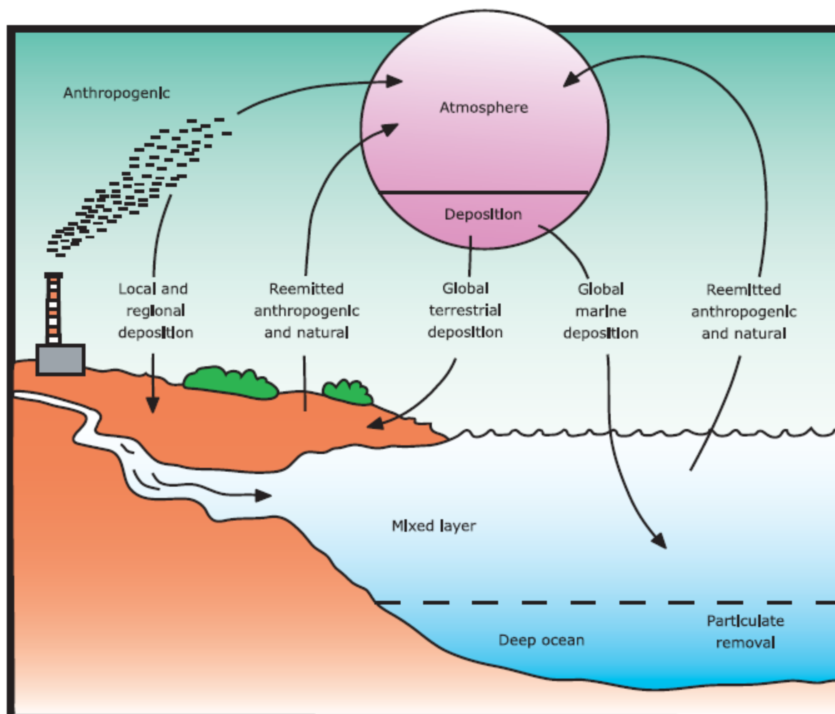

Figure **4-1**: Illustration of the mercury cycle [11].

To monitor Hg levels, quick and reliable means of both elemental and ionic Hg detection are required. Several different kinds of sensors have been developed for the detection of Hg in air and water [12][13][14][15]. Of these the most common monitors changes in the conductivity of a Au thin film upon exposure to Hg [12][15]. This sensor design, unlike many of the more complicated designs is easy to fabricate, requires no optics, and is small and portable, allowing for on-site, real-time detection. Exposing such a sensor to Hg causes an Au-Hg amalgam to be formed at the Au surface and results in an increase of the electrical resistance [12][16]. This increase has two possible contributors: increased surface scattering due to the formation of an Hg amalgam at the surface or decreased conductivity due to the lower conductivity of the amalgamated region. Due to

the importance of the surface in this Hg sensing, decreasing the thickness of an Au thin film increases the surface to volume ratio, and thereby offers the opportunity to enhance the sensor response. To further improve the response, a nanowire geometry exhibiting a high surface to volume ratio and dimensions approaching the *mfp* of the conduction electrons in Au is desirable. With this in mind, we set out and developed Hg sensors based on our Au nanowire devices.

4.1.2 Adsorption of Mercury on Gold

It has been known for a long time that Hg is extremely reactive toward Au and has a very high sticking coefficient to its surface. Its adsorption decreases the Au work-function φ_{Au} by ½ eV and was responsible for inaccurate measurements of φ_{Au} until the late 1960s [17]. Several groups have studied Hg adsorption on Au surfaces using techniques such as AFM, XPS, SIMS, and STM [18][19][20][21][22][23][24]. These studies make a few points as it applies to our nanowire sensor applications. First is that the sticking coefficient of Hg on Au is near unity up to the first monolayer and the surface reaction occurs almost instantaneously. The reaction depends on the Hg vapor concentration and saturates quickly to reduce the sticking coefficient of subsequent Hg layers. Second, Hg is very mobile on the Au surface, diffuses into grain-boundaries, and agglomerates at defect sites; therefore, polycrystalline Au has greater uptake of Hg than single crystalline Au and is not limited to single monolayer adsorption. The last point is that Hg vapor reacts with Au to form amalgam clusters which roughen the Au surface.

4.1.3 Electrical Effects of Mercury Adsorption on the Gold Nanowires

Four models can be used to explain adsorption induced electrical resistivity changes of a metal [25]. The first model depends primarily on the surface to volume ratio and ignores the relationship between the wire dimensions and *mfp* of the electrons. This model is typically used to describe electrical conduction changes of thick films or metals that have a relatively small electron *mfp*. It states that when a chemical adsorbs on the metal surface, a thin layer is modified resulting in a resistivity different from the bulk of the material. Consequently, the measured resistivity of the nanowire will change upon adsorption and can be thought of as two resistors in parallel.

The second model emphasizes the adsorption induced surface scattering and is used to explain conduction changes in metals having partially specular surfaces (Figure **4-2**) and dimensions approaching the *mfp* of the conduction electrons. As long as the surface scattering is not already completely diffuse, there will be an increase in resistivity due to a change in the specularity parameter upon adsorption. However, if the original surface is already rough and the scattering is completely diffuse, the additional material can cause a decrease in the resistivity and is better explained using the previous model.

The third model can be applied if the chemical diffuses into the grain-boundaries and/or bulk of the material. In the former case, the chemical absorption can affect the probability that an electron will be scattered at the grain-boundary, hence changing the reflection coefficient. In the latter case, the absorption of the chemical can change the bulk resistivity of the nanowire. The one-dimensional nanowire geometry also minimizes

electron-percolation paths and can be used to improve the nanowire sensor's response to the absorbed species.

Finally, there is the case that that the nanowires are only semi-continuous and do not behave according to the Drude-Sommerfield theory for conduction in metals. In such a case, electron conduction is dominated by tunneling and hopping and is dependent upon the work-function of Au and the spacing between the grains or particles.

In reality, most nanowires experience adsorption onto their surface and subsequent adsorption into the grain-boundaries and bulk of the material. In such cases, a model capable of explaining changes in the bulk conductivity, surface scattering, and grain-boundary scattering of the nanowire is desired. In the case of Hg adsorption on polycrystalline Au films, George *et al.* summarized the primary mechanisms for the increased electrical resistance [26]: (1) Surface scattering from sites occupied by Hg, (2) grain-boundary scattering from Hg occupying grain-boundaries, (3) scattering from defect regions where sufficient concentrations of Hg have adsorbed to lead to amalgamation.

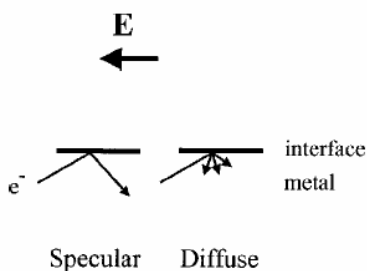

Figure **4-2**: Illustration of difference between specular and diffuse scattering. An incoming electron (e^-) strikes the metal surface and for specular reflection, the component of momentum along the applied filed (indicated by *E* and the arrow) is conserved, whereas for diffuse reflection, it is not and the reflected electron has a random direction of momentum, thus reducing the net current flow [9].

4.2 Sensor Response to Hg Vapor – WKU Experiments

4.2.1 Experimental Setup and Procedure

The sensing response of these nanowires to elemental Hg was first explored using the facilities of the Combustion Laboratory at Western Kentucky University. Sensors containing multiple nanowires between the electrical contacts were used for this work, and the testing apparatus consisted of a glass test chamber that was connected by Teflon tubing to an Hg vapor generator at its inlet and to an analyzer at its outlet (Figure **4-3**).

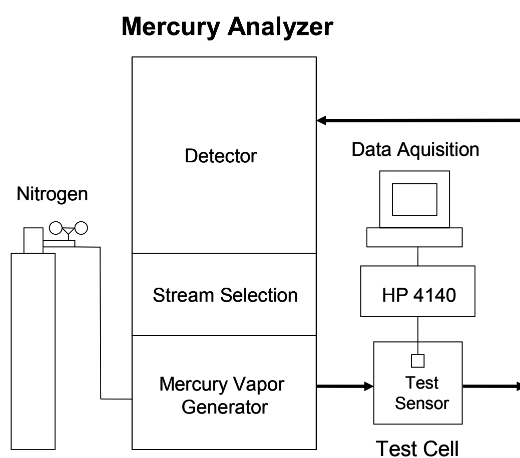

Figure **4-3**: Mercury vapor generator set-up used for the initial experiments on the gold nanowire array sensor.

This configuration allowed us to very precisely monitor the concentration of Hg entering and exiting the test chamber. Nitrogen was used as a carrier gas and was maintained at a constant flow rate of 750ml/min whether or not Hg vapor was entrained. During the Hg exposure, a 100mV potential was applied between the electrical contacts using an HP4140 and the resistance was measured as a function of time for Hg concentrations

ranging from 5ppb to 35ppb. Testing was typically performed until the resistance saturated.

4.2.2 Results and Discussion

The response of nanowires exhibiting the rough morphology is irreproducible. Figure **4-4** is an example of such a sensor. For this sensor, the resistance decreases upon Hg adsorption. One possible explanation for this behavior is that the conduction may be dominated by inter-particle tunneling. In such a case, the adsorption of Hg onto the Au surface may reduce the height and width of the tunneling barrier and hence decrease the resistance. The other possibility is that scattering on the original surface is completely diffuse and the addition of a thin Au-Hg amalgam layer decreases the resistance. However, given the vapor concentration and magnitude of resistance change, it is unlikely the amalgam could have significantly increased the effective cross-sectional area of the wires. Furthermore, the nanowires with the rough morphology are very sensitive to temperature fluctuations and will change their baseline electrical properties at the temperatures needed for sensor regeneration. The response of nanowires exhibiting the smooth morphology, achieved either due to our pre-deposition approach or our post-deposition electrical stress (see Chapter 5) approach, is highly responsive and reproducible Figure **4-5**. These sensors have a very predictable behavior: the resistance increases after Hg adsorption and generally saturates after a long exposure.

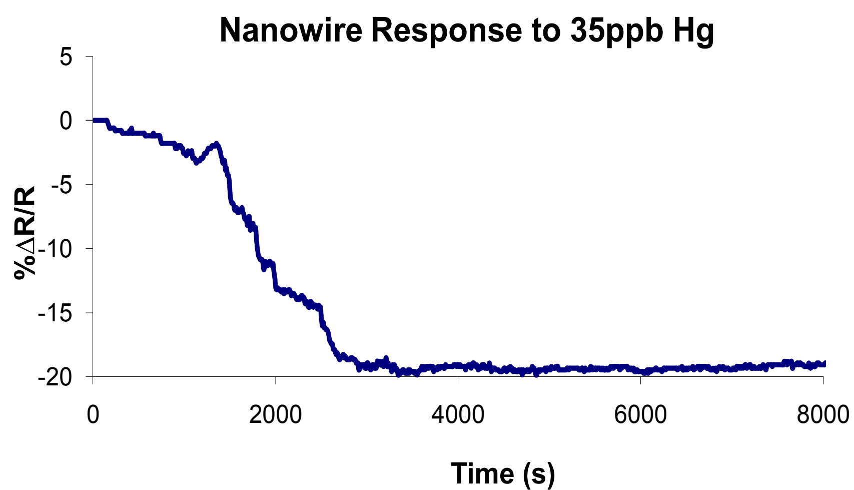

Figure **4-4**: Response of a nanowire sensor (rough morphology) to elemental Hg.

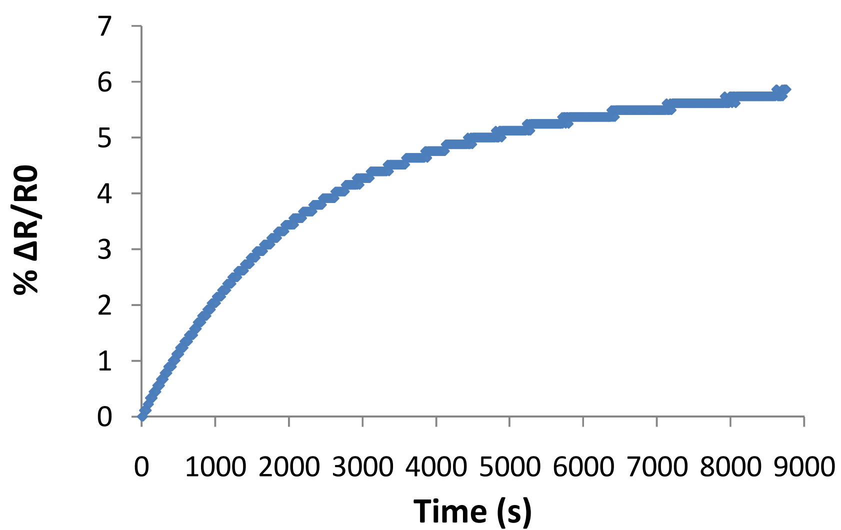

Figure **4-5**: Response of Au nanowire array (50 wires) to 18ppb Hg vapor.

4.3 Sensor Response to Hg^{2+}

4.3.1 Experimental Setup and Procedure

The sensing response to Hg^{2+} was explored using $HgCl_2$ dissolved in DI water at concentrations ranging from 10^{-4} to 10^{-8}M. The response of thin-film, single wire, and multiple wires were exposed to this Hg ion source and were compared. During the Hg^{2+} exposure, a 100mV potential was applied across the sensor. The resistance was first monitored in air for approximately 120s. Afterward, a micropipette was used to introduce a 2.5μL drop of the solution between the electrical contact pads and directly onto the nanowires (Figure **4-6**).

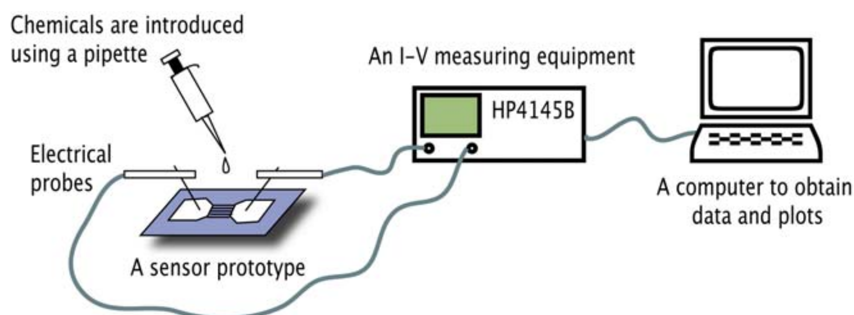

Figure **4-6**: Setup for ionic mercury detection experiments.

Resistance measurements were performed for approximately 300s beyond the introduction of the solution or until saturation in resistance was observed. To ensure that actual sensitivity to ionic Hg was detected and not shunting ionic currents, we verified that, for the concentrations used here, the measured ionic current between electrodes (Figure **4-7**) was three or more orders of magnitude smaller than the current carried in the

nanowires at the same voltage bias (i.e. 100mV). Other electrolytes, including 1μM to 1mM aqueous solutions of $CuCl_2$, $MgCl_2$, and NaCl, were introduced onto the sensing area to further insure ionic currents were not detected and also to demonstrate the selectivity of the sensor to Hg^{2+}.

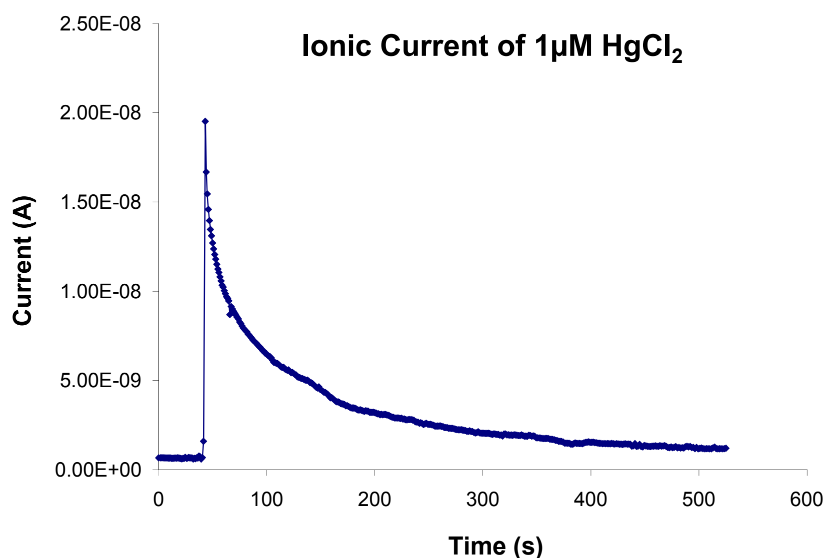

Figure **4-7**: Ionic current of 1μM $HgCl_2$ between two Pt electrical contact pads.

4.3.2 Results and Discussion

In the case of Hg^{2+} detection, three different concentrations (10^{-4}, 10^{-5}, and 10^{-6} M) of the $HgCl_2$ aqueous solution were applied to the surface of the Au nanowire sensors and the response was measured as a function of time Figure **4-8**. As in the case of elemental Hg detection, the response of the sensor was observed to increase systematically with the concentration of the applied solution. The Hg^{2+} detection limit, defined here as the lowest concentration at which increases in the resistance were

distinguishable from noise after a 300 s exposure, was found to be 10^{-8}M for Au nanowire devices that were 40 nm wide and 20nm thick. It is likely that the poorer concentration detection limit seen for Hg^{2+} in comparison to elemental Hg is due to the necessity of ancillary chemical reactions at the wire surface which are needed to maintain charge neutrality [27].

4.3.3 Kinetics Modeling

Adsorption/absorption of mercury causes local Fermi level and potential fluctuations at the Au nanowire surface, inducing significant diffuse surface scattering and grain-boundary scattering. Because the dimensions of the nanowires are on the order of the electron *mfp*, the contribution of surface scattering must be linearly additive with the grain-boundary, electron-electron, and electron-phonon scattering.

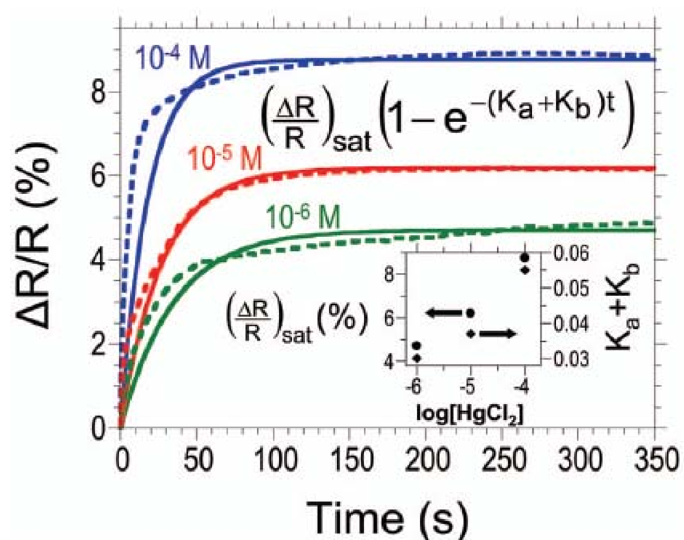

Figure **4-8**: Nanowire sensors' response to varying $HgCl_2$ concentrations. Solid and dashed lines represent the experiment and modeling, respectively.

Thus, as a first approximation, the resistance increase may be assumed to be linear with the amount of Hg adsorbed on the nanowire surface, which we term *N*. If we use the model that the net Hg adsorption rate is equal to the rate of adsorption at available (unoccupied) states, minus desorption from sites where Hg has already adsorbed, then we obtain Eq. **4.1**

$$\dot{N}(t) = K_a\left[N_t - N(t)\right] - K_d N(t) \qquad \textbf{4.1}$$

which is solved to give Eq. 4.2

$$N(t) = \frac{K_a N_t}{K_a + K_d}\left(1 - e^{-(K_a + K_d)t}\right) \qquad \textbf{4.2}$$

Here, t is the Hg exposure time, N_t is the total number of available sites for adsorption, and K_a and K_d are rate constants for the adsorption and desorption, respectively. Figure 4-8 shows the fitting of the kinetics data for three different concentrations of $HgCl_2$. In the simplest case for $[Hg^{2+}]$ adsorption, the rate of adsorption would be linear with Hg concentration; i.e., $K_a = ka[Hg^{2+}]$ where ka is a constant. With this expression for K_a, the saturated resistance change scales with $ka[Hg^{2+}]\ N_t/(ka[Hg^{2+}] + K_d)$. As seen from Figure 4-5 and its inset, $(\Delta R/R_0)$ at saturation has a weak and sublinear dependence on $[Hg^{2+}]$ in the concentration range explored in this study. This suggests either (a) $K_a = ka[Hg^{2+}]$ and $K_a > K_d$, or (b) $K_a \neq ka[Hg^{2+}]$. When the kinetics data are fit to our model, the dependence of $(K_a + K_d)$ on $[Hg^{2+}]$ is seen to be weak and sublinear, as determined from the exponent of the exponential term. As seen in the inset of Fig. 4-5, $(K_a + K_d)$ varies by

less than a factor of 2 when [Hg^{2+}] changes by 2 orders of magnitude. If we assume (a) is valid, we are faced with the fact that K_a varies by less than a factor of 3 while [Hg^{2+}] changes by 2 orders of magnitude, since $K_a > K_d$ by assumption (a). Therefore (a) is not consistent and can be ruled out. In other words, dependence of K_a on [Hg^{2+}] is weak and not linear. This supports assumption (b) and implies that adsorption of Hg on Au is not rate limited by [Hg^{2+}] but by another mechanism. Possibly the major rate-limiting mechanism involves the electron transfer at the nanowire while Hg^{2+} is being neutralized upon adsorption. Or perhaps the absorption of Hg, in this concentration range, is better described using a different model for adsorption.

4.3.4 Surface to Volume Ratio

To test the model that the sensitivity ($\Delta R/R$) is arising from Hg interaction at the nanowire surface and to demonstrate the relationship between surface to volume ratio and sensor Hg response, a series of experiments were undertaken using Au nanowires and Au thin films sensors Figure **4-9**. We first looked at the impact of the surface to volume ratio by varying the thickness of the nanowires from 30nm to 20nm and observed a 60% increase in the sensitivity (Figure 4-9a). We undertook the same experiment for Au thin films and saw similar results (Figure 4-9b). The nanowires, of course, allow another degree of freedom in adjusting the surface to volume ratio i.e., the width can be changed. For example, by reducing the width of a 1μm wide by 30nm thick thin film to a 40nm wide by 30nm thick nanowire, a 100% increase in response was realized (Figure 4-9c). Similar results were obtained using a 1μm wide and 20nm thick thin film compared to a

40nm wide and 20nm thick nanowire sensor (Figure 4-9d). As may be seen, these results show the importance of the surface to volume ratio, substantiate the model of a surface origin for the sensitivity, and underscore the advantage of the Au nanowire structure over the thin film structure for Hg sensing.

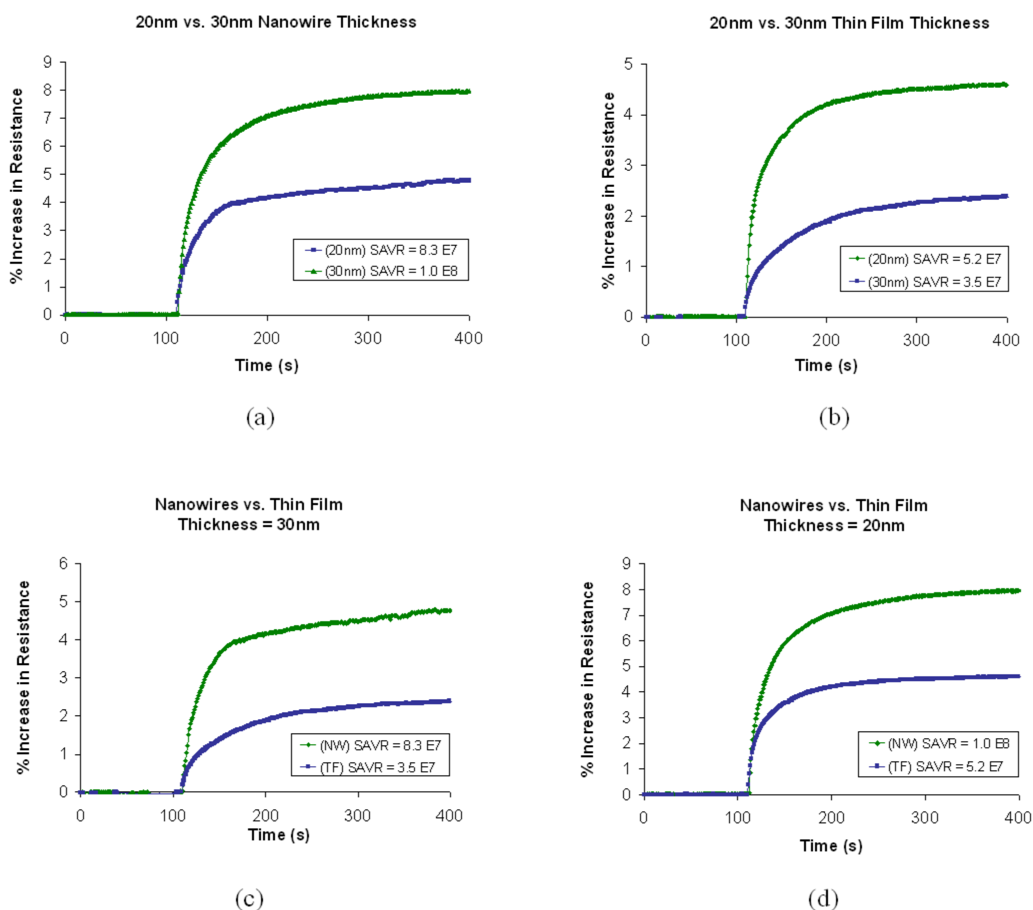

Figure **4-9**: Responses of sensors with varying dimensions to 1µM Hg^{2+}. (a) Comparison of nanowires 30nm thick (blue) and 20nm thick (green). (b) Comparison of thin films 30nm thick (blue) and 20nm thick (green). (c) Comparison of nanowires 30nm thick (green) to a thin film 30nm thick (blue). (d) Comparison of nanowires 20nm thick (green) to thin film 20nm thick (blue).

4.3.5 Selectivity of the Sensor

The selectivity of the nanowire sensors to Hg ions was examined with 1μM-1mM concentrations of $CuCl_2$ and $MgCl_2$ solutions. The same procedures mentioned above for $HgCl_2$ testing were employed for the selectivity experiments. The highest concentrations (1mM) of each electrolyte resulted in less than 1% change in the response of the sensors Figure **4-10** . The lowest concentrations (1μM) resulted in either less than a 0.2% change in response or were undetectable.

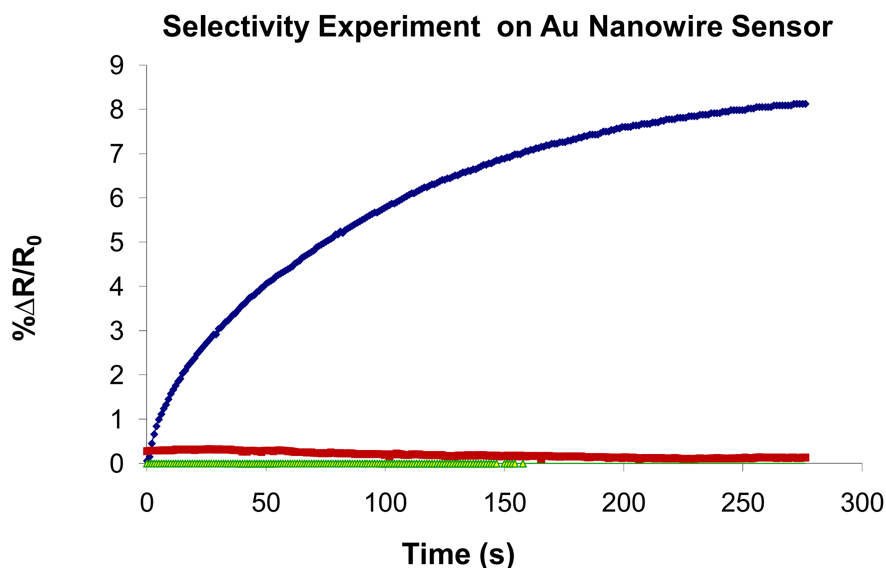

Figure **4-10**: Selectivity of Au nanowire sensor to Cu^{2+} and Mg^{2+}. Concentrations used here were 1mM $CuCl_2$ (red), 1mM Mg_2 (green), and 1μM $HgCl_2$ (blue).

4.4 Hg Sensor Response – JPL Experiments

4.4.6 Experimental Setup

The Hg sensor experiments were performed using the facilities of the Electronic Nose Laboratory at NASA Jet Propulsion Labs. There we had access to an Hg vapor generator capable of providing our test chamber with a constant, continuous flow of ppb-level Hg. The setup consisted of a liquid Hg source which was heated and evaporated. Several mass flow controllers were used to mix air and Hg vapor to get the desired concentrations. The mixing was calibrated for 5-50ppb Hg vapor with a flow rate of 750ml/min; therefore, our tests were limited to this concentration range. Prior to testing the devices, a commercial Hg vapor sensor manufactured by Jerome Instruments was used in-line to verify the Hg vapor concentrations.

The Hg test chamber was made of glass and sealed with o-rings and clamps. The chamber volume was approximately 1L and consisted of four ports; three at the inlet and one at the outlet. The center inlet port was used for introducing the gas flow into the chamber. The second inlet port was closed off and the third contained sealed electrical feed-throughs. The outlet port was used to exhaust the gas which was measured by an in-line flow-meter. This measurement helped detect system leaks and prevented over-pressurizing the chamber. The exhausted Hg vapor was transported through the tubing to a $PdCl_2$ mercury trap where it was removed.

Two-point and four-point single nanowire devices were used for the experiments in this section. The nanowires were fabricated to have smooth, reproducible

morphologies. At this point in the study, the nanowire devices have high yield and reproducibility between devices.

4.4.7 Sensor Response to Hg

Single Au nanowire devices were exposed to varying concentrations of Hg vapor (Figure **4-11**): 10ppb, 20ppb, 30ppb, and 40ppb which were introduced to the chamber for single 15s bursts at t=150s. The sensors began to respond at t=160s.

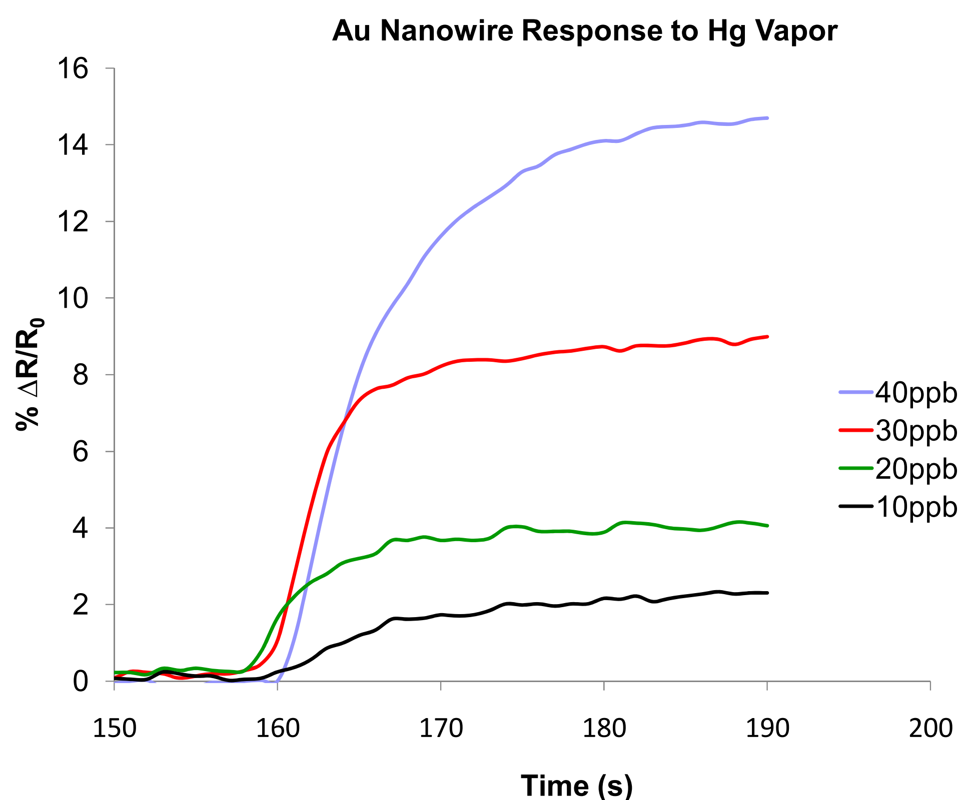

Figure **4-11**: Au nanowire response vs. time to varying Hg vapor concentrations.

The response was not limited by the diffusion of Hg from the flow to the Au surface, but rather by the transport of the vapor from the line to the devices in the chamber. The short bursts were used to ensure low coverage of Hg on the Au nanowire surface. In this range, the resistance is expected to be linear with concentration [12]. A plot of the response vs. concentration is given in Figure **4-12**. The dynamic sensitivity can be extracted from the slope of the line and is given by Eq. **4.3**. This equation obviously has a limited range of accuracy as concentrations as low as 5ppb are readily detected with the nanowire sensors.

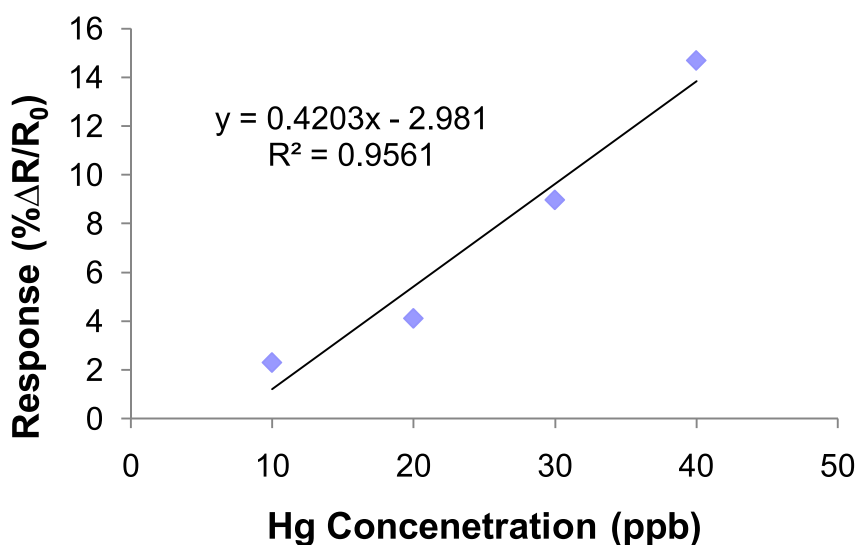

Figure **4-12**: Plot of the nanowire sensor response to varying Hg concentrations.

$$Response = 0.4203C - 2.981 \qquad \textbf{4.3}$$

where, C is the concentration of Hg vapor in ppb.

4.4.8 Multiple Exposures and Sensor Regeneration

The single Au nanowire sensors were tested for multiple exposures (reusability) and sensor regeneration capability. Figure **4-13** shows the response of a single 40nm wide, 20nm thick Au nanowire sensor that was exposed to 5ppb Hg vapor for 1.5ks. Once the resistance saturated, the device was heated to 80C driving the Hg vapor off the nanowire surface. Resistance measurements showed that the sensor returned to its baseline value within 300s. A second 5ppb, 1.5ks exposure illustrates that the sensor response was very reproducible after the first regeneration.

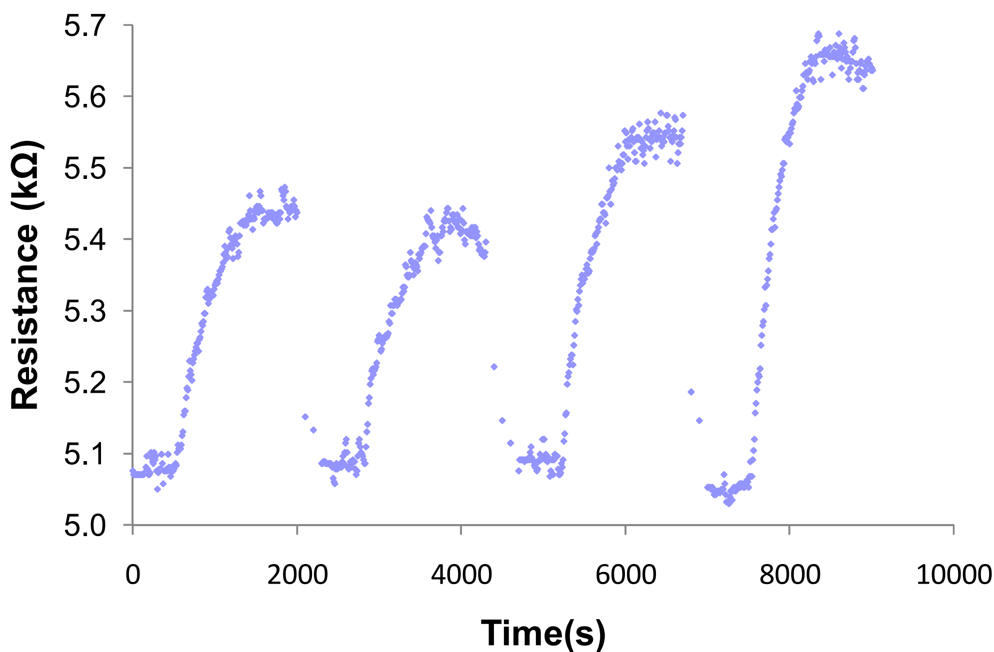

Figure **4-13**: Response of nanowire sensor to multiple exposures and multiple concentrations (5ppb, 5ppb, 20ppb, and 50ppb; left to right). Sensor regenerated to base-line value after each exposure.

The sensor was regenerated again and then exposed to 20ppb Hg. As expected the response saturated at a higher resistance value and regenerated as quickly as after the 5ppb exposure. The final exposure, at 50ppb, exhibited the largest response of all. These results demonstrate the ability of the sensor to be exposed and quickly regenerated for additional uses. However, we found that the Hg covered nanowires eventually degrade and ultimately fail if re-used too many times or if heated to temperatures above 100C. This is likely due to the exchange reactions that occur between the Hg and Au at the surface of the nanowire. One would expect the morphology of the nanowires to change slightly with each exposure and regeneration cycle.

4.4.9 Size Effects

To investigate the effects of size on the response of the sensors, four-point single nanowire devices were fabricated with 20nm thickness and varying line-widths: 30nm, 40nm, 50nm, 75nm, 100nm, 500nm, and 1μm. The electrical resistivity of the nanowires was measured and the devices were placed inside the test chamber where they were exposed to a continuous flow of 50ppb Hg for 1ks. After the exposure, the electrical resistivity was re-measured for each device. The resulting plot of resistivity vs. Au nanowire line-width before and after the Hg exposure is shown in Figure **4-14**. To highlight the changes in resistivity, $\Delta\rho$ is plotted against the line-width in Figure **4-15** and the sensitivity is plotted against the line-width in Figure **4-16**. It can be seen in these figures that the change in resistivity and sensitivity remains relatively flat for wires with line-widths greater than 100nm. Below 100nm, there is a very sharp upturn in resistivity

change and sensitivity; the sensitivity more than doubles from about 6% at the 100nm line-width to nearly 15% at the 30nm line-width.

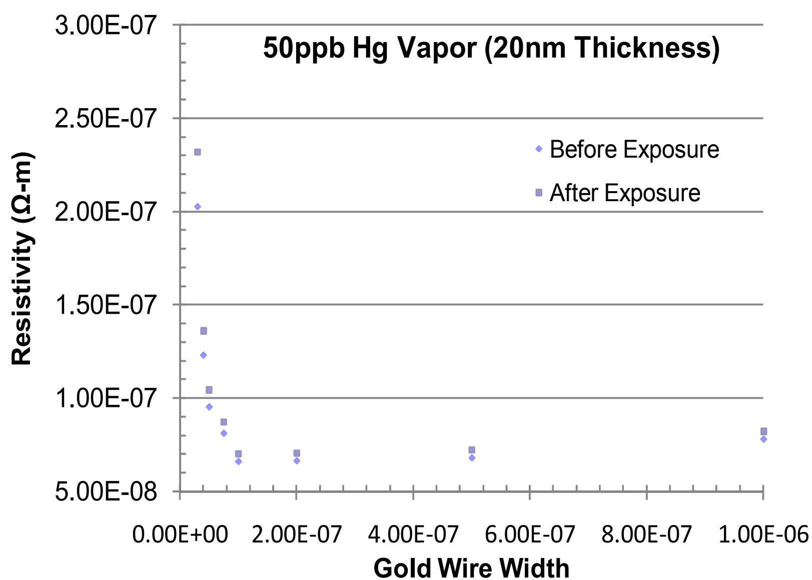

Figure **4-14**: Plot of the Au wire resistivity vs. line-width before and after 1ks 50ppb Hg exposure.

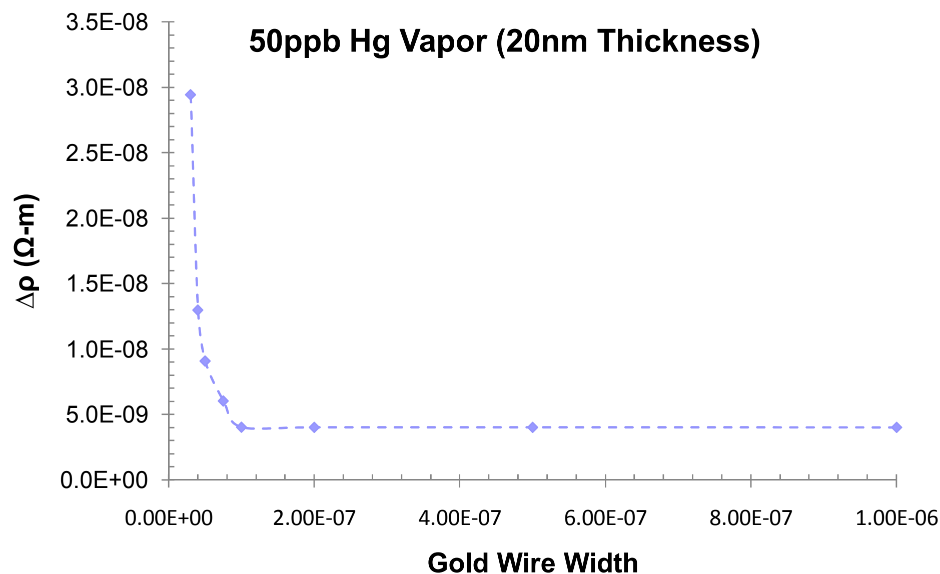

Figure **4-15**: Plot of the change in Au nanowire resistivity vs. line-width after 50ppb Hg exposure.

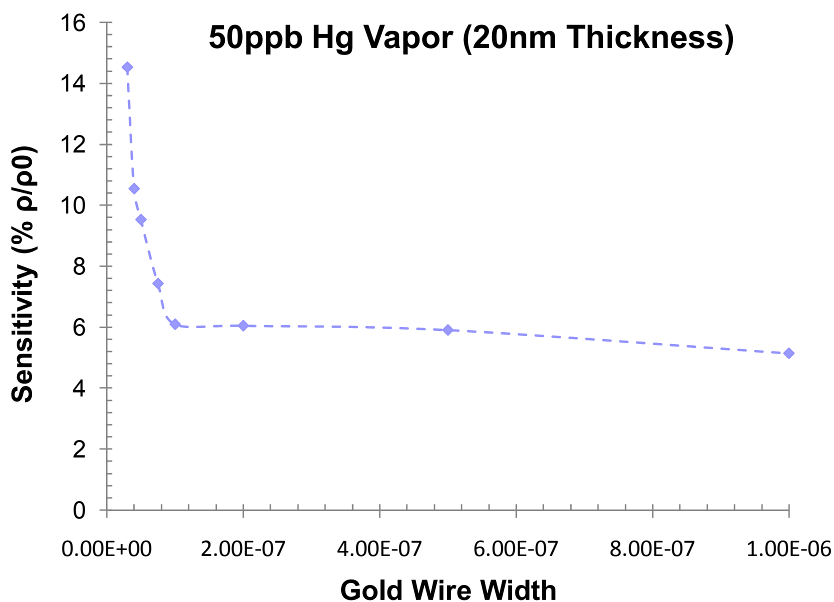

Figure **4-16**: Plot of sensitivity vs. Au line-width.

The increases in resistivity and improved sensitivity can be accounted for by the changes in the parameters of the *FS-MS* model for scattering and the reduced electron percolation in the smaller wires. If we assume that surface scattering in the Au nanowire is not completely diffuse, then we would expect the specularity parameter, p, to decrease upon Hg adsorption. The effect of this scattering would be exacerbated by the wires with the smaller line-widths; this is consistent with the results shown in the figures above. Furthermore, the diffusion of Hg into the grain-boundaries will increase scattering there and result in an increased reflection coefficient, R. The increase in R should equal for all line-widths since the grain diameters are approximately the same. However, if the smaller wires effectively minimize the electron percolation paths, then the increased R will be more significant because the electrons will have to cross each of the affected grain-boundaries.

The surface to volume ratio for the various line-widths were calculated and plotted against the nanowire sensitivity (Figure **4-17**). Similar to the Hg^{2+} results, we found that the sensitivity scaled linearly with the surface to volume ratio. These results underscore the advantages of the nano-scale for chemical sensing applications which involve chemisorption surface reactions.

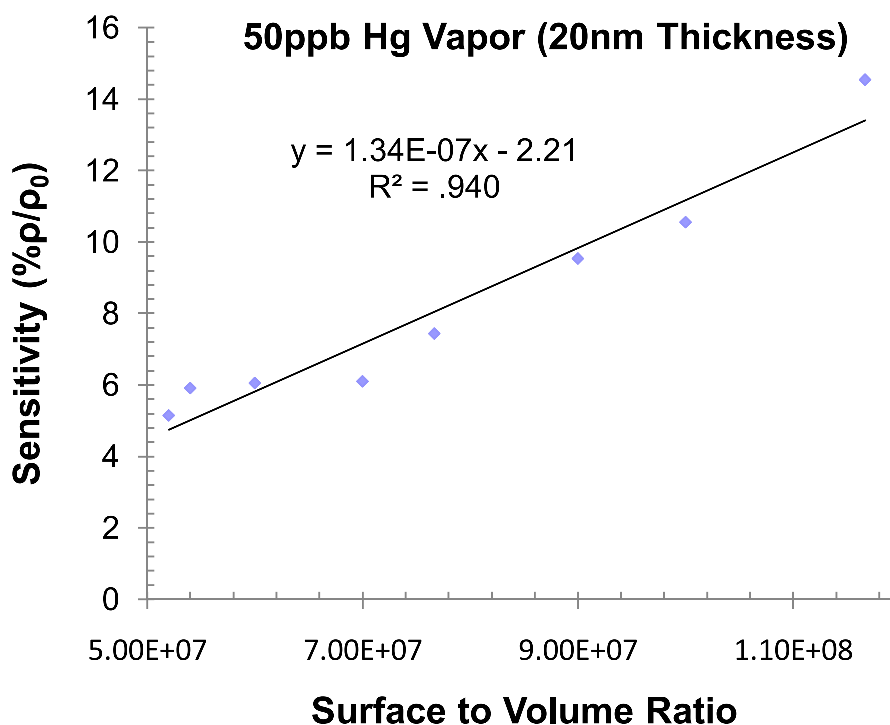

Figure **4-17**: Sensitivity vs. surface to volume ratio for the Au nanowires.

4.4.10 Sensor Selectivity

The selectivity of the Au nanowire sensors were tested by exposing them to ammonia, carbon monoxide, and hydrogen forming gas. A similar test setup and experimental procedure were used to introduce the gases into the test chamber and measure the response of the nanowire sensors. For these experiments, two-point single Au nanowire devices with 20nm thickness and 40nm line-width were used. The response of the sensor to 100ppm NH_3 is shown in Figure **4-18**. The gas was introduced at t=300s and resulted in less than a 0.25% increase in resistance after 500s exposure.

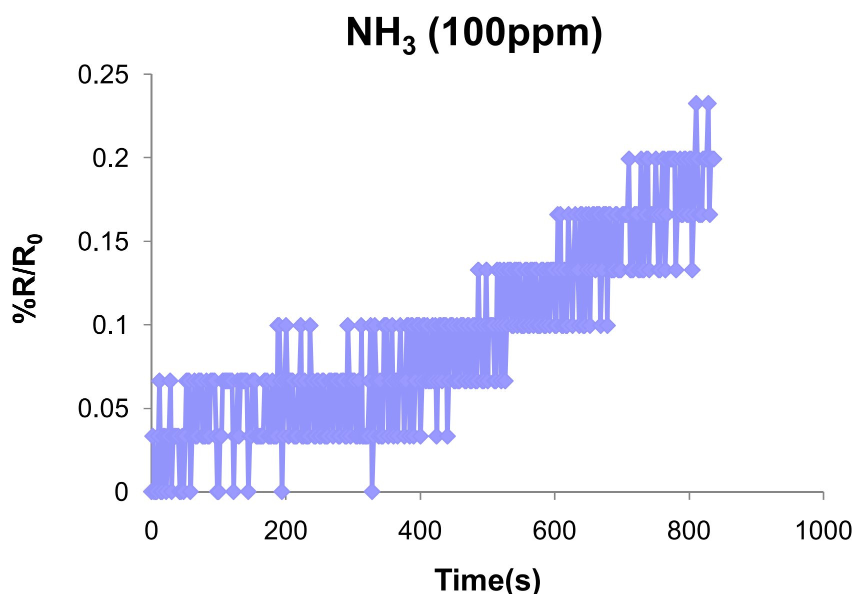

Figure **4-18**: Nanowire sensor response to 100ppm NH_3. Gas was introduced at 300s.

The response of the nanowire sensor to 100ppm CO is shown in Figure **4-19**. The gas was introduced at t=150s and resulted in less than a 0.25% decrease in the resistance after a 300s exposure. The final gas used in the selectivity experiments was 4% H_2 in Ar forming gas. The gas was introduced at 250s and the results are shown in Figure **4-20**. There was nearly a 2% decrease in resistance after 350s exposure. This was unexpected since there are few reports of hydrogen uptake in Au films. After saturation, the gas flow was halted and it was found that the process was irreversible; additionally, subsequent exposures did not result in decreases in the nanowire device. It is unclear exactly why this resistance drop occurred. One possible explanation, is that the hydrogen diffused

into the Pt contacts and caused a volumetric change. This swelling could improve the contact between the Pt and Au and result in a decrease in measured resistance.

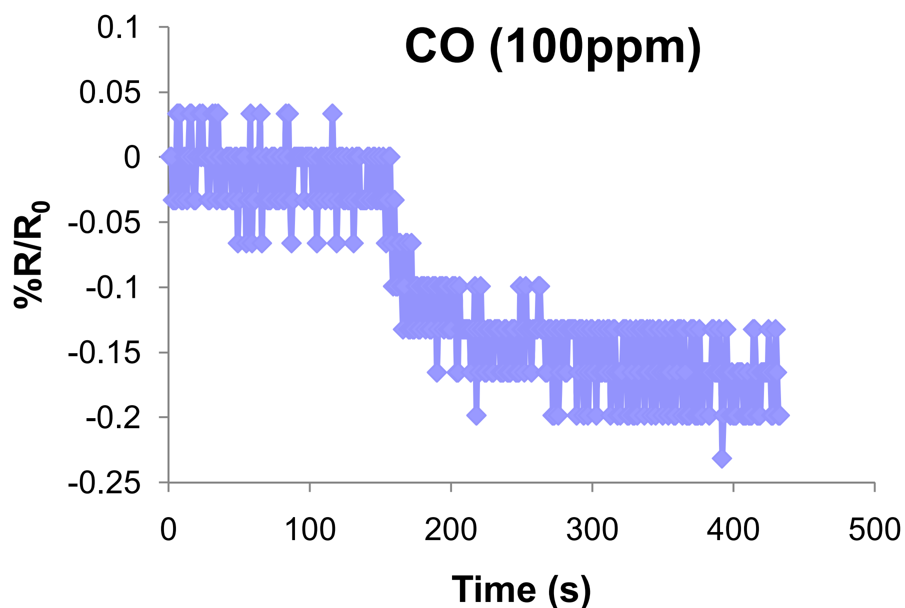

Figure **4-19**: Nanowire sensor response to 100ppm CO. Gas was introduced at 300s.

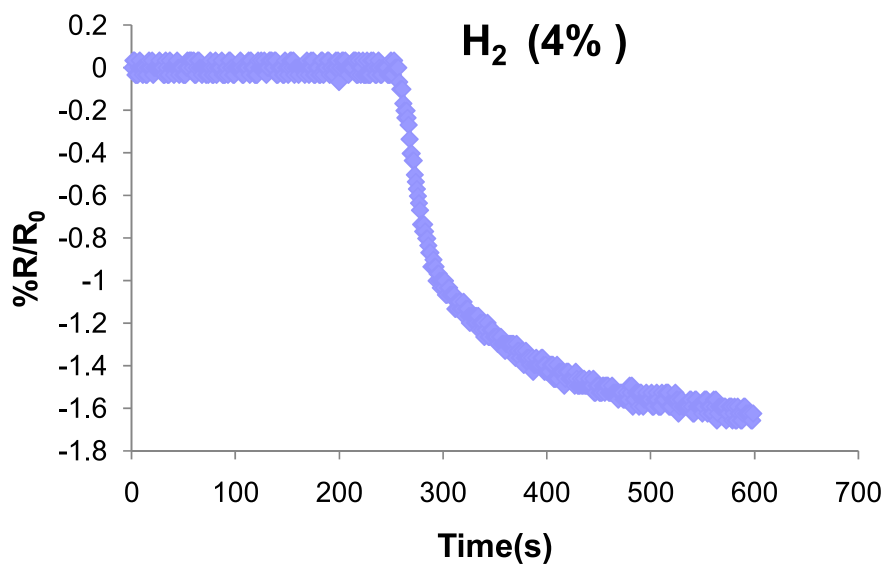

Figure **4-20**: Nanowire sensor response to 4% H_2. Gas was introduced at 250s.

4.5 Applications and Advantages of the Nanowire Hg Sensor

The nanowire sensors developed here could be used for a wide variety of Hg sensor applications. One possibility would be to use the sensors for detecting Hg spills or leaks. This could be done by continuously monitoring the air quality near Hg sources or by periodically sampling the air near the source. Another application would be to use the nanowire sensors in smoke stacks of coal-burning power plants. In such cases, they would have to be placed down-stream in a region where the exhaust is much cooler than the regeneration temperature of the sensor (80C). Additionally, the monitoring time would be rather long since the Hg concentration is low in the stacks. A final application would be to use the sensors to determine the concentration of Hg in rivers and lakes. A known quantity of water could be introduced onto the sensing element and the concentration extracted. The nanowires could be used for many other applications as well. Its primary limitation is the temperature of the sensing environment. The nanowire sensor would be inadequate for sensing in environments at or above 80C due to the rapid desorption of Hg from Au in this temperature range.

From our experimental results we can conclude that the nanowires have three key advantages over other commercially available Hg sensors: (1) The nanowire devices are lower power. The low power of operation makes the nanowire devices very attractive for portable sensor units; they will require smaller batteries and will have an extended operation time compared to their competitors. (2) They can be used for Hg detection in air and water. Most of the sensors target Hg in either air or water environments, but not

both. We have demonstrated that our nanowire sensors function well and are suited for sensing in both environments. (3) The third key advantage is the amount of Hg released during sensor regeneration. Due to the small size and high surface to volume ratio of the nanowires, they require less Hg to adsorb on the surface to obtain an equivalent response. Therefore, during sensor regeneration, the quantity of Hg released from the nanowire is less than a thin film. This makes the regeneration process safer and more environmentally friendly than its competitors.

4.6 Summary

To summarize, we have developed a manufacturable and highly responsive Au nanowire sensor capable of detecting ppb concentrations of Hg in air and water. The nanowire sensor exhibits a superior response compared to thin film sensors and it was demonstrated that this response is closely related to the size and morphology of the nanowire. The improved sensitivity was explained by the FS theory for surface and grain-boundary scattering and the minimization of electron percolation. By carefully controlling the sensor fabrication steps, we were able to obtain reproducible smooth, continuous nanowire morphologies and consequently obtain highly responsive, selective, and reproducible sensors.

4.7 References

1. M. Li, H.X. Tang, and M.L. Roukes, *Nature Nanotechnology*, 2, 114 (2007).

2. Z.J. Davis and A. Boisen, *Applied Physics Letters* 87, 013102 (2005).

3. Y. Cui, Z. Wei, H. Park, and C.M. Lieber, *Science*, 293, 5533 (2001).

4. F. Favier, E.C. Walter, M.P. Zach, T. Benter, and R.M. Penner, *Science*, 293, 5538 (2001).

5. B. J. Murray, E.C. Walter, and R.M. Penner, *Nano Letters*, 4, 665 (2004).

6. A.N. Shipway, E. Katz, and I. Willner, *ChemPhysChem*, 1, 18 (2000).

7. F.J. Ibanez, U. Gowrishetty, N.M. Crain, K.M. Walsh, F.P. Zamborini, *Analytical Chemistry*, 78, 753 (2006).

8. A.K. Kalkan, H. Li, C.J. O'Brien, and S.J. Fonash, *IEEE Electron Device Letters*, 25, 526 (2004).

9. C. Durkan and M.E. Welland, *Physical Review B*, 61, 14215 (2000).

10. W. Steinhogl, G. Schindler, G. Steinlesberger, M. Traving, and M. Engelhardt, *Journal of Applied Physics*, 97, 023706 (2005).

11. EPA's Roadmap for Mercury, 2006, http://www.epa.gov/mercury/roadmap/htm

12. J.J. McNerney, P.R. Buseck, and R.C. Hanson, *Science*, 178, 611 (1972).

13. P.J. Murphy, *Analytical Chemistry*, 51, 1599 (1979).

14. J.J. Caron, R.B. Haskell, P. Benoit, and J.F. Vetelino, *IEEE Transactions on Ultrasonic and Ferroelectric Frequency Control*, 45, 1393 (1998).

15. V.M. Mirsky, M. Vasjari, L. Novotny, V. Rehacek, V. Tvarozek, and O.S. Wolfbeis, *Nanotechnology*, 13, 175 (2002).

16. H.K. Chaurasia, A. Huizinga, and W.A.G. Voss, *Journal of Physics D: Applied Physics*, 8, 214 (1975).

17. E.E. Huber, Jr, *Applied Physics Letters*, 8, 169 (1966).

18. R.W. Joyner, M.W. Roberts, *Journal of the Chemical Society, Faraday Transactions 1*, 69, 1242 (1973).

19. T.T. Mercer, *Analytical Chemistry*, 51, 1026 (1979).

20. X.M. Yang, K. Tonami, L.A. Nagahara, K. Hashimoto, Y. Wei, and A. Fujishima, *Surface Science*, 319, L17 (1994).

21. R. Nowakowski, T. Kobiela, Z. Wolfram, and R. Dus, *Applied Surface Science*, 115, 217 (1997).

22. C. Battistoni, E. Bemporad, A. Galdikas, S. Kaciulis, G. Mattogno, S. Mickevicius, and V. Olevano, *Applied Surface Science*, 103, 107 (1996).

23. J. Inukai, S. Sugita, and K. Itaya, *Journal of Electroanalytical Chemistry*, 403, 159 (1996).

24. M. Levlin, E. Ikavalko, and T. Laitinen, *Fresenius Journal of Analytical Chemistry*, 365, 577 (1999).

25. J.R. Anderson, *Chemisorption and Reactions on Metallic Films*, Academic Press: New York (1971).

26. M.A. George and W.S. Glaunsinger, *Thin Solid Films*, 245, 215 (1994).

Chapter 5

Electrical Stressing Gold Nanowires

5.1 Introduction

A technique is presented here which enables the ability to control the surface morphology of metallic nanowires by subjecting them to a sufficient electrical stress. By utilizing this technique, the electrical conductance of the Au nanowires was increased by up to three orders of magnitude. Furthermore, the technique was employed to significantly improve the sensitivity and reproducibility of the gold nanowire mercury sensor. This technique presents more flexibility than many other post-fabrication modification methods by providing the ability to locally alter the morphology of individual nanowires supported on a single substrate.

One-dimensional nanostructures have emerged as promising building blocks for a wide range of electronic applications such as transistors, electrical interconnects, and chemical gas sensors. Consequently, a great deal of research has been focused on developing cheap and effective fabrication techniques to manufacture the nanowires. These techniques range from standard e-beam lithography [1] [2] to the one-dimensional self-assembly of nano-colloids [3][4][5][6]. The various fabrication approaches oftentimes result in nanowires exhibiting a wide range of morphologies. Since the nanowire morphology is closely related to its electrical properties, it is desirable to have methods to alter the as-fabricated morphology. This can be done by utilizing post-

fabrication modification techniques like thermal annealing [7] and chemical treatments [8]. Such techniques allow for a great degree of morphology control, but are limited to cases in which all nanowires and materials on the substrate require the same processing conditions. This, however, is not always the case; especially for highly integrated devices containing multiple materials and nano-structures. Therefore, a technique that can locally modify individual nanowires is desired.

Some techniques capable of modifying individual nanowires have been recently reported in the literature. One such method involves applying large current densities through a nanowire thus subjecting it to considerable joule heating and electromigration. This enables grain-boundaries to migrate and to re-structure the nanowire morphology. It has been demonstrated that by using this technique, a metallic nanowire can be transformed from polycrystalline to single crystalline [9]. Similar techniques, which utilize electrical stress, have been developed and employed to controllably form nanoscale break-junctions in metal lines [10] [11] and also to improve the electrical contact between carbon nanotubes [12] and metallic electrical pads [13].

With this in mind, the effects of large electrical stresses on our vapor-deposited metallic nanowires were investigated. It was found that the large electrical stresses result in substantial morphology changes in nanowires with rough, discontinuous surfaces. From these results, we explored and developed a controllable technique which utilizes electrical stress to systematically alter the electrical properties and morphology of individual metallic nanowires. This technique has been used to increase the electrical conductance of the Au nanowire devices by up to three orders of magnitude and to significantly improve the sensitivity and reproducibility of the Au nanowire Hg sensor.

The as-fabricated nanowires with rough morphologies were electrically characterized and found to have electrical conductance values significantly lower than the smooth nanowires. Additionally, the measured conductance values varied substantially between devices (Chapter 3). It was apparent upon FESEM and AFM analysis that the low conductance and poor reproducibility was due to the excessive roughness in the wires. Some of the nanowires were so rough that they would more adequately be described as a line of partially connected particles rather than a smooth continuous wire. Although this island-like deposition of Au on silicon dioxide was not unexpected, we found that the substrate condition prior to the Au vapor deposition greatly influenced the morphology of the wires (Chapter 2).

5.2 Electrical Stress Technique

In order to study the effects of electrical stress on the nanowires, we developed the following technique: An electrical characterization tool (HP 4145B) was first connected to the platinum contact pads at the end of the nanowire device via a probe station. Then a voltage sweep, starting at 0V and incremented in 100mV intervals with a 1s hold time was applied across the device to stress the nanowires. During the sweep, the output current was continuously monitored and the electrical stress was discontinued less than 5s after the signal deviated from the linear I-V response. If the electrical stress was continued beyond this transition region, the signal would enter a range of instability and would inevitably fail due to excessive heating or electromigration. To prevent device failure and to reap the benefits of this technique, the electrical stressing was discontinued

once the output current entered within a predetermined range. This range was previously established by electrically stressing a device to failure and recording the transition and failure points.

5.3 Electrical Stress Induced Conductance and Morphology Changes

The aforementioned electrical stress technique was used on single and multiple nanowire devices with rough morphologies. AFM analysis was employed to ascertain the morphology changes resulting from the technique. Figure **5-1** represents the nanowire electrical stressing technique and the resulting conductance changes. The largest observed conductance increase was three orders of magnitude. Figure **5-2 (a)** and **(b)** are AFM images of nanowires before the electrical stress technique and Figure **5-2 (c)** and **(d)** are AFM images of nanowires after the electrical stressing technique. As may be seen from the figure, the electrical stressing resulted in significant smoothing of the nanowire morphologies. This change in surface morphology improved the continuity of the wires and resulted in increased nanowire conductance. We attribute this improvement to the changes in grain boundary potentials (height and width) during grain growth and re-structuring.

Current-voltage (I-V) sweeps were performed on the devices after the electrical stressing and a linear response with an increased slope was observed (Figure **5-3**). The magnitude of increase depended on the initial conductance of the wires and was greater for devices with lower initial conductance values. In other words, when the electrical stress technique was used on nanowires with larger initial conductance values, relatively

small changes were observed (Figure **5-4**). This is expected since the electrical conductance is directly related to the level of nanowire roughness.

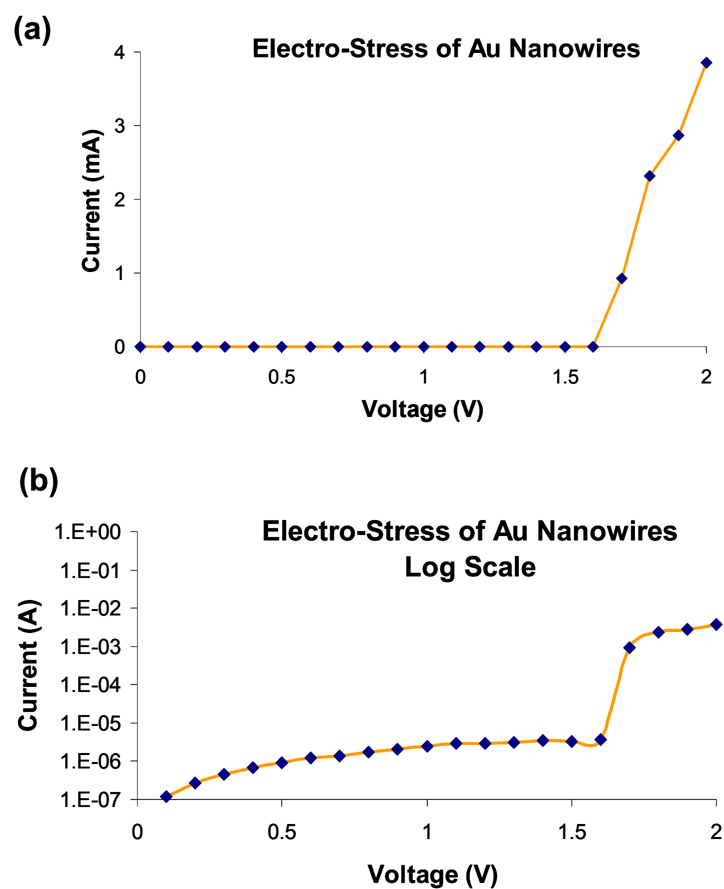

Figure **5-1**: Electrical stress technique employed on a multiple nanowire device (a) linear scale, (b) log-scale.

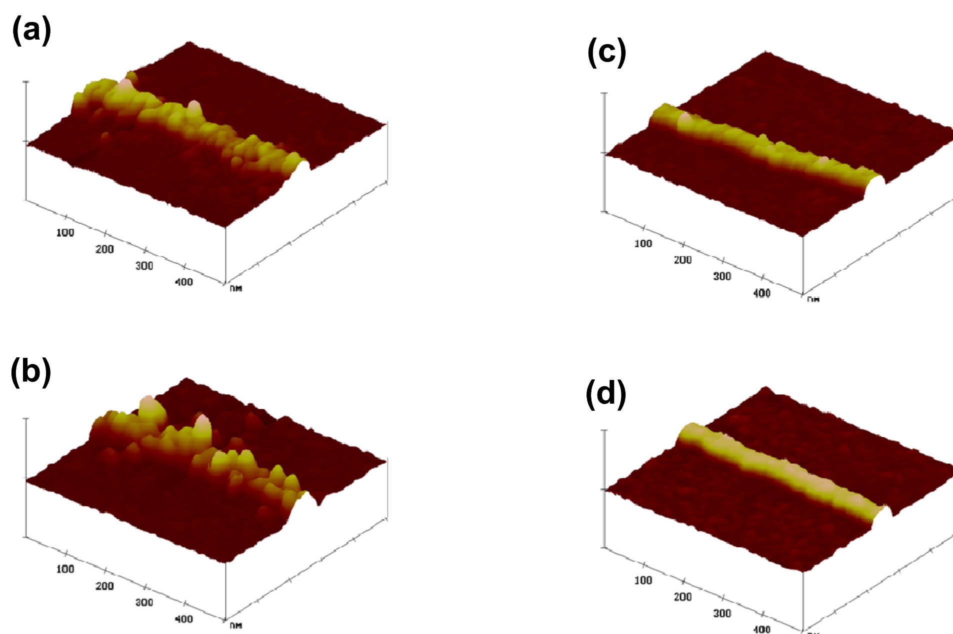

Figure **5-2**: AFM images of gold nanowires. The nanowires on the left are of the as-fabricated, rough type. The nanowires on the right have been electrically stressed to alter their morphology using our post-deposition approach to morphology control.

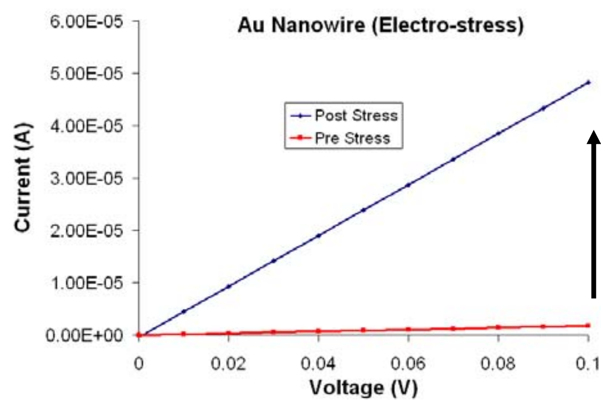

Figure **5-3**: I-V curves of a single 40nm wide Au nanowire before and after the electrical stressing. The curve remains linear, but has an increased slope.

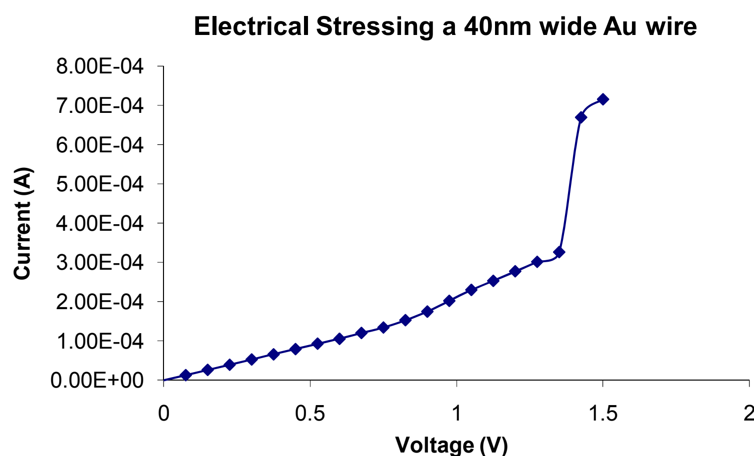

Figure **5-4**: Electrical stressing a single 40nm wide Au wire. The achievable changes in conductance depend on initial conductivity and morphology.

It is well known that nanowires subjected to large electrical stresses experience significant joule heating and electromigration. If the current density is large enough, the atoms will migrate along the nanowire length and eventually result in device failure. The dominating factor for atomic migration (i.e. heat or electromigration) prior to device failure is oftentimes difficult to discern as they act synergistically on the nanowire. This becomes even more difficult to distinguish for nanowires which exhibit significant surface roughness and have only a few grains across their width. In such cases, each grain forms an important conduction path in the wire and statistical fluctuations in the microstructure can influence the transport properties. Therefore, the relative contribution of heating and electromigration on the observed changes in morphology is unclear. It is apparent, however, that the regions of small cross-sectional area will be affected more than the regions of larger cross-sectional area. Since our nanowires are very rough, only

an average thickness can be used in the current density calculations. Fortunately, the technique we have developed does not require an accurate assessment of current densities, but rather a real-time feedback loop between the applied stress and changes in the electrical conductance.

5.3.1 Failure Analysis of Electrically Stressed Nanowires

A stress-to-failure test was performed in an attempt to ascertain any information regarding the migration of atoms during the electrical stress technique. Figure **5-5** shows a plot of the I-V curve of a multiple nanowire device stressed to failure. The curve is non-linear and gradually increases to the failure current density. At 7.3V, the curve turns downward indicating the failure of the nanowires. An I-V sweep was performed post-failure and it was confirmed that the wires were electrically discontinuous. The plot highlights the optimum region to discontinue the electrical stressing if the goal were to increase the device conductance.

A similar stress-to-failure test was performed on a 40nm wide single nanowire device (Figure **5-6**). In this experiment, the current density was incrementally increased and the resistance was recorded. The constant current was applied for 10 seconds at each data point before stepping up to the next increment. The resistance slowly decreased as the current density, J, was increased to 6-7 x 10^{11}A/m^2. Then at J = 8.8 x 10^{11}A/m^2 it suddenly dropped two orders of magnitude. The nanowires failed in less than 60 seconds for current densities greater than 9 x 10^{11}A/m^2.

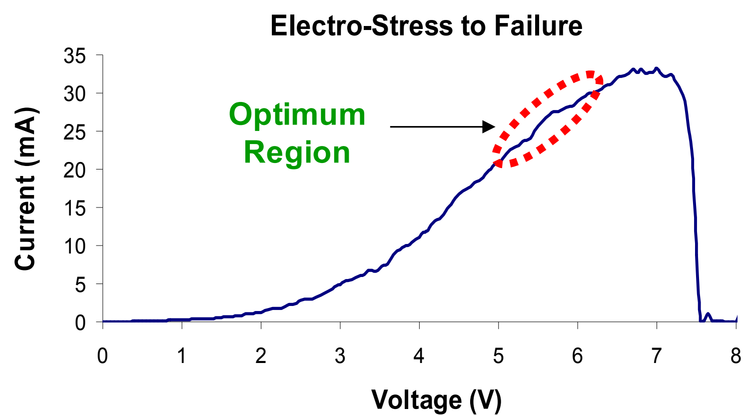

Figure **5-5**: Plot of a stress-to-failure test on a multiple nanowire device. The optimum region to discontinue the electrical stressing is highlighted in red.

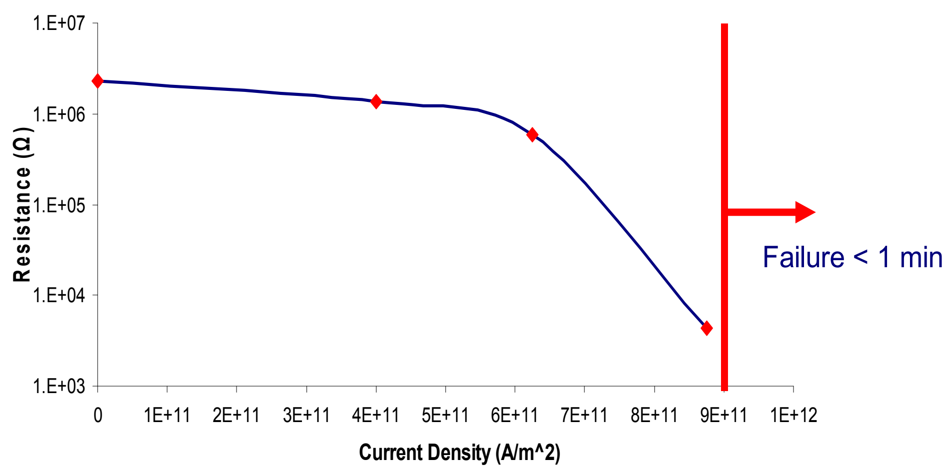

Figure **5-6**: Plot of stress-to-failure test on a 40nm wide single nanowire device.

SEM analysis was performed on the nanowires after the stress-to-failure test in order to determine the mode of failure (Figure **Figure 5-7**). The figure shows that the Au is missing near the contact pad and has accumulated in the upper region of the SEM image. It should be noted that the electrons were flowing from the bottom of the image toward the top during the electrical stress procedure. Though inconclusive, the results are indicative of a thermally-assisted electromigration failure. This is further supported by the current densities being comparable to those reported in literature [**14**][**15**] for this type of failure. It is likely that both joule heating and electromigration play an important role in the electrical stress process. However, the surface morphologies of the nanowires are too variable and disordered to give a general model explaining their relative contributions.

Figure **5-7**: SEM image of a nanowire device that failed during electrical stressing. The electrons were flowing in the bottom to top direction during the electrical stress procedure.

5.4 Thermal Induced Conductance and Morphology Changes

Thermal annealing is another post-fabrication technique commonly used to improve the morphology and conductivity of nanowires [2] and films [16]. The thermal energy supplied to the atoms in the annealing process allows them to diffuse to more energetically favorable positions, induce grain-boundary migration, and re-structure the film. Although the electrical stress technique involves joule heating, we wanted to test the affects of annealing on our devices by heating them on a hotplate at the following temperatures for 300 seconds: 125C, 150C, 175C, 200C, 225C, and 250C. Once the nanowire devices were annealed, they were removed from the hotplate with tweezers and air cooled to prevent any sudden thermal gradients. After 60s of cooling, they were placed on the electrical probe station and I-V measurements were performed. The resulting conductance ($\Delta G/G_0$) changes are plotted against the annealing temperature in Figure **5-8**.

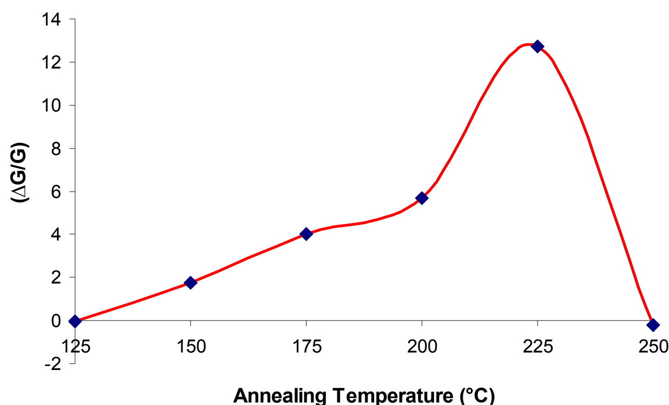

Figure **5-8**: Plot of conductance change vs. annealing temperature for multiple nanowire devices (40nm wire width).

The thermal annealing procedure resulted in up to an order of magnitude increase in the conductance. There was a near linear increase in $\Delta G/G_0$ for annealing temperatures up to 200C. The largest increase was observed at 225C. Above this temperature, the conductance decreased to below its initial value. This is in good agreement with other reports [15] that Au nanowires fail at 220C. The resulting annealed nanowire morphology is shown in Figure **5-9** where it is compared to the as-fabricated and electrically stressed morphologies. It may be seen in this image that the annealed wire is more continuous than the as-fabricated wire, but less smooth than the electrically stressed wire. It follows that the annealed wire should have an intermediate increase in conductance.

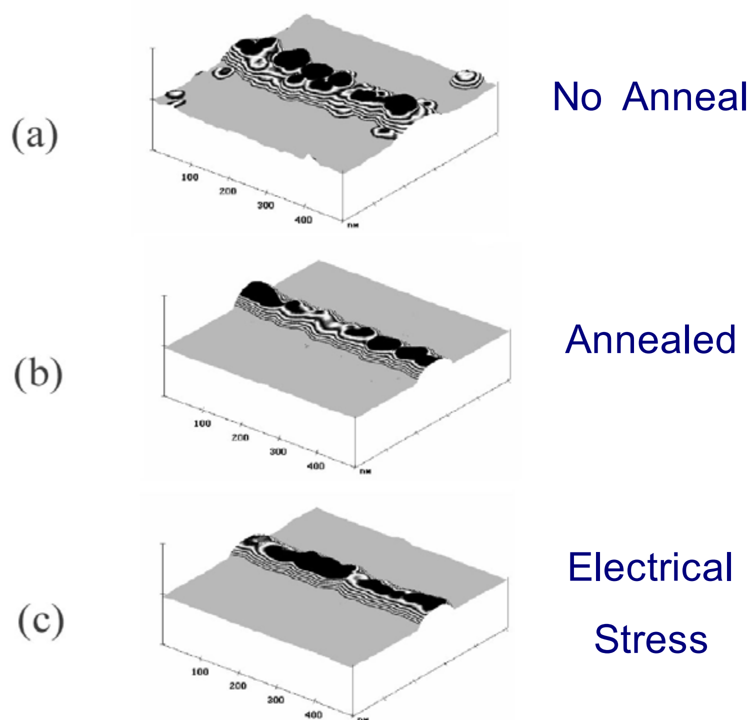

Figure **5-9**: 3D AFM images of 40nm Au nanowires (a) Nanowire is as-fabricated, (b) nanowire is annealed, and (c) nanowire is electrically stressed.

The results indicate that the nanowire morphology and conductance are very sensitive to annealing temperature; it follows that they should also be sensitive to annealing time. One experiment showed that the conductance of the nanowires decreased at temperatures as low as 150C if left on the hot plate too long. This type of low-temperature film degradation is common and nanowires and thin films [17]. Upon annealing, the grains will initially coalesce; however, if given energy and time, the grains will eventually bead up to form a discontinuous string of particles. SEM analysis was used to verify this on nanowires which failed during the annealing process (Figure **5-10**). The images revealed that the failed nanowires beaded up along the entire wire length, forming electrically discontinuous metal particle lines. This mode of failure is easily distinguishable from the electrical stress failure modes.

Figure **5-10**: FESEM image of nanowires that failed during the annealing process. Temperature of the hotplate was 250C.

5.5 Response to Hg Vapor

The nanowire morphology plays a very significant role in determining the response and reproducibility of the Au nanowire sensors. Smooth, continuous nanowires increase their resistance upon Hg adsorption because of the increased surface and grain-boundary scattering (Figure **5-11**). On the other hand, rough, discontinuous nanowires can exhibit the opposite response since transport is dominated by tunneling between inter-particle boundaries (Figure **5-12**). The adsorption of Hg into these boundaries reduces the barrier height by lowering the workfunction of Au and decreases the barrier width by physically filling it in. Both of these phenomena work to decrease the resistance of the wire. As seen in Chapter 2, the rough nanowires have a wide range of resistance values and are not reproducible; therefore, the response to Hg vapor varies substantially between devices. The electrical stress technique has been utilized to increase the nanowires conductance and improve its reproducibility to Hg vapor sensing.

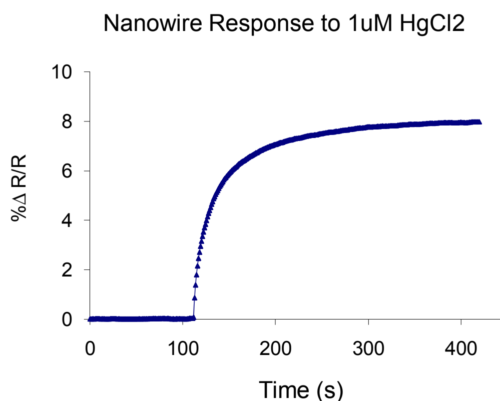

Figure **5-11**: Response of a smooth continuous nanowire to 1μM $HgCl_2$.

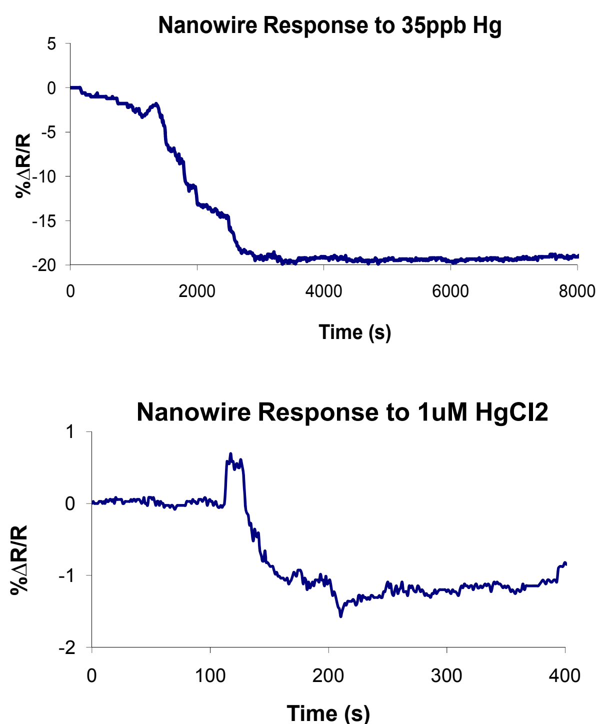

Figure **5-12**: Resistance response of rough, discontinuous nanowire to 35ppb Hg exposure (top) and 1μM $HgCl_2$ (bottom).

5.6 Summary

To summarize, we have presented a technique which enables the ability to control the surface morphology of metallic nanowires by subjecting them to a sufficient electrical stress. By utilizing this technique, the electrical conductance of the Au nanowires was increased by up to three orders of magnitude. Furthermore, the technique was employed to significantly improve the sensitivity and reproducibility of the Au nanowire Hg sensor. Thermal annealing experiments were performed and the results compared to the electrical

stress technique. It was found that annealing increased the conductance of the nanowires by up to one order of magnitude. This is a substantial increase; however, it is lower than the electrical stress technique and lacks the ability to modify the morphology of individual devices on the substrate. Finally, stress-to-failure experiments were performed on the nanowires and the results indicate that the failure was due to thermally assisted electromigration.

5.7 References

1. D. Natelson, *Recent Developments in Vacuum Science and Technology*, 157 (2003).

2. C. Durkan and M.E. Welland, *Physical Review B*, 61, 14215 (2000).

3. Y. Cui, M.T. Bjork, J. A. Liddle, C. Sonnichsen, B. Boussert, and A.P. Alivisatos, *Nano Letters*, 4, 1093 (2004).

4. J.J. Diao, J. Sun, and J.B. Hutchison, *Applied Physics Letters*, 87, 103113 (2005).

5. J. Huang, A.R. Tao, S. Conner, R. He, and P. Yang, *Nano Letters*, 6, 524 (2006).

6. K. Suh, *Small*, 2, 832 (2006).

7. Y. Kakefuda, K. Narita, T. Komeda, S. Yoshimoto, and S. Hasegawa, *Applied Physics Letters*, 93, 163103 (2008).

8. B. J. Murray, E.C. Walter, and R. M. Penner, *Nano Letters*, 4, 665 (2004).

9. S. Fujisawa, T. Kikkawa, and T. Kizuka, *Japanese Journal of Applied Physics*, 42, L1443 (2003).

10. A.A. Houck, J. Labaziewicz, E.K. Chan, J.A. Folk, and I.L. Chuang, *Nano Letters*, 5, 1685 (2005).

11. M.L. Trouwborst, S.J. van der Molen, and B. J. van Wees, *Journal of Applied Physics*, 99, 114316 (2006).

12. C. Jin, K. Suenaga, and S. Iijima, *Nature Nanotechnology*, 3, 17 (2008).

13. L. Dong, S. Youkey, J. Bush, J. Jiao, V. M. Dubin, and R.V. Chebiam, *Journal of Applied Physics*, 101, 024320 (2007).

14. C. Durkan, M.A. Schneider, and M.E. Welland, *Journal of Applied Physics*, 86, 1280 (1999).

15. C. Durkan and M.E. Welland, *Ultramicroscopy*, 82, 125 (2000).

16. D. Smith, *Thin-Film Deposition: Principles & Practice*, McGraw-Hill, Boston (1995).

17. G.P. Zhigal'skii and B.K. Jones, *The Physical Properties of Thin Metal Films*, Taylor and Francis, New York (2003).

Chapter 6

Summary and Future Work

6.1 Summary

In this thesis, we have explored the electrical properties of Au nanowires and utilized their nano-scale phenomena to develop robust, highly sensitive Au nanowire sensors capable of detecting ppb concentration of Hg in air and water. The Au nanowire devices were fabricated using e-beam lithography, evaporation, and other standard device processing techniques. The line-widths ranged from 30nm to 1μm and the thicknesses between 20 and 30nm. SEM analysis was used to verify the dimensions, geometry, and spacing of the nanowires and electrical contact pads after fabrication. AFM analysis was used to determine the thickness, morphology, and average grain size of the nanowires and films. The nanowire characterizations revealed that alterations in the fabrication procedure could produce nanowires with smooth and continuous, or rough and discontinuous morphologies. The cause of this was found to be the surface condition prior to metal evaporation.

The Au nanowires were characterized with four point electrical resistivity measurements and the resistivity was found to increase substantially for line-widths smaller than 100nm. A widely used model for surface and grain-boundary scattering was introduced to explain this phenomenon, but was inadequate because of the assumption that the specularity parameter and reflection coefficient are independent of line-width.

Additionally, two-point resistance measurements were performed on Au nanowires with varying morphology. It was found that the rough nanowires were more resistive and less reproducible than the smooth wires. Furthermore, we found that the surface condition prior to the Au evaporation was strongly related to the resulting nanowire morphology. Finally, the temperature dependence of resistivity was reported on. The nanowires exhibited a linear increase in resistivity with temperature for temperatures above 50K. These results underscored the continuity of the nanowires and indicated phonon-dominated scattering in this temperature range. The temperature coefficients of resistance were extracted from the data and found to be within 10% of the bulk Au value. In addition, an upturn in resistance was observed at temperatures below 50K. This behavior was unexpected and attributed to the mismatch in thermal coefficients of expansion for the nanowires and substrate. It is believed that as the nanowires cool, the separation between grain-boundaries increases, hence reducing the transmission probability of the tunneling electrons.

After electrical characterization, we developed the Au nanowires into manufacturable and highly responsive sensors capable of detecting ppb concentrations of Hg in air and water. The nanowire sensor exhibited a superior response compared to thin film sensors and it was demonstrated that this response was closely related to the size and morphology of the nanowire. The improved sensitivity was explained by the FS theory for surface and grain-boundary scattering and the minimization of electron percolation. By carefully controlling the sensor fabrication steps, we were able to obtain reproducible smooth, continuous nanowire morphologies and consequently obtain highly responsive and reproducible sensors.

Finally, we presented a technique which enables the ability to control the surface morphology of metallic nanowires by subjecting them to a sufficient electrical stress. By utilizing this technique, the electrical conductance of the Au nanowires was increased by up to three orders of magnitude. Furthermore, the technique was employed to significantly improve the sensitivity and reproducibility of the gold nanowire mercury sensor. Thermal annealing experiments were performed and the results compared to the electrical stress technique. It was found that annealing increased the conductance of the nanowires by up to one order of magnitude. This is a substantial increase; however, it is lower than the electrical stress technique and lacks the ability to modify the morphology of individual devices on the substrate. Finally, stress-to-failure experiments were performed on the nanowires and the results indicate that the failure was due to thermally assisted electromigration.

6.2 Future Work

The breadth of topics covered in this thesis lends itself to many potential research directions. A few areas of particular interest include: (1) Developing alternative fabrication techniques to improve the gold nanowire sensor manufacturability; for example, bottom-up approaches like grow-in-place and self-assembly techniques or top down approaches like nano-imprint lithography. (2) Exploring new methods to alter the gold nanowire morphology and investigate how these techniques affect the electrical properties and sensing response of the mercury vapor sensor; for example, heating or cooling the substrate during deposition, use of surface treatments prior to deposition,

chemically etching inter-particle boundaries. (3) Last is the investigation of size effects in other metallic nanowire materials and how chemisorption affects their electrical properties; for example, Pd nanowires for hydrogen sensing and Ag nanowires for ammonia sensing.

Appendix

Nanowire and Thin Film Device Processing Details

F.1 Silicon Dioxide Growth / Silicon Nitride Deposition

The substrate material was n-type, research grade 3” silicon (100) purchased from Silicon Quest. Once unpackaged, the wafers were run through the standard cleans (SC1, SC2) and an HF dip to remove any oxide on the substrate surface. They were then oxidized using a dry oxidation process in the diffusion tubes or they were coated with an LPCVD grown silicon nitride. The thickness of the layers was in the range of 100nm-200nm. The thickness of the insulators was verified by ellipsometer measurements.

F.2 E-beam Lithography Processing

F.2.1 Resist Coating

The silicon wafers were spin-coated with 3% PMMA dissolved in anisole. The coating conditions were as follows:

1) Substrate dehydrated at 180C for 5mins, then cooled for 30s on a heat sink.
2) Two Step Static Dispense:
    1. 500rpm, 100rpm/s, 10s
    2. 4krpm, 10krpm/s, 60s
3) Substrate baked at 180C, 3 mins to drive off solvent.

To prevent charging during the e-beam write, a thin gold conducting layer was thermally evaporated onto the PMMA-coated substrate. The procedure is below:

F.2.2 Conducting Film Deposition

The gold film was thermally evaporated in the Kurt Lesker Evaporator. The starting pressure was below 3 x 10^{-6} torr, the deposition rate was 5 A/s, and the final film thickness was 150A. The quartz crystal monitor was used to monitor the deposition rates and film thicknesses.

F.2.3 E-beam Direct Write

The details leading up to the direct write are covered in Chapter 2. The substrate was then loaded in a holder, the job file was set up and the wafer was exposed.

F.2.4 Etching the Conducing Layer

Once exposed, the gold conducing layer had to be removed before developing the resist. This was done by using commercially available wet etchant: Transene Au Etch. The wafer was immersed into the etchant for 60s, then thoroughly rinsed with DI water and nitrogen gun dried.

F.2.5 Developing the Resist

The resist was developed with a 1:7 mixture of MIBK:IPA for 130seconds in a temperature controlled bath set at 20C. The sample was then rinsed one of two ways:

1. IPA for 30 seconds, nitrogen gun dry
2. IPA for 30 seconds, DI rinse (no spray) 30 seconds, nitrogen gun dry

These rinsing procedures resulted in different nanowire morphologies as described in Chapter 2.

F.3 Ti/Au Evaporation

The Ti/Au evaporations were performed on either the Kurt Lesker or Semicore e-beam evaporators. The base pressures were always kept below $2.5x10^{-6}$ torr and the deposition pressures varied with each run. The Ti was first run through its soak cycle until the desired evaporation rate (0.5A/s) was reached on the QCM. At this point the shutter was opened and the deposition continued until 25A of Ti was deposited. The shutter was then closed and the Ti was sent through the reverse soak process. After this, without breaking vacuum, the source was changed to Au and it was sent through a similar soak cycle until the desired evaporation rate (0.5A/s) was achieved. The deposition was started by opening the shutter and continued until the desired thickness of Au was deposited. To stop the deposition, the shutter was closed and the tool was sent through its cool-down cycle. No substrate heating or cooling was used in the deposition.

F.3.1 Metal Lift-off

The metal lift-off was performed by first placing the coated wafer in a beaker filled with acetone at room temperature. The wafers were soaked for at least 1 hour and then sprayed with an acetone spray bottle to remove the bulk of the Au film. Before drying, the wafer was placed in a second beaker containing fresh acetone. It was soaked for an additional 10mins, re-sprayed, and agitated in an ultrasonic bath to remove the remaining Au. The wafer was then transferred to a beaker filled with IPA and soaked for a few minutes. Finally the wafer was rinsed in a beaker filled with DI water and dried with the nitrogen gun.

F.4 Photolithography

F.4.1 Resist Coating

The wafers were spin-coated with LOR-5A/SPR3012 dual-layer resist stack. The coating conditions were as follows:

1) Substrate dehydrated at 110C for 5mins, then cooled for 30s on a heat sink.
2) Two Step Static Dispense of LOR-5A:
    1. 500rpm, 100rpm/s, 10s
    2. 4krpm, 10krpm/s, 60s
3) Substrate baked at 170C, 3 mins
4) Two Step Static Dispense of SPR-3012:
    1. 500rpm, 100rpm/s, 10s

2. 4krpm, 10krpm/s, 60s

5) Substrate baked at 110C, 90 secs

F.4.2 Alignment, Exposure, Developing the Resist

The electrical contact mask was first loaded on the MA-6 Contact Aligner. Next, the wafer was loaded on the tool and aligned to the mask. Once aligned, the substrate was exposed to the UV radiation for 7 seconds. After exposure, the wafers were baked at 100C in a post-exposure bake step. The exposed resist was then developed in a TMAH-based developer (MF-CD-26) for 1 min, immediately rinsed with DI water for 1min, and finally dried with the nitrogen gun.

F.4.3 Resist Descum

The wafers were next loaded in the PlasmaTherm RIE for the resist descum step. The process conditions were as follows:

Pressure:	100mtorr
Power:	100W
O_2:	40sccm
Ar:	5sccm
Time:	20sec

F.5 Ti/Pt Evaporation

The Ti/Pt evaporations were performed very similar to the Ti/Au evaporations: The base pressures were always kept below $2.5x10^{-6}$ torr and the deposition pressures

varied with each run. The Ti was first run through its soak cycle until the desired evaporation rate (0.5A/s) was reached on the QCM. At this point the shutter was opened and the deposition continued until 35A of Ti was deposited. The shutter was then closed and the Ti was sent through the reverse soak process. After this, without breaking vacuum, the source was changed to Pt and it was sent through a similar soak cycle until the desired evaporation rate (1A/s) was achieved. The deposition was started by opening the shutter and continued until 700A of Pt was deposited. To stop the deposition, the shutter was closed and the tool was sent through its cool-down cycle. No substrate heating or cooling was used in the deposition.

F.5.1 Metal Lift-off

The device fabrication was finalized by lifting off the contact metal. This was done by first heating a beaker of Remover PG to 70C on a temperature controlled hotplate which had a magnetic stirrer. The wafers were soaked in the solution for 30mins and were then transferred to a fresh batch of heated solution for an additional 30min soak. After soaking in Remover PG for 1hr., the wafers were rinsed with IPA, DI water, and finally dried with a nitrogen gun. This step finalizes the device fabrication.

VITA

Shawn Keebaugh

Shawn Keebaugh was born on July 28, 1981. He graduated from Penn State University in 2003 with a B.S. in Engineering Science and minor in Engineering Mechanics. He began his graduate studies at Penn State in August 2003. He has authored papers on the electrical properties of metallic nanowires and their applications to sensors.